Measurement of K_L^0 flux at the J-PARC neutral-kaon beam line for the $K_L^0 \to \pi^0\nu\bar{\nu}$ experiment

Koji Shiomi

Department of Physics, Graduate School of Science,
Kyoto University

January, 2012

Abstract

The $K_L^0 \to \pi^0\nu\bar{\nu}$ decay is a rare CP-violating process. It is a powerful tool for measuring the parameters in the Standard Model and searching for new physics beyond the Standard Model.

The KOTO experiment aims to observe this decay. For this purpose, a K_L^0 beam of high intensity is required. Therefore we constructed a new neutral-kaon beam line at J-PARC. The primary proton energy is 30 GeV and K_L^0 production angle is 16 degree. The K_L^0 flux at the exit of the beam line was estimated by using various simulation packages of hadronic interactions. The expected values of the K_L^0 flux at this beam line differed by up to a factor of three among the packages. While we estimated the sensitivity of the KOTO experiment with the smallest expected value of the K_L^0 flux among simulations, precise knowledge on the K_L^0 yield, as well as its momentum spectrum, is essential to decide experimental design. Therefore, we planed to measure the K_L^0 flux and spectrum with 10% accuracy soon after construction of the beam line.

For the purpose, a unique method to identify the $K_L^0 \to \pi^+\pi^-\pi^0$ decay was developed. Usually, momenta of charged particles are measured by a magnetic spectrometer. However, in the measurement, these were derived by solving the transverse momentum balance of the $\pi^+\pi^-\pi^0$ system. Neutral-kaons could be fully reconstructed with a compact detector system, which was composed of scintillator hodoscopes for charged particle measurement and an electromagnetic calorimeter for photon measurement. The contamination of background events could be suppressed about 1%. We took data over several days in February 2010 and successfully collected 1923 and 2217 $K_L^0 \to \pi^+\pi^-\pi^0$ candidates for the 5.4-cm-long Ni and the 6.0-cm-long Pt targets, respectively.

As a result of the measurement, the K_L^0 flux was obtained with accuracy of about 10%. The measured K_L^0 flux was 2.6 times larger than the value we had been assuming in the KOTO sensitivity estimation, to be 1.94×10^7 and 4.19×10^7 per 2×10^{14} protons on the Ni and the Pt targets, respectively. The sensitivity of the KOTO experiment was re-estimated with results of the measurement, and we found that two times better sensitivity can be expected.

In this thesis, results from these measurements are described, and the impacts of the results on the sensitivity of the KOTO experiment are discussed.

Acknowlegements

This thesis could not be completed without support and guidance from many people. Here, I would like to acknowledge them.

First of all, I would like to express my appreciation to my supervisor Prof. Noboru Sasao, who gave me a wonderful opportunity for the research of high energy physics. I have been always impressed by his idea and instinct for physics.

I would like to thank Prof. Tadashi Nomura, and Prof. Hajime Nanjo. They have taught me physics and experimental methods from basic knowledge to technical issues. I learned methods of physical thinking through discussion with them. Especially, Prof. Tadashi Nomura always gave me powerful support while I was writing this thesis. I would never have reached this successful end without his strong support.

I wish to express my appreciation to Prof. Taku Yamanaka, the spokesperson of the KOTO experiment. He gave me a grate opportunity to cary out the K_L^0 flux measurement. In the measurement, I learned many important things to complete a physics experiment successfully.

I present my appreciation to Prof. Takeshi Komatsubara, Prof. Gei Youb Lim, Prof. Hiroaki Watanabe, for perfect arrangements to send experimental tools from KEK to Tokai and to do crane works to set up detectors in the experimental area. Thanks to their arrangements, we could proceed the experimental preparation smoothly. I would like to appreciate Prof. Yasuhisa Tajima. He always helped us with beam tests at the Research Center for Electron Photon Science, Tohoku University and, prepared various things required for the measurement. I am also thankful to Prof. J. Comfort, Prof. M. Togawa, Prof. Y. Ri, and Prof. H.Y. Yoshida.

I would like to acknowledge all the people in the KOTO Collaboration. Especially, I would like to express my thanks to all the fellows and the graduate students who worked together with me for the beam survey experiment, Dr T. Shimogawa, Mr. K.Y. Baek, Mr. E. Iwai, Mr. N. Kawasaki, Mr. J.W. Ko, Mr. J.W. Lee, Mr. Y. Maeda, Mr. T. Masuda, Mr. D. Naito, Mr. Y. Nakaya, Ms. M. Sasaki, Mr. K. Sato, Mr. Y. Sugiyama, Mr. G. Takahashi, Ms. Y. Yanagida, for giving me the help. The present work would not completed without their hard works. Tokai life was very busy, but I had enjoyed these days with them. I was very happy and so excited to see the first beam of the KOTO beam line with the GOH-monitor, which measured beam profile in the neutral beam.

I would like to show my special thank to Mr. Goh Takahashi. While he prepared for the GOH-monitor, he helped me with the construction of detectors for the K_L^0 flux measurement. Without his help, the detectors had never be constructed in a timely manner.

I am grateful for the help of Dr. Yoshinori Kurimoto. Thanks to his advise, I could become to use VA/TA DAQ boards and make a DAQ system for the measurement.

In addition, I would like to thank all the members of the high energy physics group of Kyoto University, Prof. N. Sasao, Prof. T. Nakaya, Prof. A. K. Ichikawa, Prof. M. Yokoyama, Prof. T. Nomura, Prof. H. Nanjo, Prof. A. Minamino, Prof. T. Sumida, Dr. M. Ikeda, Dr. H. Morii,

Dr. Y. Kurimoto, Dr. K. Hiraide, Dr. Y. Nakajima, Dr. N. Taniguchi, Dr. K. Nitta, Mr. H. Yokoyama, Mr. M. Taguchi, Mr. H. Kawamuko, Mr. S. Gomi, Mr. Y. Kurosawa, Mr. H. Kubo, Mr. T. Usuki, Mr. N. Kawasaki, Mr. T. Masuda, Mr. N. Nagai, Mr. M. Otani, Mr. K. Asada, Mr. K. Ieki, Mr. Y. Maeda, Mr. A. Murakami, Mr. D. Naito, Mr. T. Kikawa, Mr. D. Orme, Mr. K. Suzuki, Mr. G. Takahashi, Mr. S. Takahashi, Mr. T. Hiraki, Mr. T. Yamauchi. Mr. K. Goda, Mr. S. Seki, Mr. T. Tashiro and Mr. T. Nagasaki. My life in the university have been always happy with them. My special thank goes to the "coffee club" members in the laboratory. I have always enjoyed interesting conversation with the members. I hope to continue this club without fiscal bankruptcy, receiving abundant support from gentle staffs.

Finally, I would like to express my special appreciation to my parents for various supports throughout my life.

Koji Shiomi
Kyoto, Japan.
January 2012

Contents

Chapter 1

Introduction

Asymmetry of matter and antimatter in the universe is one of the greatest unsolved problems in particle physics. A key issue to solve this problem is considered to be CP violation, which represents the difference of reaction between matter and antimatter. The very rare decay $K_L^0 \to \pi^0\nu\bar{\nu}$ is a sensitive probe for direct CP violation in the quark sector. The decay is a flavor changing neutral current process that is induced through electroweak loop diagrams. The decay is also sensitive to new physics beyond the Standard Model, because the amplitude of the decay can vary when an unknown particle(s) appears in the loop diagram.

In this chapter, I firstly introduce CP violation. Next, physics motivation of a search for the $K_L^0 \to \pi^0\nu\bar{\nu}$ decay and the current status of experimental searches are described. I also introduce the KOTO experiment which aims at the first observation of the decay at J-PARC. Then, issues on the K_L^0 flux estimation in the beam line for the KOTO experiment are described. To solve them is the motivation of this research. Finally, the outline of this thesis is described in the last section.

1.1 CP Violation

A CP violating phenomenon in the quark sector was first observed in a K-meson system by Cronin and Fitch in 1964 [1]. The observed phenomenon was explained by the mixing of two CP states in the K-meson system, and called as "indirect CP violation". Afterwards, another CP violating phenomenon, which can not be explained by the mixing of two states, was observed and called "direct CP violation" [2].

In the Standard Model, the Lagrangian of the charged current in the weak interaction is given by:

$$\mathcal{L}_{CC} = \frac{g}{\sqrt{2}}[\overline{u_i}V_{ij}d_jW^- + \overline{d_j}V_{ij}^*u_iW^+] \tag{1.1}$$

where $u_i = (u, c, t)$ are left-handed up-type quarks and $d_i = (d, s, b)$ are left-handed down-type quarks, and $W^\pm$ denote the weak bosons. V_{ij} is the 3×3 unitary matrix (Cabibbo-Kobayashi-Maskawa (CKM) matrix [3]) which connects the up-type quarks with the down type quarks:

$$V_{CKM} = \begin{pmatrix} V_{ud} & V_{us} & V_{ub} \\ V_{cd} & V_{cs} & V_{cb} \\ V_{td} & V_{ts} & V_{tb} \end{pmatrix} \tag{1.2}$$

When CP transformation is applied to the Lagrangian, it changes as:

$$L_{CC} \rightarrow \frac{g}{\sqrt{2}}[\bar{d}_j V_{ij} u_i W^+ + \bar{u}_i V_{ij}^* d_j W^-]. \tag{1.3}$$

If the $V_{ij} \neq V_{ij}^*$, the interaction is not invariant under CP transformation.

The CKM matrix can be described by three Euler-type angles and a complex phase. In the Wolfenstein parameterization [4], matrix elements are expanded in powers of $\lambda = |V_{us}| = 0.22$:

$$V_{CKM} = \begin{pmatrix} 1-\lambda^2/2 & \lambda & A\lambda^3(\rho - i\eta) \\ -\lambda & 1-\lambda^2/2 & A\lambda^2 \\ A\lambda^3(1-\rho-i\eta) & -A\lambda^2 & 1 \end{pmatrix} + \mathcal{O}(\lambda^4), \tag{1.4}$$

where A, ρ, and η are independent real parameters. This parameterization shows clearly that the off-diagonal elements are small and the diagonal elements are close to unity. The parameter η represents the complex phase that causes CP violation.

1.2 $K_L^0 \rightarrow \pi^0\nu\bar{\nu}$ decay

1.2.1 $K_L^0 \rightarrow \pi^0\nu\bar{\nu}$ decay

The rare decay $K_L^0 \rightarrow \pi^0\nu\bar{\nu}$ provides us one of the best probes for understanding CP violation in the quark sector. The decay is a flavor-changing neutral current (FCNC) process from the strange quark to the down quark. In the Standard Model, FCNC processes are forbidden at the tree level. These processes are induced through loop effects, as expressed by the electroweak penguin and box diagrams shown in Fig. 1.1 [5].

The branching ratio of the $K_L^0 \rightarrow \pi^0\nu\bar{\nu}$ decay, $BR(K_L^0 \rightarrow \pi^0\nu\bar{\nu})$, is expressed in the Standard Model as:

$$BR(K_L^0 \rightarrow \pi^0\nu\bar{\nu}) = 6.87 \times 10^{-4} \times BR(K^+ \rightarrow \pi^0 e^+ \nu) \times A^4\lambda^8\eta^2 X^2(x_t), \tag{1.5}$$

where $BR(K^+ \rightarrow \pi^0 e^+ \nu)$ is the branching ratio of the $K^+ \rightarrow \pi^0 e^+ \nu$ decay, x_t is the square of the top and the W mass ratio, $x_t = m_t^2/m_W^2$, and $X(x_t)$ is the Inami-Lim loop function [6] with QCD higher order corrections, respectively. $BR(K_L^0 \rightarrow \pi^0\nu\bar{\nu})$ is proportional to η^2. This means that the $K_L^0 \rightarrow \pi^0\nu\bar{\nu}$ decay is directly related to CP violation.

The most important benefit to study the $K_L^0 \rightarrow \pi^0\nu\bar{\nu}$ decay is that the branching ratio can be predicted with small uncertainty. Contributions from long distance interactions are negligibly small, and the hadronic matrix element can be extracted directly from well-measured $BR(K^+ \rightarrow \pi^0 e^+ \nu)$. Uncertainty in the theoretical calculation is only a few percent.

By using the currently obtained values of the CKM parameters, the $BR(K_L^0 \rightarrow \pi^0\nu\bar{\nu})$ is predicted to be [7]

$$BR(K_L^0 \rightarrow \pi^0\nu\bar{\nu}) = (2.43^{+0.40}_{-0.37} \pm 0.06) \times 10^{-11} \tag{1.6}$$

where the first and the second uncertainties come from the allowed ranges of η and the top mass and intrinsic theoretical uncertainties, respectively.

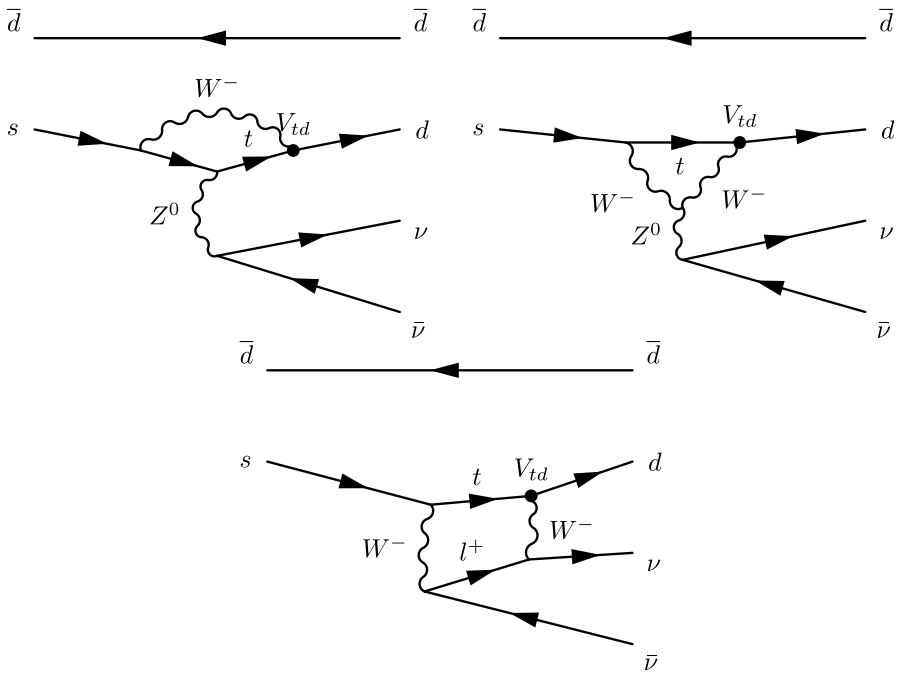

Figure 1.1: Feynman diagrams of the $K_L^0 \to \pi^0 \nu\bar{\nu}$ decay. The decay is mediated by penguin (top) and box diagrams (bottom). In both cases, contributions of the top quark in the loop dominate the decay.

1.2.2 $K_L^0 \to \pi^0\nu\bar{\nu}$ decay beyond the Standard Model

Owing to the small theoretical uncertainty in the estimation of $BR(K_L^0 \to \pi^0\nu\bar{\nu})$, significant excess or deficiency directly indicates existence of new physics beyond the Standard Model. In this section, I first explain the model-independent upper limit that was calculated by the branching ratio of the closely-related process $K^+ \to \pi^+\nu\bar{\nu}$. Next, I introduce several possibilities to modify $BR(K_L^0 \to \pi^0\nu\bar{\nu})$ from viewpoints of new physics model beyond the SM.

Grossman-Nir limit

The rare decay of charged kaon $K^+ \to \pi^+\nu\bar{\nu}$ is strongly related to the $K_L^0 \to \pi^0\nu\bar{\nu}$ decay. Y. Grossman and Y. Nir pointed out the correlation between their branching ratios [8]. The diagram of the $K^+ \to \pi^+\nu\bar{\nu}$ process can be obtained simply by replacing the accompanying down quark with the up quark in the $K_L^0 \to \pi^0\nu\bar{\nu}$ diagram. The correlation between these two modes can be derived from the isospin symmetry. A model independent upper limit for the $BR(K_L^0 \to \pi^0\nu\bar{\nu})$, called the Grossman-Nir limit, can be derived as

$$BR(K_L \to \pi^0\nu\bar{\nu}) < 4.4 \times BR(K^+ \to \pi^+\nu\bar{\nu}). \tag{1.7}$$

The $K^+ \to \pi^+\nu\bar{\nu}$ decay was experimentally observed by the AGS E787/E949 experiment at the Brookhaven National Laboratory. They obtained the branching ratio of the $K^+ \to \pi^+\nu\bar{\nu}$ decay to be [9]

$$\mathrm{BR}(K^+ \to \pi^+\nu\bar{\nu}) = [14.7^{+13.0}_{-8.9}] \times 10^{-11}. \tag{1.8}$$

Calculating from Eq. 1.8, the upper limit to the $K^+ \to \pi^+\nu\bar{\nu}$ decay at the 90 % confidence level is 3.2×10^{-10}. By substituting the upper limit into Eq. 1.7, the upper limit to the $BR(K_L^0 \to \pi^0\nu\bar{\nu})$ can be obtained as

$$\mathrm{BR}(K_L \to \pi^0\nu\bar{\nu}) < 1.4 \times 10^{-9} \quad (90\%\ \mathrm{C.L.}). \tag{1.9}$$

Examples of theories beyond the Standard Model

The $K_L^0 \to \pi^0\nu\bar{\nu}$ decay occurs via loop diagrams and directly violates CP symmetry. If there is any contribution from a new particle that appears in loop diagrams and/or from a new source of CP violation, the branching ratio might vary. We can probe a new physics by measuring the deviation of $BR(K_L^0 \to \pi^0\nu\bar{\nu})$ from the SM prediction.

One of major models of new physics beyond the Standard Model is Minimal Supersymmetric Standard Model (MSSM), which is the minimal extension to the SM, including features of supersymmetry (SUSY). In the general MSSM, it is possible to have new CP-violating phases; this results in a possibility to have the $BR(K_L^0 \to \pi^0\nu\bar{\nu})$ to be a few times 10^{-10}, which is about 10 times larger than the SM prediction. Buras *et al.* studied on the allowed region of $BR(K_L^0 \to \pi^0\nu\bar{\nu})$ and $BR(K^+ \to \pi^+\nu\bar{\nu})$ by scanning the SUSY particle parameters [10].

In contrast, the Minimal Flavor Violation hypothesis (MFV) is designed so that all flavor and CP-violating interactions are linked to the known structure of the CKM matrix. Thus, deviations of the $BR(K_L^0 \to \pi^0\nu\bar{\nu})$ from the Standard Model prediction become small ($\sim 20\%$) in MFV models [11, 12]. Predictions from other hypotheses: littlest higgs model with T-parity (LHT) [13, 14], minimal 3-3-1 model [15] and four generations (4-Gen.) [16], are summarized in Fig. 1.2, as well as the results from the general MSSM and the MFV models.

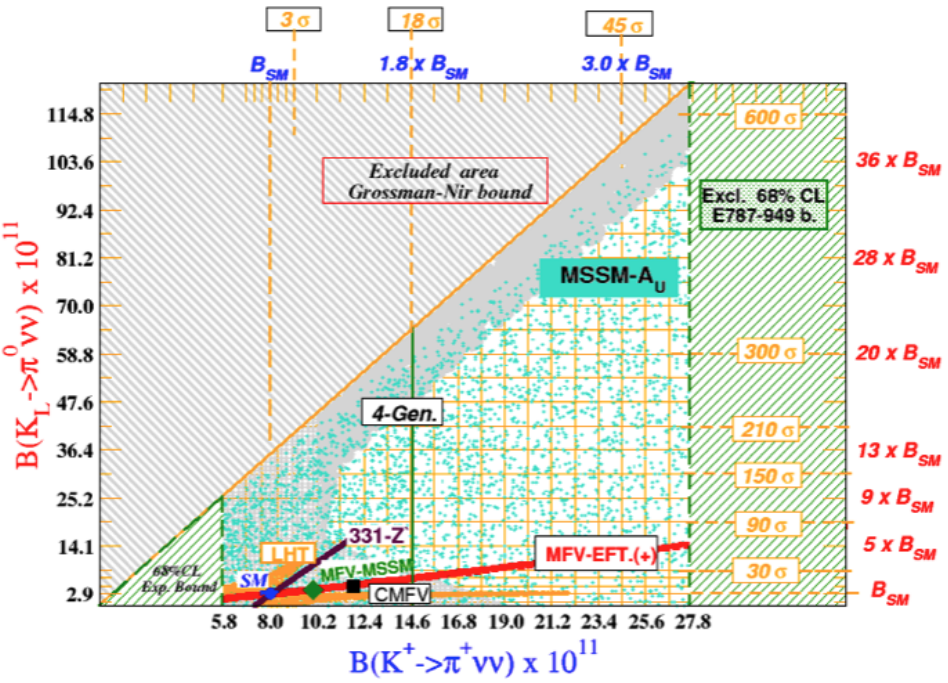

Figure 1.2: The correlation between $BR(K_L^0 \to \pi^0 \nu\bar{\nu})$ and $BR(K^+ \to \pi^+ \nu\bar{\nu})$ by showing the allowed region in various new physics models. Red points show the allowed region in the Minimal Flavor Violation hypothesis (MFV). Yellow points show the allowed region in the littlest higgs model with T-parity (LHT). Purple points show the allowed region in the minimal 3-3-1 model. Emerald green points show the allowed region in the Minimal Supersymmetric Standard Model (MSSM). A gray region show the allowed region in the four generation model. The regions of the shaded lines are excluded by the result of E787 and E949 experiments, which measured the branching ratio of the $K^+ \to \pi^+ \nu\bar{\nu}$ decay. The figure was quoted from the reference [17].

1.2.3 History of $K_L^0 \to \pi^0\nu\bar{\nu}$ search

There were several experiments that searched the $K_L^0 \to \pi^0\nu\bar{\nu}$ decay, as shown in Fig. 1.3. Due to the small value of BR($K_L^0 \to \pi^0\nu\bar{\nu}$), only upper limits were given.

The first study was performed by Littenberg. He extracted a limit for the $K_L^0 \to \pi^0\nu\bar{\nu}$ decay from the data of Cronin and Fitch for the $K_L^0 \to 2\pi^0$ study [1]. The limit was [18]

$$BR(K_L^0 \to \pi^0\nu\bar{\nu}) < 7.6 \times 10^{-3} (90\ \%\ C.L.). \tag{1.10}$$

The following studies were carried out in two different approaches.

One approach used a $\pi^0 \to e^+e^-\gamma$ decay to identify the $K_L^0 \to \pi^0\nu\bar{\nu}$ decay. The advantage is that the decay vertex can be reconstructed with e^+e^- tracks and the invariant mass of $e^+e^-\gamma$ can be calculated, which enables clean π^0 reconstruction. On the other hand, the disadvantage is that the branching ratio of the decay is about 1%, which corresponds to small efficiency. The other approach used a $\pi^0 \to \gamma\gamma$ decay. The advantage is that the branching ratio of the $\pi^0 \to \gamma\gamma$ decay is 99%. The E391a experiment which was conducted at KEK with the latter approach set the current best upper limit on the branching ratio [19]:

$$BR(K_L^0 \to \pi^0\nu\bar{\nu}) < 2.6 \times 10^{-8} (90\ \%\ C.L.). \tag{1.11}$$

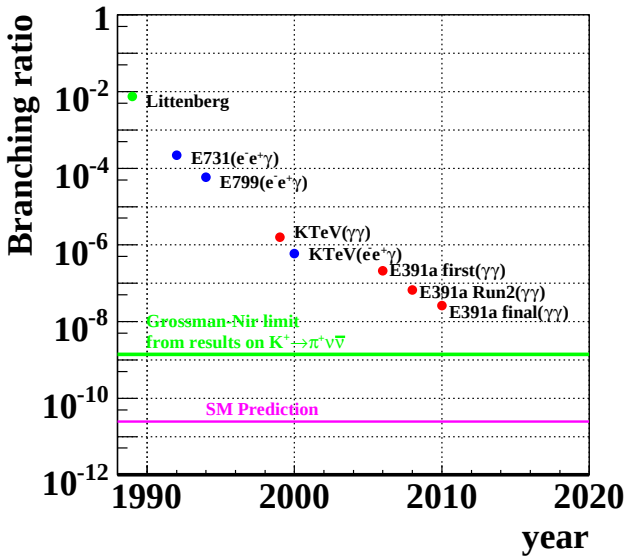

Figure 1.3: History of the $K_L^0 \to \pi^0\nu\bar{\nu}$ search. A green point shows the first study performed by Littenberg. Blue (Red) points in the figure show results of the analysis using a $\pi^0 \to e^+e^-\gamma$ ($\pi^0 \to \gamma\gamma$) decay to identify the K_L^0 decay. A green line shows the Grossman-Nir limit. A pink line shows the branching ratio of the $K_L^0 \to \pi^0\nu\bar{\nu}$ decay predicted in the Standard Model.

1.2.4 KEK-PS E391a experiment

The E391a experiment, which was carried out at the KEK 12-GeV proton synchrotron (KEK-PS), was the first dedicated experiment in the world to search for the $K_L^0 \to \pi^0\nu\bar{\nu}$ decay. The purpose of the experiment was to confirm the experimental concept for measuring the $K_L^0 \to \pi^0\nu\bar{\nu}$ decay.

The signature of the $K_L^0 \to \pi^0\nu\bar{\nu}$ decay was two photons from the π^0 decay and no other particles in the final state. In the E391a experiment, two photons from π^0 were detected by an electromagnetic calorimeter which consisted of undoped CsI crystals. Additional particles, if existed, were detected by hermetic veto counters surrounding the decay region. In order to reduce beam neutron interactions, which cause π^0 production, gas was evacuated from the decay region down to 10^{-4} Pa. Figure 1.4 shows the E391a detector system.

The signal region for the $K_L^0 \to \pi^0\nu\bar{\nu}$ decay was defined in the plane of the reconstructed vertex position (Z_{vtx}) and the transverse momentum of π^0 (P_t). Figure 1.5 shows a final plot in the E391a experiment. Outside the signal region, there are two clusters of events, located at Z_{vtx} = 250–280 cm and Z_{vtx} = 550–570 cm, respectively. They were considered to be due to halo neutrons, which are neutrons in the halo of the neutral beam. When such a neutron hits a detector subsystem, a π^0 may be produced by the interaction between the neutron and the detector material. This was the main background source in the E391a experiment.

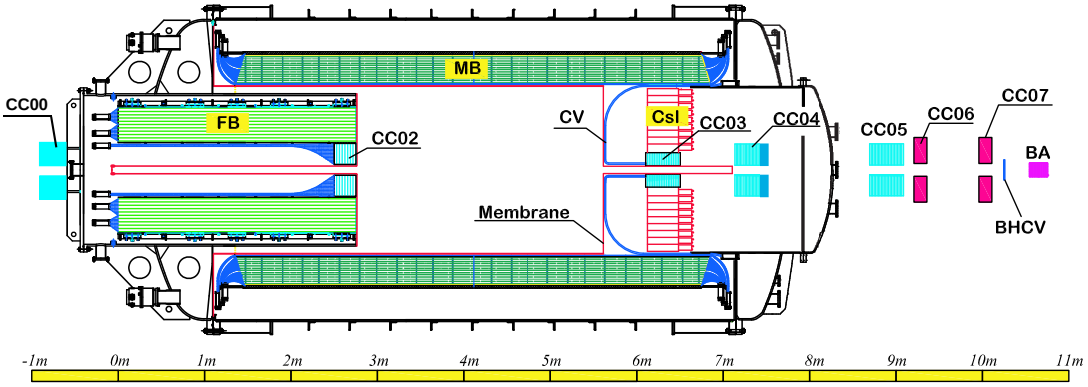

Figure 1.4: Cross-sectional view of the E391a detector system. The detector system consisted of a undoped CsI calorimeter and veto counters. The calorimeter was located at the downstream end of the decay region and detected two photons decayed from π^0. The veto counters surrounded the decay region to reduce background events by detecting extra particles.

1.2.5 J-PARC KOTO experiment

The KOTO experiment is a successor experiment to the E391a experiment, and aims at first observation of the $K_L^0 \to \pi^0\nu\bar{\nu}$ decay [20]. This experiment follows the experimental concept that was established by the E391a experiment. While the sensitivity of the E391a experiment was three orders of magnitude far from the SM prediction, the background level was O(1). We have to improve the sensitivity to the $K_L^0 \to \pi^0\nu\bar{\nu}$ decay and to suppress background events more strongly.

For the improvement of the sensitivity, a new dedicated beam line for the KOTO experiment was constructed at the Japan Proton Accelerator Research Complex (J-PARC). The proton intensity of the Main Ring (MR) accelerator of J-PARC is 100 times higher than that of the

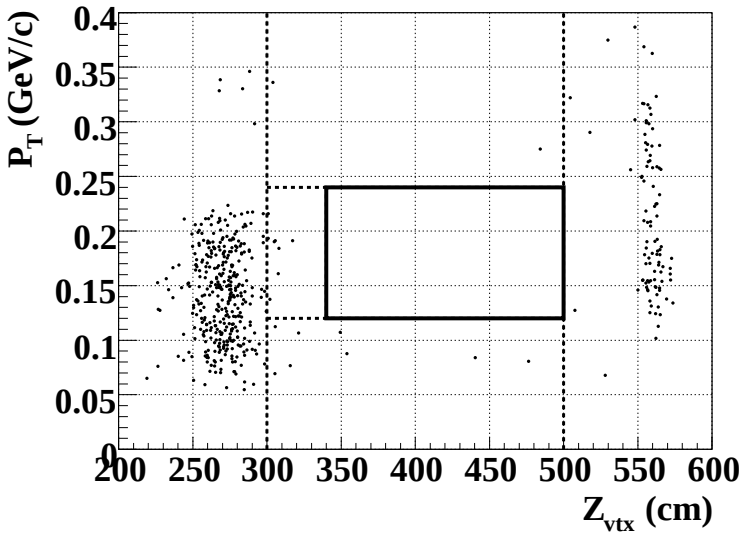

Figure 1.5: Final result of the E391a experiment. The vertical axis shows the reconstructed transverse momentum of the π^0 (P_t). The horizontal axis shows the reconstructed Z position of the π^0. In this plot, all of selection cuts were imposed. The region bounded by the solid line shows the signal box.

KEK-PS. In addition, the primary proton energy of the J-PARC MR accelerator is 30 GeV. The extraction angle of the KOTO beam line is 16 degree, which is larger than that of the E391a beam line (4 degree). This configuration was chosen considering to improve the kaon-to-neutron ratio in the beam, though it loses a part of the K_L^0 yield. Consequently, the K_L^0 flux in the KOTO beam line was expected to be 27 times larger than that in the E391a beam line. This is the largest factor to improve the sensitivity from that of the E391a experiment. Therefore, the K_L^0 flux is a key issue for the KOTO experiment. Other improvement factors are obtained from increase of the signal acceptance by the detector upgrade, and longer run time compared to the E391a experiment. For reduction of background events, the new beam line was designed to suppress the halo neutron flux as much as possible. This is very important, because halo neutrons were main background source in the E391a experiment. The detector upgrade also helps further suppression of background events.

1.3 K_L^0 flux

In order to achieve the high sensitivity to the $K_L^0 \to \pi^0\nu\bar{\nu}$ decay, the K_L^0 flux is very important, as mentioned in the previous section.

The K_L^0 flux was estimated by using several Monte Carlo (MC) simulation packages of hadron interactions. Each package employs different hadronic models and extrapolating/interpolating algorithms to predict the cross section of K_L^0 production at a given energy and angle. In the case of the E391a experiment, MC predictions and obtained data agreed well with each other, as summarized in Table 1.1. On the other hand, in the MC studies on the KOTO beam line, the expected values of the K_L^0 yield were different among the packages, as summarized in Table 1.2. In particular, The K_L^0 flux expected by FLUKA was 3.6 times larger than that expected by GEANT4.

One cause of the discrepancies among the packages was considered to stem from the large production angle in the KOTO case. Similar issues were reported by other groups: data of E802 experiment, which measured hadron production between 12.4 GeV protons and various nucleons, was compared with the cross-section expected from different MC packages by D.E. Jaffe *et al* [21]. While MC predictions were consistent with the data for the small production angle, there were discrepancies among the packages for the large production angle, some of which were inconsistent with the data. The results mean that predictions of the cross section of K_L^0 production at a large angle strongly depend on simulation packages of hadron interactions, and there are large uncertainty. It is desirable to measure the K_L^0 flux experimentally.

As mentioned above, various simulation programs predicted the K_L^0 fluxes that differed by up to a factor of three at the KOTO beam line. We estimated the sensitivity of the KOTO experiment, using the K_L^0 flux and spectrum expected by the GEANT4 simulation. The K_L^0 flux expected by this simulation was smallest among various simulations. However, if the K_L^0 flux expected by the FLUKA simulation is right, the sensitivity of the KOTO experiment may become a few times better than the estimation with the GEANT4 simulation. To reduce a large uncertainty to the K_L^0 flux was important to decide experimental design. Therefore, we planed to measure the K_L^0 flux and spectrum with 10% accuracy soon after construction of the beam line. It was important to prepare for the measurement in a short term and to obtain results quickly.

Table 1.1: The K_L^0 yield per incident proton on the target (POT) in the E391a experiment. The obtained data in the experiment, labeled Run-2 data, and predictions by various MC packages are summarized.

	K_L^0 Yield per POT
Run-2 data	$(1.36 \pm 0.08) \times 10^{-7}$
Geant3	1.32×10^{-7}
Geant4(QGSP)	1.31×10^{-7}
FLUKA	1.40×10^{-7}

Table 1.2: Comparison of expected K_L^0 yields in the KOTO experiment by various MC packages.

	K_L^0 Yield per POT
Geant3	7.55×10^{-8}
Geant4(QGSP_BERT_CHIPS)	3.70×10^{-8}
FLUKA	1.03×10^{-7}

1.4 Outline of the thesis

In this thesis, the measurement of K_L^0 flux in the neutral beam line constructed for the KOTO experiment at J-PARC is described. The measurement is essential to estimate the sensitivity of

the KOTO experiment and provides new data of the K_L^0 production with 30-GeV protons at a large angle.

The thesis is organized as follows. In the next chapter, Chapter 2, the features of the KOTO experiment is briefly introduced. In Chapter 3, the design of the neutral beam line for the KOTO experiment is explained. In Chapter 4, the experimental concept, the detector configuration and the data set of the K_L^0 flux measurement are described. In Chapter 5, MC simulations used in this analysis, the event reconstruction, and the event selection are described. In Chapter 6, the results of this measurement are described and the comparison of data with the simulations is discussed. In Chapter 7, the sensitivity of the KOTO experiment based on the results of this measurement is discussed. The conclusions are given in Chapter 8.

Chapter 2

KOTO experiment

The KOTO experiment aims at the first observation of the rare decay $K_L^0 \to \pi^0\nu\bar{\nu}$ by using the upgraded KEK-E391a detector and a high-intensity K_L^0 beam at J-PARC.

In this chapter, I first explain a detection method for the $K_L^0 \to \pi^0\nu\bar{\nu}$ decay and possible background events. Next, I explain the features of the KOTO experiment. Finally, the requirements of the neutral beam line are summarized from the viewpoint of the $K_L^0 \to \pi^0\nu\bar{\nu}$ search.

2.1 Detection method

The $K_L^0 \to \pi^0\nu\bar{\nu}$ decay is identified by detecting two photons from the π^0 decay. No other particles are allowed to exist in the final state. The K_L^0 decay modes that have exclusively two photons in the final state are $K_L^0 \to \pi^0\nu\bar{\nu}$ and $K_L^0 \to \gamma\gamma$ decays. All other decay modes include at least two charged particles or at least four photons, and these decays can be distinguished from the signal by detecting extra particles other than two photons. We can discriminate the $K_L^0 \to \pi^0\nu\bar{\nu}$ decay from the $K_L^0 \to \gamma\gamma$ decay by requiring a finite transverse momentum (P_t) of the detected two-photon system.

In the KOTO experiment, the energies and positions of the two photons are measured with an electromagnetic calorimeter, which is located at the downstream end of the decay region in order to detect two photons boosted in the K_L^0 direction efficiently. The decay position of the π^0 is reconstructed along the beam axis, assuming the invariant mass of the two photons equals to the π^0 mass. The event whose decay position is in a proper region is regarded as a π^0 decay. In addition, we require there are no other activities in hermetic veto counters surrounding the decay region. Among those events with a π^0 only, $K_L^0 \to \pi^0\nu\bar{\nu}$ candidates are selected by imposing various cuts on photon's and π^0's kinematics. Details are explained in Chapter 8.

2.2 Backgrounds

Background suppression is a key issue of the KOTO experiment because the branching ratio of the $K_L^0 \to \pi^0\nu\bar{\nu}$ decay expected from the Standard Model is very low, ($\sim 10^{-11}$). In the KOTO experiment, background events are classified into two categories: K_L^0-decay backgrounds and beam-interaction backgrounds.

K_L^0 decay modes	Branching ratio	p_{max}(Mev/c)
$K_L^0 \to \pi^0\nu\bar{\nu}$	$(2.4\pm\ 0.4)\times10^{-11}$	231
$K_L^0 \to \pi^\pm e^\mp \nu$	(40.55±0.11)%	-
$K_L^0 \to \pi^\pm \mu^\mp \nu$	(27.02±0.07)%	-
$K_L^0 \to 3\pi^0$	(19.56±0.14)%	139
$K_L^0 \to \pi^+\pi^-\pi^0$	(12.56±0.05)%	133
$K_L^0 \to 2\pi^0$	$(8.69\pm0.04)\times10^{-4}$	209
$K_L^0 \to \gamma\gamma$	$(5.48\pm0.05)\times10^{-4}$	-

Table 2.1: Branching ratios of K_L^0 decay modes; the $K_L^0 \to \pi^0\nu\bar{\nu}$ decay, the top 4 modes, and relevant two neutral modes are listed. For $K_L^0 \to \pi^0\nu\bar{\nu}$, the predicted branching ratio by the Standard Model is shown, and other values are quoted from [22]. For the decay modes that include one or more π^0, the kinematic limits of the π^0 momentum in the K_L^0 rest frame are also indicated.

2.2.1 K_L^0 decay

Table 2.1 shows a list of the branching ratios of K_L^0 decay modes. Among the modes with four largest branching ratios, three contain charged particles in the final state. In order to distinguish them from the $K_L^0 \to \pi^0\nu\bar{\nu}$ decay, detection of charged particles with high efficiency is necessary.

$K_L^0 \to 3\pi^0$ and $K_L^0 \to 2\pi^0$ decays can become backgrounds if extra photons are undetected. Photon detection with high efficiency is important in order to reduce background events. In the $K_L^0 \to \gamma\gamma$ decay, there are only two photons in the final state. This decay mode can be discriminated by requiring a large transverse momentum, as shown in Fig 2.1.

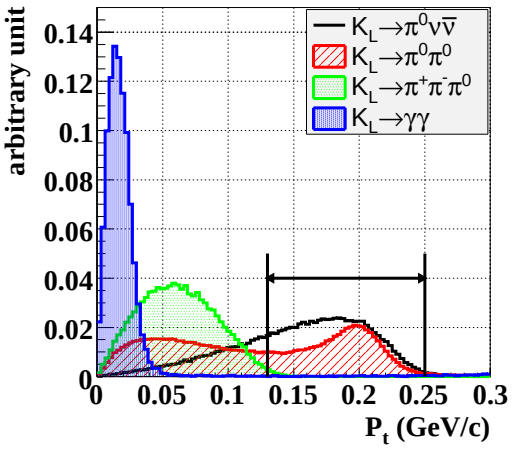

Figure 2.1: Reconstructed P_t distributions of two-photon system for $K_L^0 \to \pi^0\nu\bar{\nu}$, $K_L^0 \to 2\pi^0$, $K_L^0 \to \pi^+\pi^-\pi^0$, and $K_L^0 \to \gamma\gamma$ decays, respectively, obtained by a Monte Carlo simulation. All the distributions are normalized to be 1 when integrated. The signal region in the KOTO experiment is set between two vertical lines in the figure.

2.2.2 Beam interaction

In the neutral beam, there is a large amount of neutrons produced by the hadronic interactions in the target. If such a neutron interacts with residual gas, it may produce π^0 or η that can be a source of background. In order to reduce this type of backgrounds, the decay region is necessary

to be a high vacuum. With the pressure of 10^{-4} Pa, the number of background events due to interactions between neutrons and residual gas is expected to be negligible in the case of the KOTO experiment.

Around the beam region, there exist accompanied neutrons, which are called "halo neutron". If a halo neutron interacts with detectors located near the beam, it may produce particles that can be a source of background. This type of backgrounds was the main background source in the E391a experiment. The mechanisms that cause backgrounds are the following.

- π^0 production
  If a π^0 is produced by the interaction, it fakes the signal. Usually, interactions with detector materials can be separated from the signal since the reconstructed decay position points the detector position properly. However, if the energies of the photons are mis-measured due to leakage of an electromagnetic shower, photo nuclear effect, and additional energy deposition by other particles, the reconstructed vertex may be shifted into the signal region.

- η production
  η mesons are also produced in the interactions. They decay into two photons with $Br(\eta \to \gamma\gamma)$ of about 40%. Since the decay position is reconstructed with the assumption that the invariant mass of two photons equals to the π^0 mass, it will be miscalculated.

The primary method of reducing these types of backgrounds is to use the beam line with less halo neutrons. The key issues of the detector are to have good energy resolution and to detect associated particles from the interaction.

2.3 Features of the KOTO experiment

To reduce the backgrounds mentioned in the previous section, the KOTO experiment has several features. In this section, I introduce the key components in the KOTO experiment.

2.3.1 Hermetic veto system

The most important tool to reduce backgrounds is detection of extra particles, because two photons are accompanied with two additional photons or charged particles in most of backgrounds. For this purpose, the decay region is surrounded by highly sensitive veto detectors, as shown in Fig. 2.2. We even cover the beam region, where the neutral beam passes through.

2.3.2 Pencil beam line

The KOTO experiment introduce a small-diameter K_L^0 beam called "pencil beam". Although the K_L^0 flux is reduced, the pencil beam has several advantages.

First, a small size allows us to minimize the beam hole in the calorimeter, and reduces the chance that particles from K_L^0 decays go through the beam hole. Such particles are likely to hit a veto detector inside the beam, with less detection efficiency due to exposure to a huge amount of photons and neutrons.

Second, the measurement error of the π^0 transverse momentum (P_t) is kept small. The decay position is reconstructed on the beam axis by assuming that the two photons hitting the calorimeter has the invariant mass of π^0, and the error of P_t comes from a finite beam size. The pencil beam reduces this error.

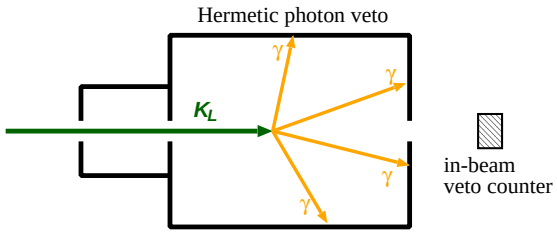

Figure 2.2: Concept of the hermetic veto detector system in the KOTO experiment.

2.3.3 Reduction of halo neutrons

As mentioned in Section 2.2.2, the interactions between detector materials and halo neutrons were main sources of backgrounds in the E391a experiment. Therefore we optimized the beam line design to suppress the beam halo to as low levels as possible. By the configuration of the collimators, the edge of the neutral beam was sharply shaped, and the rate of the beam halo is 4 orders of magnitude lower than the rate of the beam core in the KOTO experiment. The KOTO beam line is described in detail in Chapter 3.

2.4 Requirement on the neutral beam

In this section, I summarize the requirement on the neutral beam to search for the $K_L^0 \to \pi^0\nu\bar{\nu}$ decay with high sensitivity.

It is necessary to collect large amount of K_L^0's because the branching ratio of the $K_L^0 \to \pi^0\nu\bar{\nu}$ decay is very small. The beam with a high K_L^0 flux is desirable. In the KOTO experiment, it is also necessary to consider background suppression, as mentioned in Section 2.2. For the suppression of background events, the small-diameter K_L^0 beam called "pencil beam" is required. The neutral beam should be well collimated, keeping a sufficient K_L^0 flux which is needed to achieve high sensitivity. The beam halo must be suppressed as much as possible to reduce the number of halo neutrons, which interact with detector materials and become background sources.

As mentioned in the next chapter, the KOTO beam line was constructed based on the beam line design which satisfies these requirements. In order to confirm the sensitivity and the background level of the KOTO experiment, it is necessary to measure the K_L^0 flux and spectrum in the neutral beam.

Chapter 3

Neutral-kaon beam line at J-PARC

In order to search for the $K_L^0 \to \pi^0\nu\bar{\nu}$ decay with high sensitivity, a high-intensity K_L^0 beam is essential. We constructed a new neutral-kaon beam line at J-PARC.

In this chapter, I firstly introduce the J-PARC briefly. Next, a primary proton beam of the neutral beam and production targets of K_L^0 are described. Then, the neutral beam line for the KOTO experiment is described.

3.1 J-PARC

The Japan Proton Accelerator Research Complex (J-PARC) is a newly constructed high-intensity proton accelerator facility in Japan. This facility has various kinds of secondary particle beams, such as neutron, muon, neutrino, and kaon beams with high intensity. These beams are used for researches in various fields of science such as nuclear physics, particle physics, and materials and life sciences.

As shown in Fig. 3.1, the accelerator complex of the J-PARC consists of three components: a linear accelerator (LINAC), a 3-GeV Rapid-Cycling Synchrotron (RCS), and a 30-GeV synchrotron, which is called Main Ring (MR).

The 3-GeV proton beam from the RCS is extracted to the material and life science experimental facility (MLF) and produce pulsed neutron and muon beams. These beams are utilized for condensed matter physics, materials sciences, structural biology, and so on. A part of the 3-GeV beam is injected to the MR accelerator, and is accelerated to 30 GeV. The 30-GeV proton beam from the MR is provided to a neutrino experimental facility and a hadron experimental hall. In the neutrino facility, an intense neutrino beam is produced and is used for a long-baseline neutrino oscillation experiment between Tokai and Kamioka (T2K) [23]. In the hadron experimental hall, secondary hadron beams are utilized for nuclear and particle physics experiments.

3.2 Primary proton beam

The KOTO experiment is carried out in the hadron experimental hall. A 30-GeV proton beam from the MR is used as a primary beam. The beam is extracted from the MR by using a slow extraction technique, having 0.7 second duration every 3.3 second repetition cycle (design values). A beam extraction in one cycle is called "spill". The design intensity of the primary beam is 2.0×10^{14} protons per a spill.

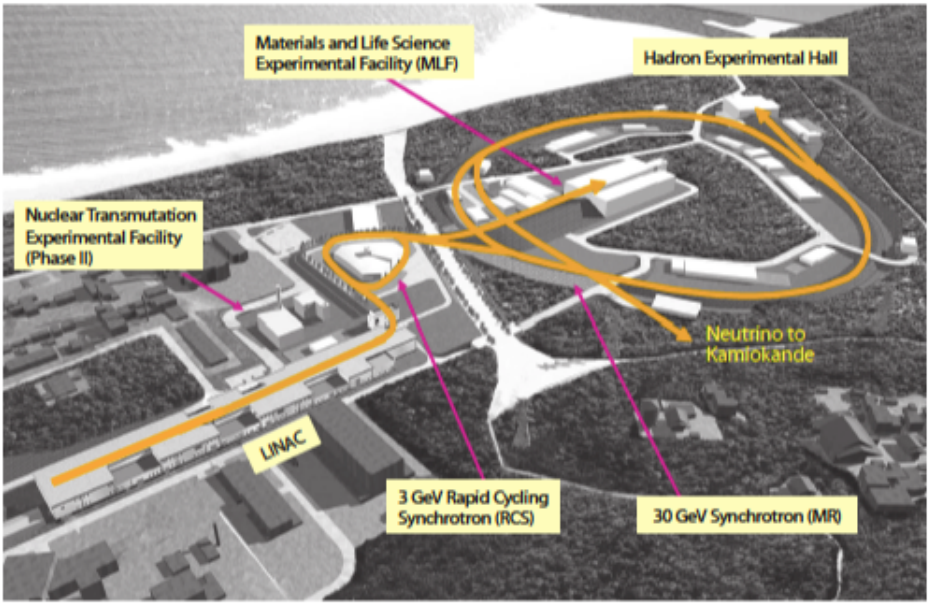

Figure 3.1: Bird eye's view of the J-PARC site. J-PARC consists of the LINAC, RCS, and MR. There are three experimental facilities: a material and life science experimental facility (MLF), a hadron experimental hall, and a neutrino experimental facility.

3.3 Production target

The primary proton beam is injected into a production target, called T1 target. The generated secondary particles are delivered to experimental areas through two charged (K1.8 and K1.1) and one neutral (KL) beam lines simultaneously, as shown in Fig. 3.2. The T1 target is composed of five nickel (Ni) disks of 360 mm in diameter, as shown in Fig. 3.3. The thickness in total is 54 mm, which corresponds to 0.36 interaction length (λ_I). The disks rotate in the water tank to prevent being melted by heat due to high beam power. Thicknesses of the disks were determined individually to share heat deposition uniformly.

At present, the accelerator is under commissioning, and the beam intensity is only a few percent of the design value. Therefore a nickel block, which has four grooves and its effective thickness of 54 mm to simulate the disk target, was used as an alternative without water cooling. In addition, a platinum (Pt) rod of 6 mm in diameter and 60 mm in thickness was prepared to increase intensities in the secondary beam lines. The thickness of the Pt target corresponds to 0.7 interaction length. Figure 3.4 shows a picture of the nickel block and platinum rod mounted on the target holders. These targets were used in the K_L^0 flux measurement in this research.

A copper collimator is placed just behind the target to prevent magnets for the charged beam lines from being exposed to high radiation. It is made of 400-mm-thick Cu plate and covers 1×1 m^2 region. It has a hole at the center for the primary beam to pass through. For the KOTO beam line, a square hole of 4×4 cm^2 is prepared. Figure 3.5 shows a schematic plan view of the T1 target and the Cu collimator.

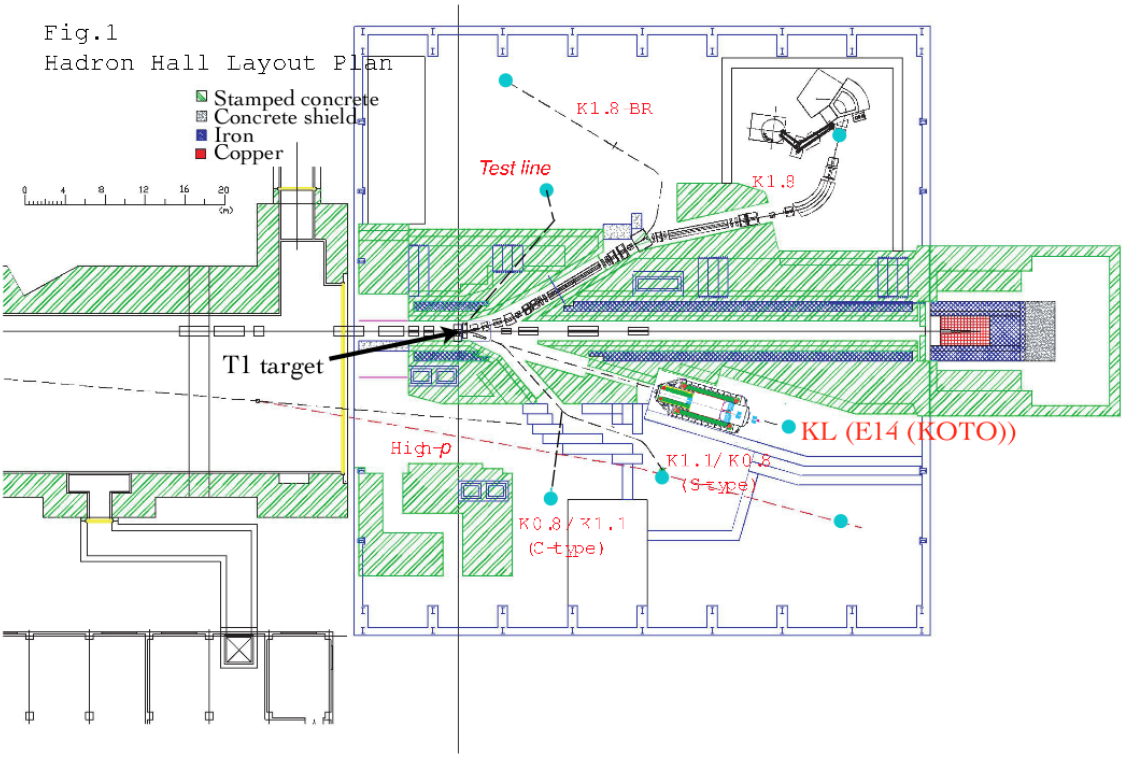

Figure 3.2: Layout in the hadron experiment hall.

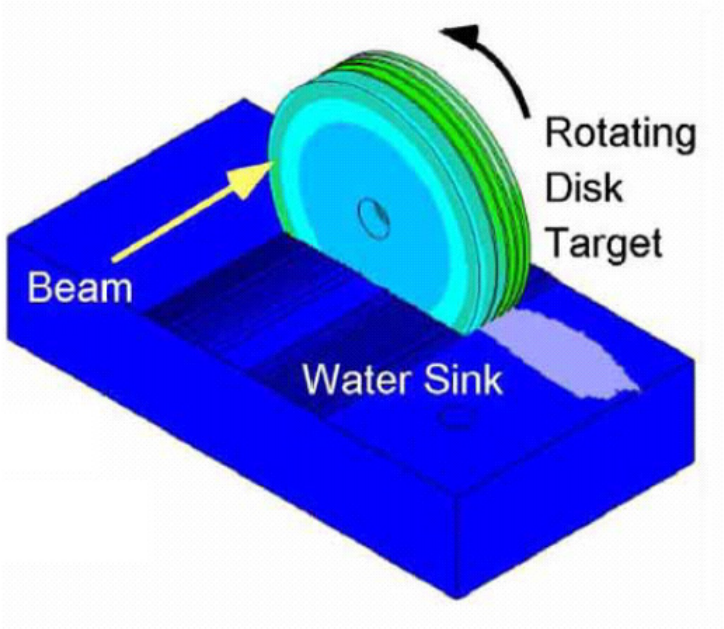

Figure 3.3: Schematic drawing of the T1 target

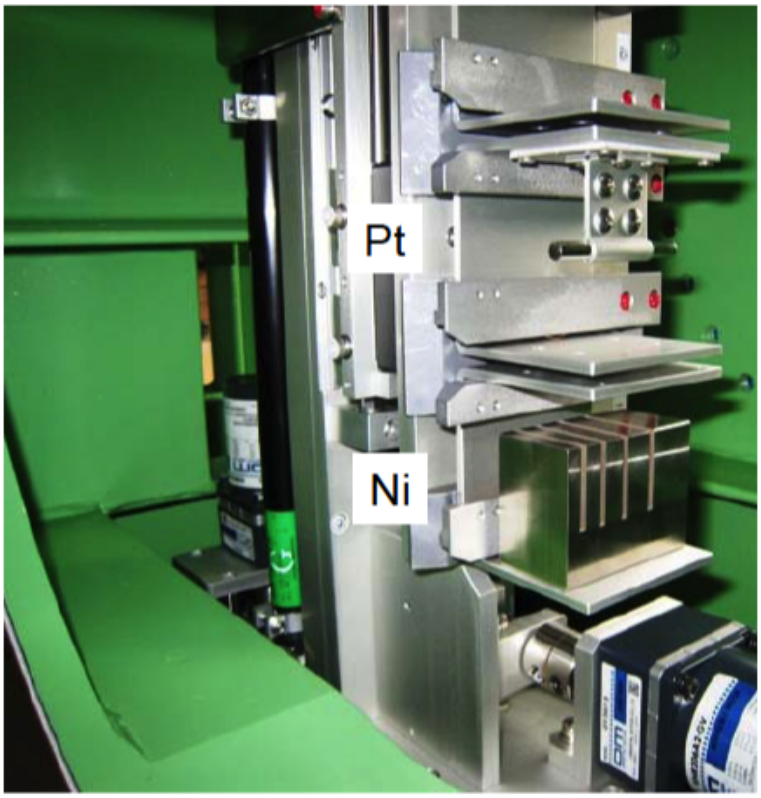

Figure 3.4: Picture of the Ni and the Pt targets. The Ni target is made of a nickel block with four grooves, whose thickness is 54 mm in total. The Pt target is a rod of 6 mm in diameter and 60 mm in thickness. Both targets are used without water cooling.

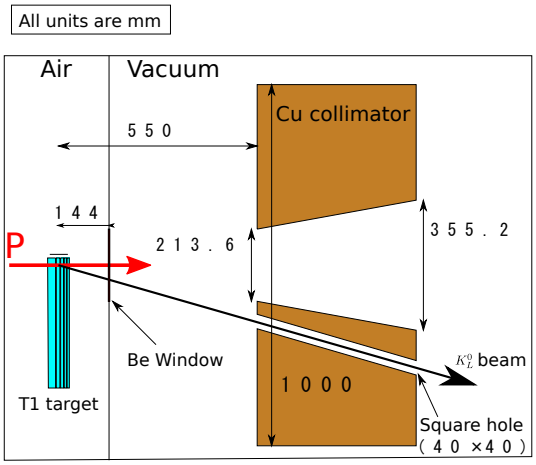

Figure 3.5: Plan view of the T1 target area. The target is located in air, while the Cu collimator is located in a vacuum chamber just behind the target. The remaining proton beam that passes through the target, as well as secondary particles for the charged beam lines, goes through the central hole. Neutral particles to the K_L^0 beam line go through the square hole of 4×4 cm^2.

3.4 Neutral-kaon beam line

As shown in Fig. 3.2, the neutral-kaon beam line for the KOTO experiment is located in the south area in the hadron experimental hall. The extraction angle for the neutral (K_L^0) beam is 16 degree with respect to the primary proton beam.

3.4.1 Design concept

As mentioned in Chapter 2, there are two important issues to be considered in designing the beam line for the KOTO experiment. One is to create a narrow beam ("pencil beam"), and the other is to suppress the beam halo. The former is to obtain better resolution in the transverse-momentum measurement for selecting the $K_L^0 \to \pi^0\nu\bar{\nu}$ decay. Also, a small beam size in the detector is necessary for detection of extra particles in background events. The latter is to suppress the background events due to interactions of halo neutrons.

The only method to shape a neutral beam is collimation by heavy materials. Unlike a charged beam, neither focusing/defocusing nor bending by electromagnetic force is applicable. Therefore design of a neutral beam line is basically consideration of collimator configurations. A solid angle of collimators determines the beam size at the detector position. Since a part of neutrons can penetrate materials, collimators must have enough length. To use heavier materials is also helpful. Scattering on the inner surface of a collimator hole may cause halo neutrons. The shape and placement of collimators must be optimized. A basic scheme of the collimator configuration was developed by geometrical consideration, and was evaluated by a simulation. In addition, efforts to remove unwanted particles (other than K_L^0) from the beam were also made. Installation of a magnet sweeps out charged particles. Insertion of a high-Z material inside the beam reduces a fraction of photons drastically, with small sacrifice of the K_L^0 yield.

In the following sections, the actual design of the K_L^0 beam line is described, and its expected performances are discussed.

3.4.2 Beam line components

The neutral-kaon beam line is a complex of a photon absorber, a dipole magnet, and collimators, as shown in Fig. 3.6. The beam is collimated by two stages of long collimators made of iron, partly embedding tungsten alloys. The length of the first and second collimators are 4 m and 5 m, respectively. In order to avoid interference with the upstream magnets for the K1.1 beam line, the collimation system starts 6.5 m downstream of the target. In order to reduce a photon flux in the beam, a photon absorber, which is a 7-cm-thick lead block, is located at the position of 4 m from the target. Charged particles in the beam are swept out by a dipole magnet installed between the collimators.

3.4.3 Collimation scheme

Figure 3.7 illustrates three collimation lines that were determined to suppress halo neutron production. The effective target image, which reflects a trajectory of the primary proton beam in the target, has different size in horizontal and vertical directions. The horizontal image is determined by the extraction angle; it corresponds to the projection of the target thickness to 16 degree direction and is 18 mm in length. The vertical image is determined by the primary beam size; its width is 1.3 mm. We optimized the collimation lines separately in each direction so that the shape of the beam at the detector position becomes a square.

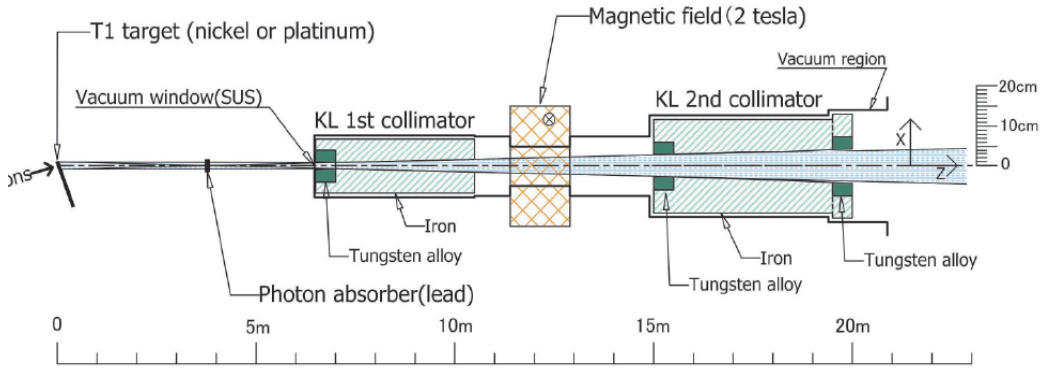

Figure 3.6: Schematic layout of the neutral-kaon beam line. It consists of a pair of collimators and a sweeping magnet (2 Tesla). A 7-cm-thick lead absorber is inserted in the beam line to reduce photons. Also shown is the coordinate system used in this thesis: x in the horizontal, y in the vertical, and z in the beam directions. The origin of the coordinate is set at the center of the production target. The exit window of the beam line (not shown) is located at $z = 20.6$ m.

The first collimator primarily determines the size and the profile of the beam (Line-1). The size of the beam at the entrance of the KOTO detector ($z = 21$ m) is determined to be 8.5×8.5 cm^2, which was optimized by considering both the K_L^0 yield and rejection of backgrounds. Since the halo neutrons are produced by multiple scattering of neutrons on beam line materials, the inner surface of the collimators should not be seen directly from the target. The front edge of the first collimator is needed to be dense because it must stop most of neutrons. A 50-cm-long tungsten alloy is used for the most upstream part of the first collimator.

The photon absorber in the beam becomes a scattering source. If a neutron that is scattered by the absorber re-scatters at the second collimator, it may become a halo neutron. The Line-2 adjusts the collimation line of the second collimator to avoid re-scattering. The both edges of the second collimator are needed to be dense to stop the incoming neutron effectively. 50-cm-long tungsten alloys are used for the most upstream and downstream part of the second collimator.

A neutron that scatters at the front edge of the first collimator becomes a halo neutron through re-scattering at the second collimator. The rear half of the second collimator is further trimmed, to be a shape determined by Line-3.

3.4.4 Expected performance

The collimation scheme was optimized by using the GEANT3-based MC simulation [24]. The beam parameters relevant to this study are summarized in Table 3.1. The resultant beam profile of neutrons at the exit of the beam line is shown in Fig. 3.8. Here, the threshold of neutron momentum was set to be 0.78 GeV/c, which corresponds to the threshold of π^0 production. While the profile in the core in the vertical plane was flat, that in the horizontal plane showed a gradual decrease due to a larger target image. The ratio of the number of halo neutrons that entered one of the KOTO detector components to that of K_L^0's in the core was obtained to be $(6.99 \pm 0.47) \times 10^{-4}$.

In order to estimate beam fluxes, three simulation packages of hadron interactions were used; those were GEANT3 with the GFLUKA package [25], GEANT4 with the QGSP-BERT-CHIPS physics list [26], and FLUKA [27]. Each code employs different hadronic models and

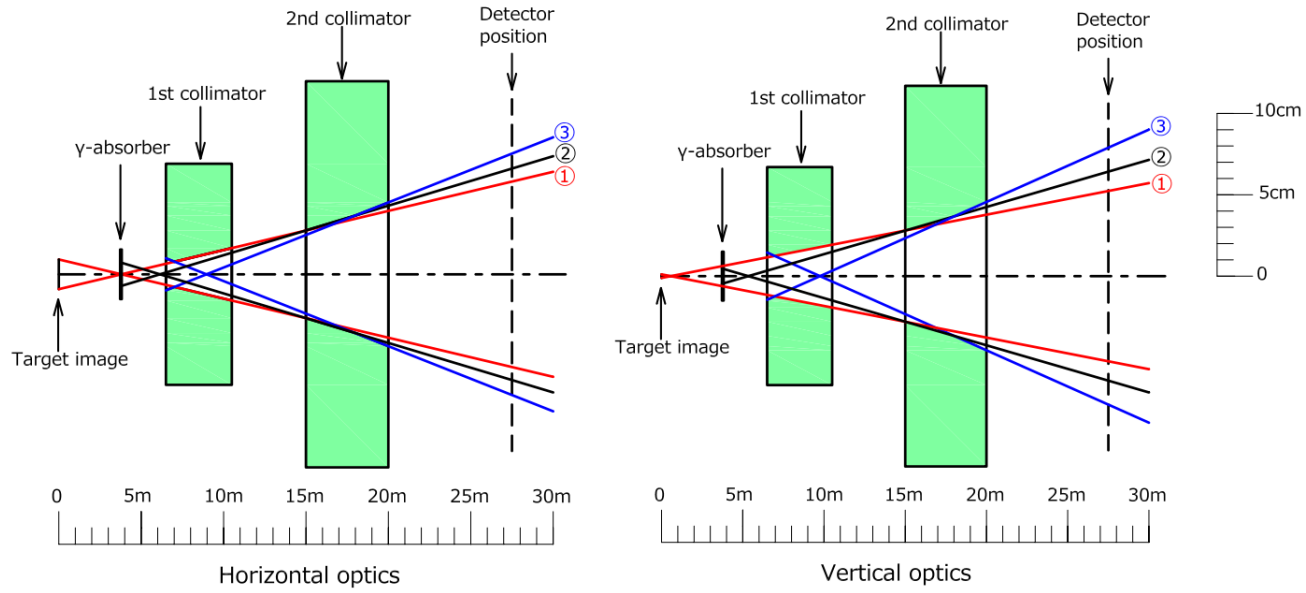

Figure 3.7: Optics of the K_L^0 beam line in the horizontal and vertical planes. The colored areas indicate cross-sectional views of the collimators. Three lines in each figure indicate collimation schemes, as explained in the text.

extrapolating/interpolating algorithms to predict the cross section of hadron production at a designated energy and angle. The resultant fluxes are summarized in Table 3.2, and the resultant momentum distributions of each species of particles are shown in Fig. 3.9. The neutron fluxes obtained by the simulations were consistent within 20%. The neutron spectrum obtained by the FLUKA simulation was harder than that obtained by the other simulations. The same tendencies were seen in the expectations of the gamma fluxes and spectrum obtained by the simulations. On the other hand, the K_L^0 fluxes obtained by the simulations differed from each other by as much as a factor of three. The fact therefore motivated us to measure the K_L^0 flux.

Parameter	value	Remarks
Primary proton energy	30 GeV	
Proton intensity	2×10^{14}	
Spill length / Beam repetition	0.7 s / 3.3 s	
Production target	Common T1 target	
Extraction angle	16	
Solid angle	7.8 μsr	

Table 3.1: Parameters of the neutral beam (designed values).

3.5 Collimator alignment

Before proceeding to the description of the K_L^0 flux measurement, the collimator alignment is mentioned here.

Package name	K_L^0 flux	Neutron flux (T_n >100 MeV)	Photon flux ($E_\gamma > 10$ MeV)
GEANT4	7.4×10^6	3.2×10^8	5.9×10^7
GEANT3	1.5×10^7	3.8×10^8	5.1×10^7
FLUKA	2.1×10^7	3.7×10^8	7.1×10^7

Table 3.2: Yields of secondary particles per spill obtained by three different MC packages. The fluxes were normalized to 2×10^{14} primary protons which corresponds to the designed intensity in a spill.

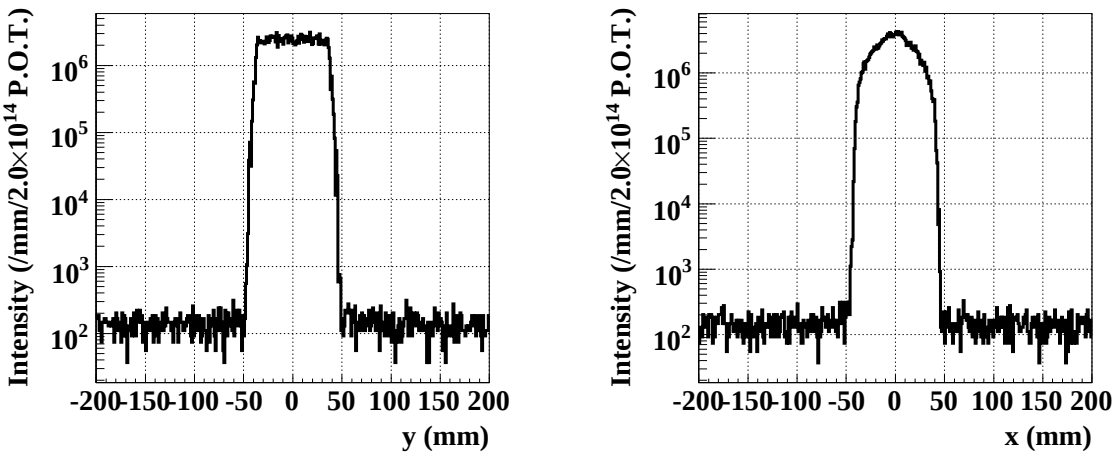

Figure 3.8: Beam profiles of neutrons with their momenta above 0.78 MeV/c in the y plane (left) and the x plane (light) at the exit of the neutral beam line, obtained by the beam line simulation.

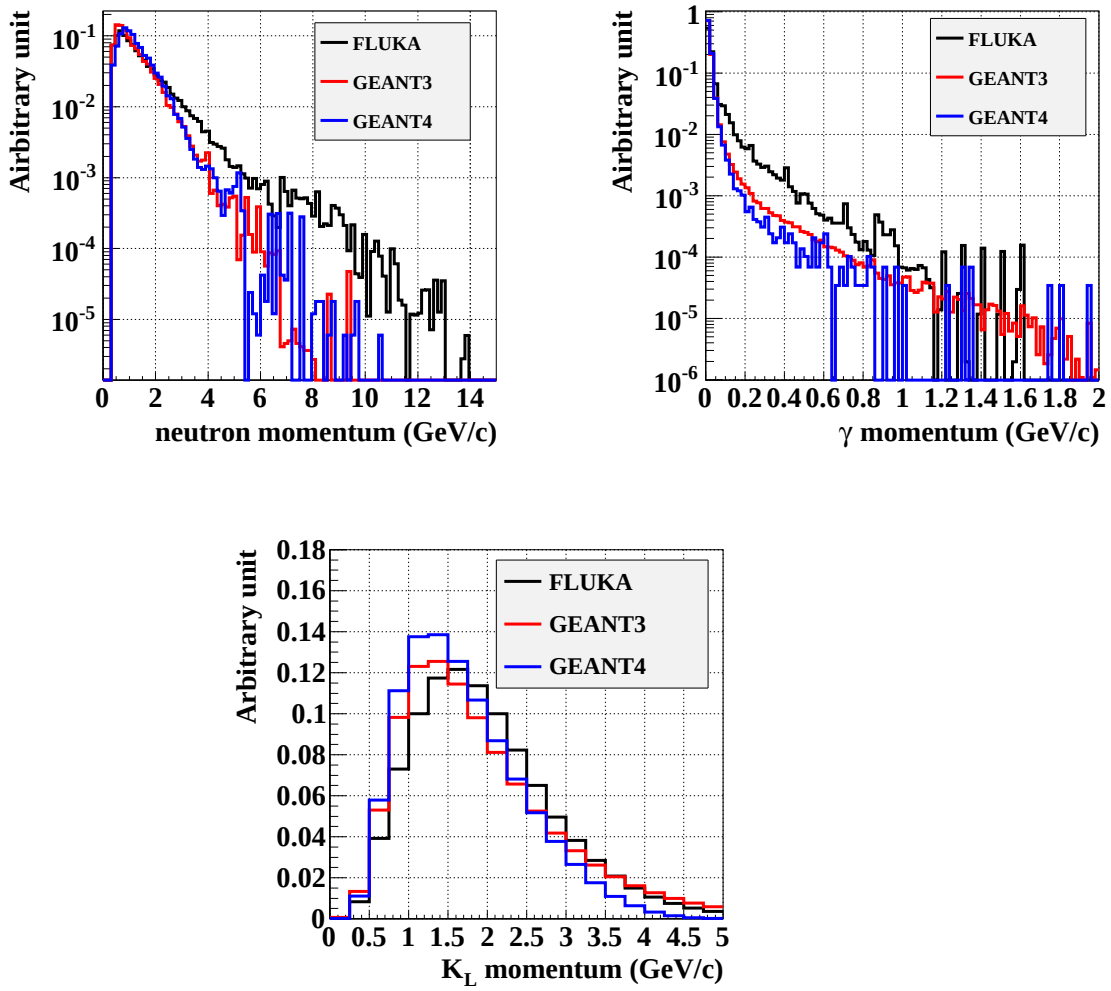

Figure 3.9: Momentum spectrums of neutrons with their kinematic energies above 100 MeV (top left), gammas with their kinematic energies above 10 MeV (top right), and K_L^0 (bottom), respectively, at the exit of the neutral beam line. The results by three simulation packages, FLUKA, GEANT3, and GEANT4, were overlaid in each plot.

In order to achieve the designed performance of the collimation, the collimators must be aligned properly, to an accuracy of a milimeter. Each collimator is mounted on two movable stages: one at the upstream and the other at the downstream points. They can move independently in both horizontal and vertical directions with accuracy of 10 μm, so that the position and the angle of the collimator can be adjusted precisely.

The initial positioning of the collimators was made by a survey with an optical theodolite and levels at the beam line construction. Then, the position of the collimators was adjusted with the neutral beam itself using a beam profile monitor, named "GOH-monitor (Graphic Online High-flux beam monitor)" [28].

The monitor was arrays of scintillating fibers, as shown in Fig. 3.10. The fibers were 1.5 mm square in the cross section and 450 mm in length. There were 120 fibers in total in one plane, and there were two identical planes orthogonal to each other. The overlapped area was 180 $\times$ 180 mm^2 to cover the expected size of the neutral beam, 90 $\times$ 90 mm^2, at the beam-line exit. One end of each fiber was viewed by a 64-ch multi-anode photomultiplier tube (MA-PMT).

The alignment procedure was done as follows. Fig. 3.11 shows an example of obtained beam profiles. The edges of the beam were defined as the positions at which the height in the profile was 10% of the maximum. The edge position varied as the collimator position was changed. By looking at the change of the edge, we searched the optimal position of the collimator. Once two collimators were aligned, the overall angle of the two-collimator direction was adjusted by maximizing the integrated yield in the beam, in order to direct the system to the center of the target. Figure 3.12 shows the final beam profiles after the alignment. With a consideration of the resolving power in the profile measurement, precision of the collimator positions was estimated to be better than 1 mm.

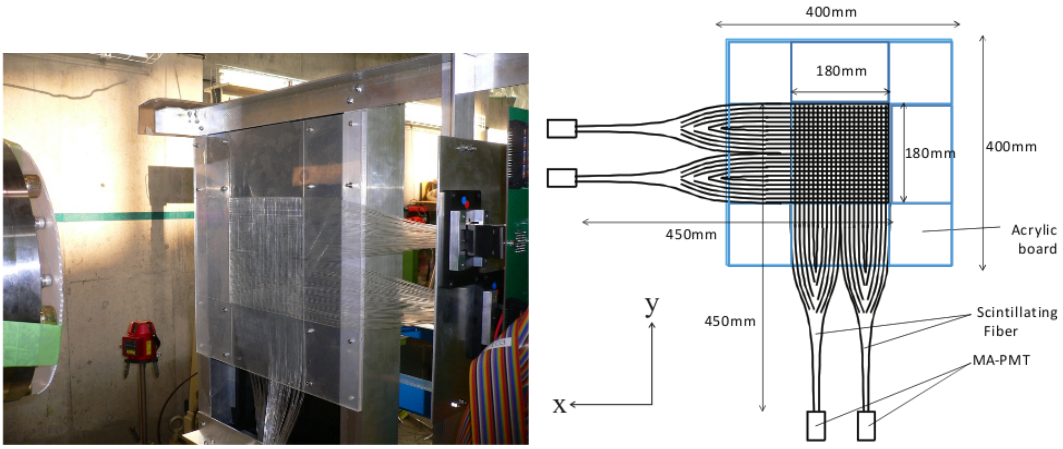

Figure 3.10: Photo (left) and schematic view (right) of the GOH-monitor which was used for the collimator alignment.

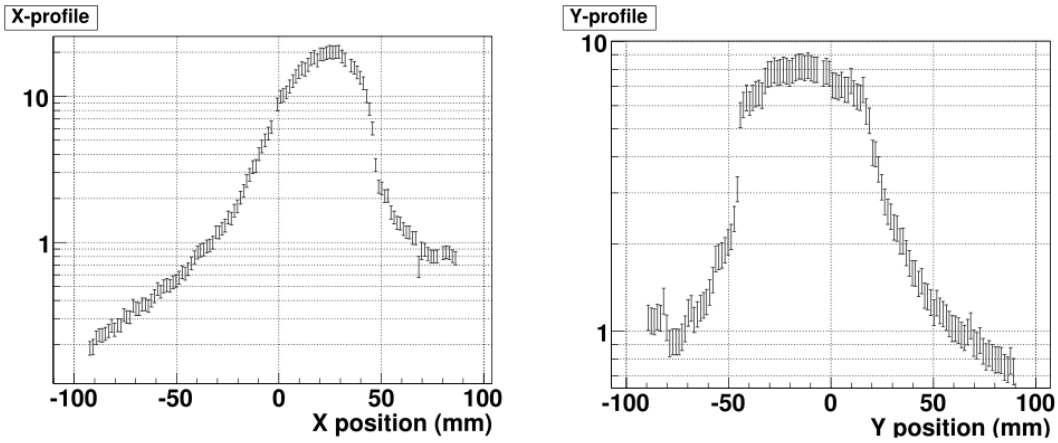

Figure 3.11: Beam profiles when the collimators were off from the optimum position by intention.

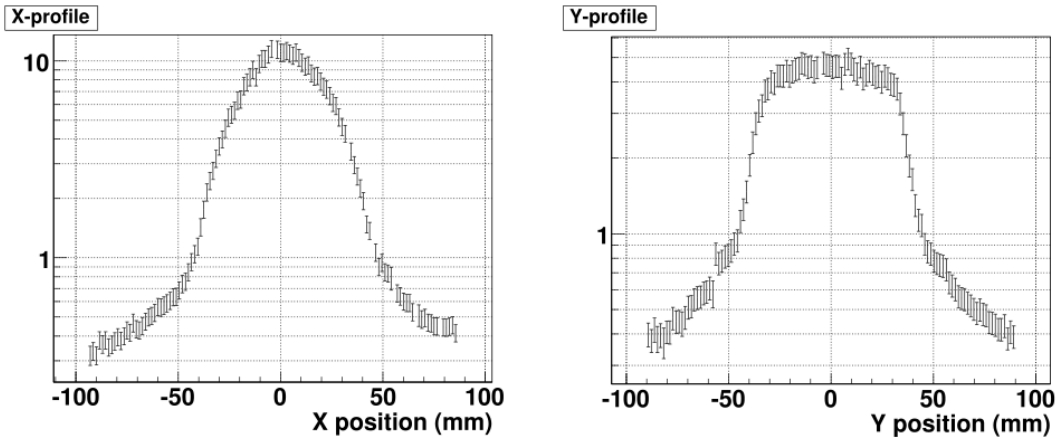

Figure 3.12: Beam profiles after the collimator alignment.

Chapter 4

K_L^0 flux measurement

The K_L^0 flux measurement in this research was conducted in February 2010, before the installation of the KOTO detector in the experimental area. An aim of the measurement was to measure the K_L^0 flux and spectrum with 10% accuracy because there were differences of a factor of three in the predictions of the K_L^0 flux by various simulation programs. We needed to cary out the measurement quickly after construction of the beam line. For this purpose, I developed an original method to identify the $K_L^0 \to \pi^+\pi^-\pi^0$ decay with a compact detector system. Uniqueness of the method was to obtain momenta of charged pions without any magnetic spectrometer.

In this chapter, the experimental principle of the K_L^0 flux measurement is explained firstly. Next, design concepts of a detector system are described, and each detector component is introduced. A data acquisition system for the K_L^0 measurement and calibration methods are also described. In the last section, data used in the analysis of the K_L^0 flux measurement are explained.

4.1 Experimental principle

In order to evaluate the K_L^0 flux and spectrum, we have measured the $K_L^0 \to \pi^+\pi^-\pi^0$ decay. This mode was chosen because its branching ratio is large, and all decay products can be easily detected, allowing reliable event reconstruction. The $K_L^0 \to \pi^+\pi^-\pi^0$ decay was reconstructed by detecting two photons from the π^0 decay and two charged particles. With the vertex position of charged tracks, the invariant mass of the two photons was calculated and was compared with the π^0 mass. Then, equations for the transverse momentum balance of the $\pi^+\pi^-\pi^0$ system were solved to derive the absolute momenta of the charged particles without any magnetic spectrometer. Finally, the invariant mass of $\pi^+\pi^-\pi^0$ was calculated and was compared with the K_L^0 mass in order to identify the $K_L^0 \to \pi^+\pi^-\pi^0$ decay.

4.2 Detector design

In this section, design concepts of our setup in this measurement are described. As mentioned in the previous section, we searched for the events including two charged particles and two photons to identify the $K_L^0 \to \pi^+\pi^-\pi^0$ decay. For this purpose, we designed a detector system that consisted of a tracking system for charged particle measurement and an electromagnetic calorimeter for photon measurement, as shown in Fig. 4.1. The tracking system had two arms, each of which had two layers to measure the positions and directions of charged particles. The

electromagnetic calorimeter had two banks to catch two photons individually. The detector system did not have any magnetic spectrometer because momenta of charged particles could be derived by solving the transverse momentum balance of the $\pi^+\pi^-\pi^0$ system. we could fully reconstruct K_L^0 with good momentum resolution, as described below, except for events with specific kinematic; if two charged particles went in the opposite direction in the transverse plane of the beam direction, simultaneous linear equations to the transverse momentum balance lost linear independence and could not be solved. Furthermore, the reconstruction method have another advantage. In the method, the length of a whole detector system to the beam direction o could be made short, and the sufficient geometrical acceptance for the measurement could be obtained by using compact detectors.

We first decided sizes and locations of the detector components, considering the expected number of $K_L^0 \to \pi^+\pi^-\pi^0$ decays that can be accumulated per day. As a boundary condition, the primary beam power was limited to be about 1 % of the designed value in this measurement. The total number of K_L^0 at the exit of the beam line was expected to be 2.0×10^9 per day based on the GEANT4 simulation. We estimated geometrical acceptance for $K_L^0 \to \pi^+\pi^-\pi^0$ decays with various layouts by the simulation, and decided the cross sections of the hodoscopes and the calorimeter banks to be 40×60 cm^2 and 35×35 cm^2, respectively. In this case, the acceptance was 0.004% [1]. Considering the branching ratio of the $K_L^0 \to \pi^+\pi^-\pi^0$ decay, we could detect 1.0×10^4 $K_L^0 \to \pi^+\pi^-\pi^0$ events per day, and this number was sufficient for this measurement.

Next, we considered a material for the electromagnetic calorimeter. The range of the photon energy was expected from 100 MeV to 800 MeV. The calorimeter should have sufficient energy resolution for the photon with such energies. We decided to use undoped CsI crystals, which were used in the E391a experiment. Undoped CsI has a short radiation length and enough light outputs for photons in the required energy range. Details of the CsI calorimeter is described in Section 4.3.1.

At last, we considered a design of the tracking system; in particular, a requirement on the position resolution of the hodoscopes was examined, since it affected on quality of the reconstruction of kinematic variables and event selection efficiency in the analysis. We checked the resolution of the K_L^0 momentum and the efficiency for signal events, as shown in Fig. 4.2. With hodoscopes that were composed with 10-mm-wide scintillator strips, the position resolution for charged tracks could be expected to be 3 mm. With this position resolution, the expected number of reconstructed K_L^0's per day was 2000 events, and the momentum resolution of the K_L^0 would become 12%. These values were sufficient for this measurement. Details of the scintillator hodoscopes are described in Section 4.3.4.

4.3 Detector

The experimental setup for the $K_L^0 \to \pi^+\pi^-\pi^0$ measurement is shown in Fig. 4.3. It consisted of two major components to detect $K_L^0 \to \pi^+\pi^-\pi^0$ decays that occurred in the upstream region of the setup. One component was an electromagnetic calorimeter with undoped CsI crystals to detect photons from π^0 decays. The other component was a tracking system with sets of hodoscope planes to detect charged particles. In addition, a charged veto system (CV) to detect and veto charged particles was located in front of the calorimeter. As shown in the photo in Fig 4.4, a bag filled with helium gas was inserted in the beam region between the exit window of the beam line and the surface of the calorimeter to reduce backgrounds due to neutron interactions

[1] This values contains the K_L^0 decay probability in the upstream region of the detector, which was 5.6%.

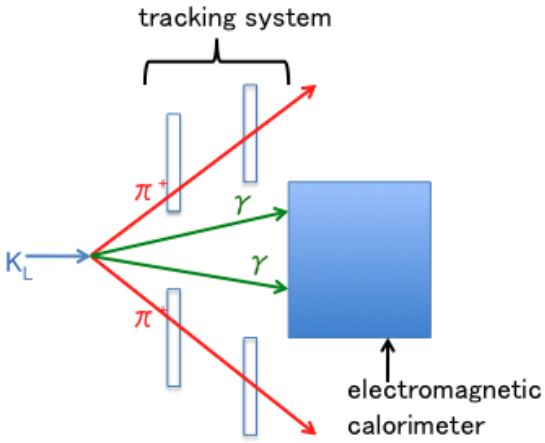

Figure 4.1: Schematic view of a detector system for K_L^0 flux measurement

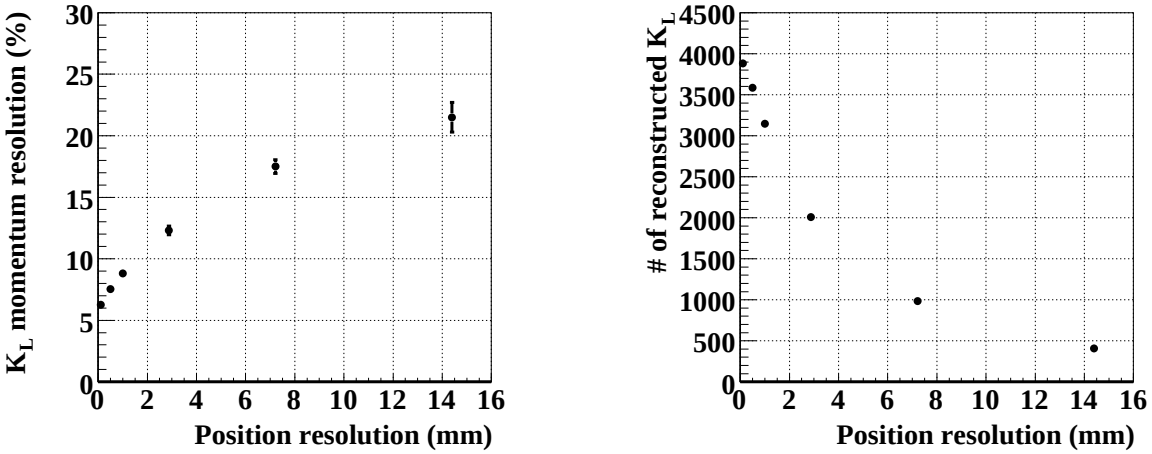

Figure 4.2: Momentum resolution of the K_L^0 (left) and the amount of reconstructed K_L^0 per day (right) as functions of the position resolution of the hodoscope.

in the beam. No detectors were placed in the neutral beam in order to avoid excessively high counting rate.

Here, a coordinate system used in this measurement is defined: x in the horizontal, y in the vertical, and z in the beam directions. The origin of the coordinate is set at the center of the production target. The exit of the beam line is located at $z = 20.6$ m.

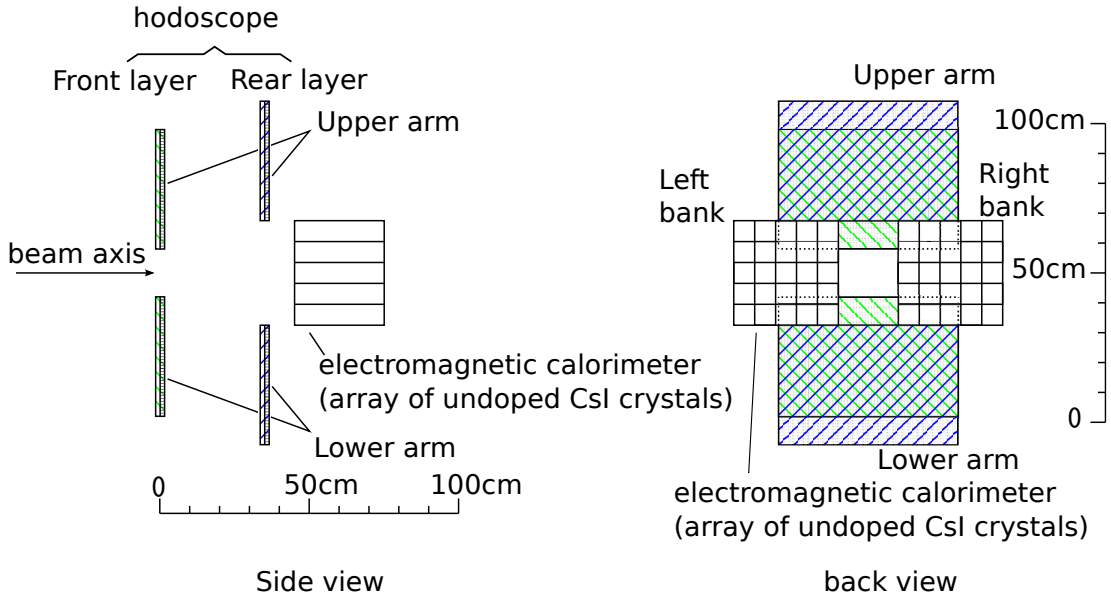

Figure 4.3: Schematic drawing of the experimental setup in the side view (left) and the back view (right)

4.3.1 CsI Calorimeter

The electromagnetic calorimeter was located at $z = 24.1$ m. As shown in Fig. 4.3, there were two calorimeter banks; one was on the left and the other was on the right of the beam line with a 20 cm space between the two. One bank consisted of 25 undoped CsI crystals, stacked in a 5×5 matrix. A photo of the calorimeter is also shown in Fig. 4.5.

CsI Crystal

Figure 4.6 shows a module of the calorimeter. The size of a CsI crystal was 7×7×30 cm^3. Each CsI crystal was wrapped with a 100-μm-thick Teflon sheet and then wrapped with a 20-μm-thick aluminized Mylar sheet in order to isolate each crystal optically and to improve the light collection. The scintillation light produced by the electromagnetic showers in the CsI crystals was detected by the photo-multiplier tubes (PMTs) mounted on the back of each crystal. Each crystal was viewed by a 2-inch PMT (Hamamatsu R4275-02 [29]) through a 3-mm-thick silicone cookie, a UV transmitting filter and a light guide. The UV transmitting filter reduced the slow component of the scintillation light from the CsI crystal. The CsI crystal yielded typically 15 photoelectrons per the energy deposition of 1 MeV. All of the crystals and the PMTs were acquired from the calorimeter used in the E391a experiment [30].

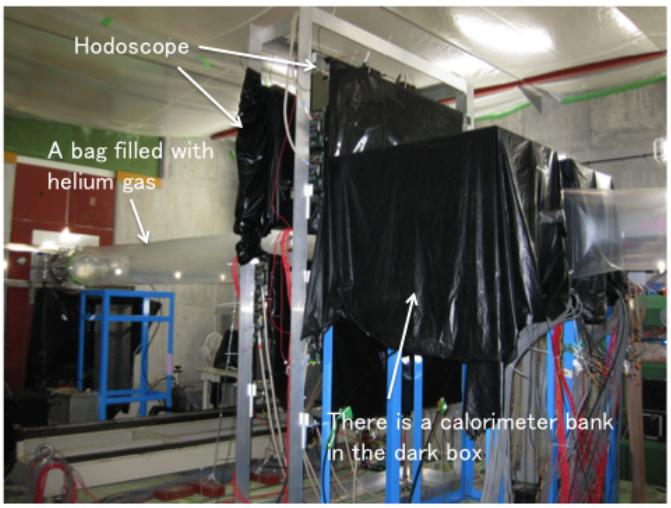

Figure 4.4: Photo of the experimental area. The detector system covered by black sheets for light shielding appears in the center. The neutral beam came from the left side. A bag filled with helium gas was installed upstream in the beam region.

Figure 4.5: Photo of the CsI calorimeter.

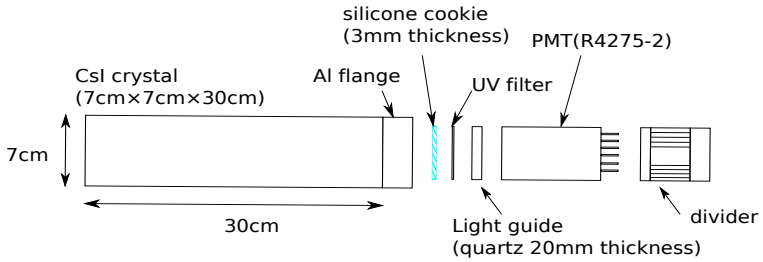

Figure 4.6: Schematic drawing of a calorimeter module.

Humidity and temperature management

An undoped CsI crystal is a deliquescent material. We had to keep its ambient humidity low. Each calorimeter bank was installed in a dry box, where dry air was flowed constantly with the flow rate of approximately 25 cc/min. The box was used also for light shielding. The ambient relative humidity was measured and monitored with a humidity sensor (TDK CHS-UPS [31]) in each box. The sensor gives an output voltage from 0 to 5 V which was linear to the relative humidity corresponding to the range from 0 to 100%. The output voltage from the sensor was measured by a scanning analog-to-digital converter (ADC) every one minute. The scanning ADC (Technoland C-TS 201B [32]) can measure the range of ±5 V with the 12-bit resolution. As shown in Fig. 4.7, the humidity was kept below 14 % during the measurements, which is sufficiently low to prevent the CsI crystal deliquesce.

The light yield of the crystal has a temperature dependence of -0.6 %/°C [22]. Therefore the temperature in the experimental area was kept constant with an air conditioning. The ambient temperature was measured and monitored with a temperature sensor (National Semiconductor LM35DZ/NOPB [33]) in each box. The sensor gives an output voltage from 0 to 5 V which was linear to the temperature corresponding to the range from 0 to 100°C. The output of this sensor was also measured by the scanning ADC. Figure 4.8 shows the temperature during the measurements. The temperature was kept constant within ±1°C, and thus fluctuation of light yields due to the temperature variation was suppressed to about 1% level.

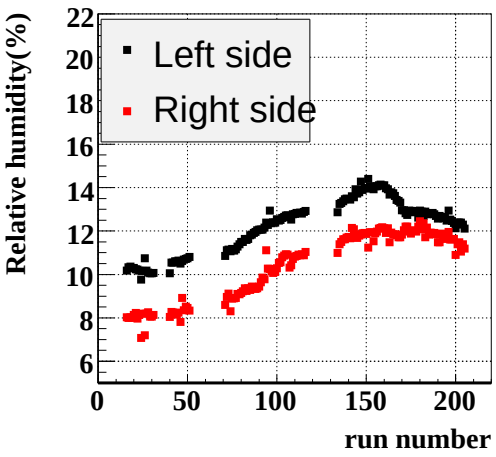

Figure 4.7: The ambient relative humidity of the CsI calorimeter in the dry box containing CsI crystals as a function of the run number in the K_L^0 measurements. Black and red squares show the humidity of the left-side and right-side banks, respectively.

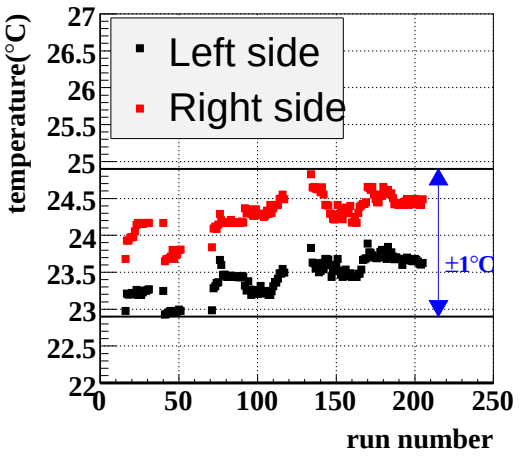

Figure 4.8: The ambient temperature of the CsI calorimeter in the dry box containing CsI crystals as a function of the run number in the K_L^0 measurements. Black and red squares show the temperature of the left-side and right-side banks.

Performance of the Electromagnetic Calorimeter

Prior to the K_L^0 flux measurement, we evaluated the energy resolution of the calorimeter. A part of the calorimeter, a 3×3 array of CsI crystals, was tested by using a positron beam at the Research Center for Electron Photon Science in Tohoku University. The energy range we measured was from 0.2 to 0.8 GeV. Figure 4.9 shows the result of the energy resolution as a function of the incident beam energy (E). We obtained the energy resolution to be:

$$\frac{\sigma_E}{E(GeV)} \simeq \frac{1.5\%}{E(GeV)} \oplus \frac{0.5\%}{\sqrt{E(GeV)}} \tag{4.1}$$

where the symbol $\oplus$ represents summation in quadrature.

We also measured the linearity of the calorimeter, as shown in Fig. 4.10. It was found to be ±3.5% in the energy range from 0.2 GeV to 0.8 GeV.

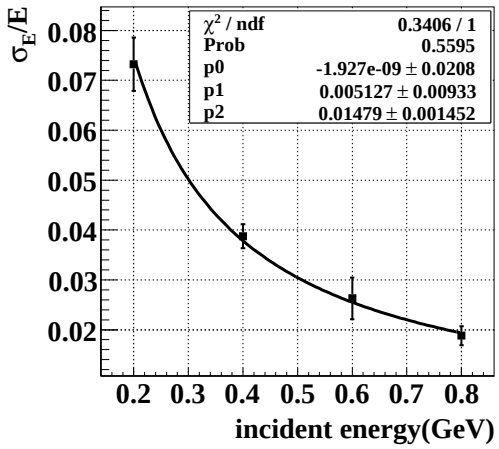

Figure 4.9: Energy resolution of the 3 × 3 CsI crystals as a function of the incident positron energy. A curve indicates the resultant fitting function, which was represented in the form in Eq. 4.1.

4.3.2 Charged veto counter (CV)

The front face of each calorimeter bank was covered with a charged veto counter (CV) to detect and veto charged particles. The CV was made of a 7-mm-thick scintillator plate, and its cross section was 38 × 38 cm^2. The scintillator plate was wrapped with a 50-μm-thick aluminized Mylar sheet in order to improve the light collection. The scintillator plate had thirty eight 1.6-mm-deep grooves at 10-mm intervals, in which wavelength-shifting (WLS) fibers (Kuraray Y11(200)MS [34]) were glued. Figure 4.11 shows the absorption and emission spectra of the WLS fiber. The wavelength of the absorption peak is 430 nm, while the wavelength of the emission peak is 476 nm. The 38 WLS fibers were bound into a bundle, and the light from the fibers was read by a 1-1/8-inch PMT (Hamamatsu H7415).

(a) (b)

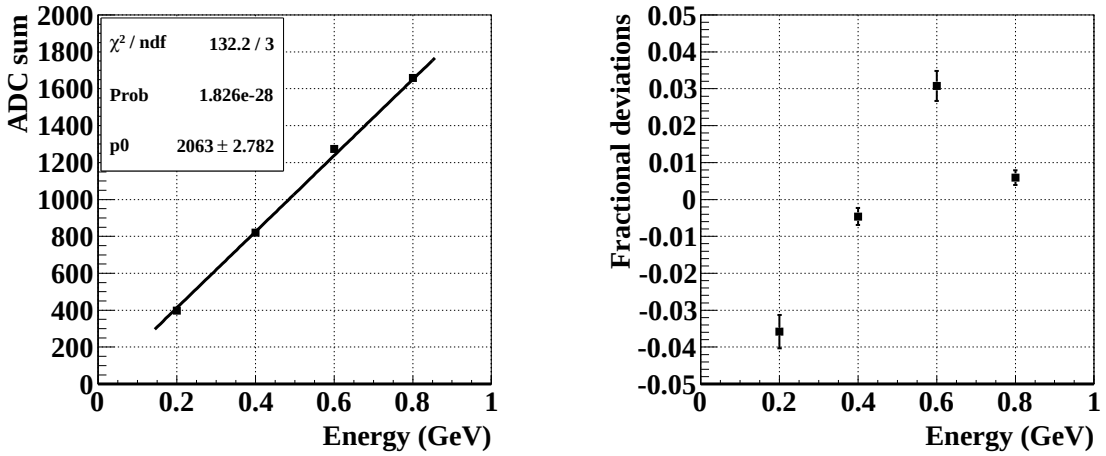

Figure 4.10: (a): Correlation between the incident energy and the sum of output from the 3 × 3 CsI crystals. A straight line fitted to data points. (b): Fractional deviations from the fitting function as a function of the incident energy.

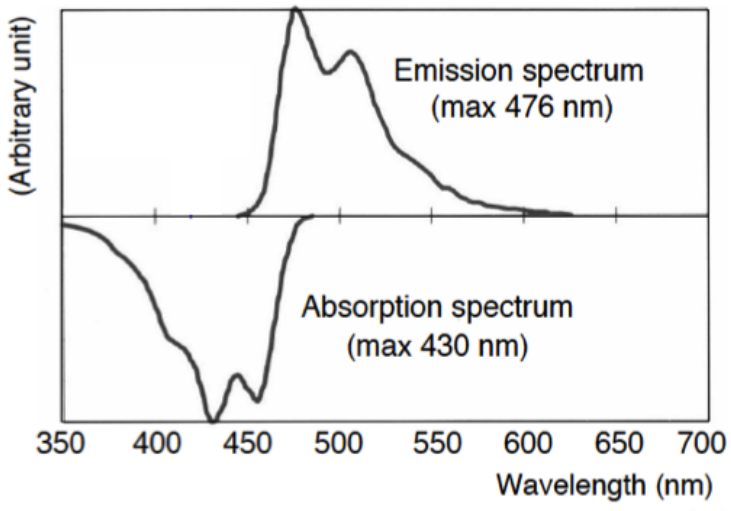

Figure 4.11: Absorption and emission spectra of the wavelength-shifting fiber: Kuraray Y11(200)MS type.

4.3.3 Cosmic-ray counter

In addition to the detectors for measuring $K_L^0 \to \pi^+\pi^-\pi^0$ decays, a counter to catch cosmic rays was also installed. Five plastic scintillator counters were lined up toward the beam direction on the top and the bottom of each calorimeter bank, as shown in Fig. 4.12. The size of the each counter was $5\times1\times35$ cm^3. Each scintillator bar had a 3-mm-diameter hole in the center of the cross section, where a WLS fiber was inserted. The same fiber as in the CV was used. The scintillator was covered with a co-extruded reflective coating, composed of TiO_2 infused in polystyrene. The 10 WLS fibers from counters on the top and the bottom in each bank were viewed by a 16-ch multi-anode PMT (Hamamatsu H6568 MOD).

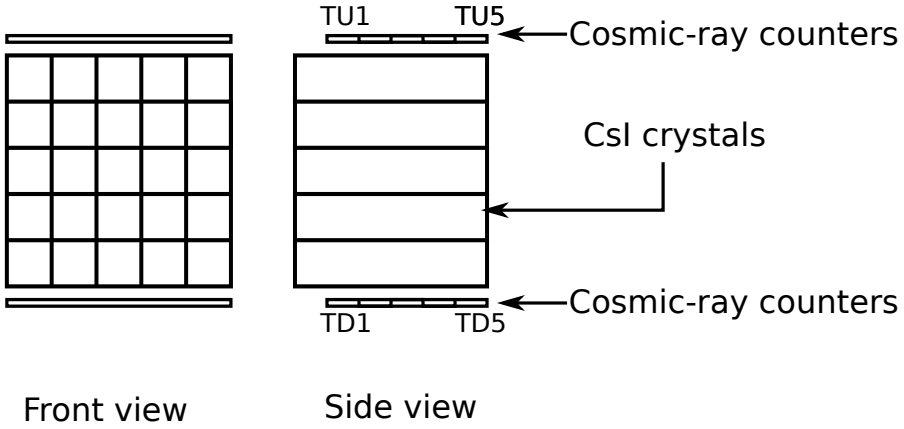

Figure 4.12: Schematic view of the cosmic-ray counters.

4.3.4 Tracking Hodoscope

Charged particles were detected by a set of plastic-scintillator hodoscopes. As shown in Fig. 4.3, they consisted of two identical arms, one above and the other below the beam, which were designated as the upper and lower arms, respectively. Each arm consisted of two hodoscope layers: the front and rear layers separated by 35 cm in the beam direction. The rear layers were located at $z = 24$ m: a distance of 10 cm from the front face of the calorimeter. Each of the hodoscope layers was composed of x and y planes that measure the horizontal and vertical positions, respectively. Each plane was an array of 1-cm-wide and 0.5-cm-thick scintillator strips with wavelength-shifting (WLS) fibers grooved into the strip.

There were 40 scintillator strips in the y plane. The fibers in the y plane were viewed from their both ends by 64-ch multi-anode PMTs (Hamamatsu H8804), as shown in Fig. 4.13. 20 fibers were connected to one PMT on each side, and four PMTs in total were used for readout of a y plane. On the other hand, there were 60 scintillator strips in the x plane. Each fiber in the x plane was viewed by a 64-ch multi-anode PMT from one end: from the top end in the upper arm and the bottom end in the lower arm, respectively. The opposite end was covered with a reflective material to improve light-collection. 30 fibers were connected to one PMT on one end, and two PMTs in total were used for readout of a x plane. Parameters of the tracking hodoscope are listed in Table 4.1.

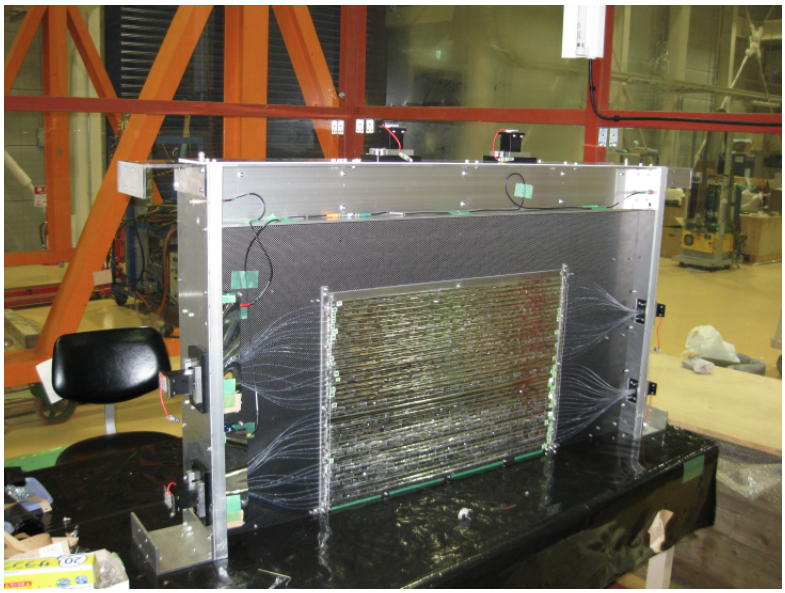

Figure 4.13: Photo of a y-plane hodoscope.

Table 4.1: Structure and dimensions of the tracking hodoscope. There were two identical arms, upper and lower arms, as shown in Fig. 4.1. Labels x and y indicate the planes which measured x and y position, respectively.

Item	Description	Note
Front plane		
z-position	z =23.65 m	from the target
	Δz_{cal} =-44.7 cm	from the calorimeter
transverse coverage	$\|x\| \leq \pm 30$ cm	$60 \times 40\text{cm}^2$ in each arm
	$8 \leq \|y\| \leq 48$ cm	
strip size	1-cm-wide, 0.5-cm-thick	
number of strips	60 (x), 40 (y)	
Rear plane		
z-position	z =24.00 m	from the target
	Δz_{cal} =-10.0 cm	from the calorimeter
transverse coverage	$\|x\| \leq \pm 30$ cm	$60 \times 40\text{cm}^2$ in each arm
	$17.5 \leq \|y\| \leq 57.5$ cm	
strip size	1-cm-wide, 0.5-cm-thick	
number of strips	60 (x), 40 (y)	

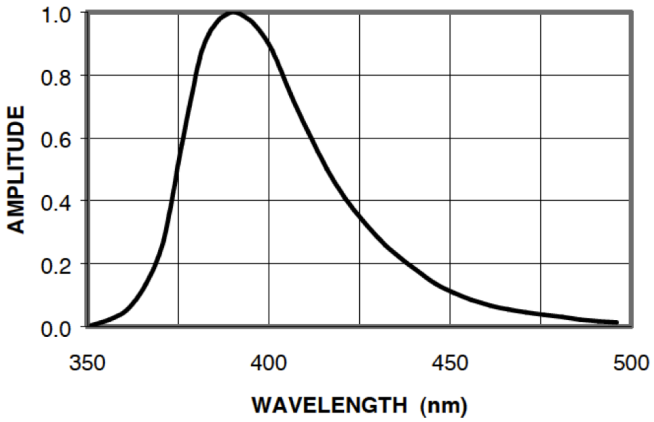

Figure 4.14: Emission spectrum of the EJ230 plastic-scintillator.

Scintillator strip

We used a plastic scintillator provided by ELJEN Technology (EJ-230) [35]. It has a fast response (a short decay time), and emits ultraviolet lights. The characteristics of this scintillator are listed in Table 4.2, and the emission spectrum is shown in Fig. 4.14. The scintillator strip had a 1.5-mm-deep groove to insert a wavelength shifting fiber. Each scintillator strip was wrapped with a 50-μm-thick aluminized Mylar sheet in order to isolate each strip optically and to improve light collection.

Light output	64% anthracene
Scintillation efficiency	9,700 photons/1MeV e^-
Wavelength of maximal emission	391 nm
Rise time	0.5 ns
Decay time	1.5 ns
Refractive index	1.58
Density	1.023 g/cc

Table 4.2: Basic characteristics of the EJ230 plastic-scintillator.

Wavelength-shifting fiber

We used the WLS fiber, Kuraray B2 (200) MS type, glued in the groove of the scintillator strip. The WLS fiber was 1.5 mm in diameter with a multicladding structure. A scintillation light from the EJ-230 scintillator, whose peak wavelength is 391 nm, was absorbed by a WLS material in the fiber, and a light around 420 nm was re-emitted. The emitted light in the fiber was propagated inside a fiber core to a PMT. The quantum efficiency of the photomultiplier with a bialkali photocathode has a peak around 420 nm, and thus the emission from the B2 fiber gave us a benefit of detection with high sensitivity. Figure 4.15 shows the absorption and emission spectra of the B2 fiber.

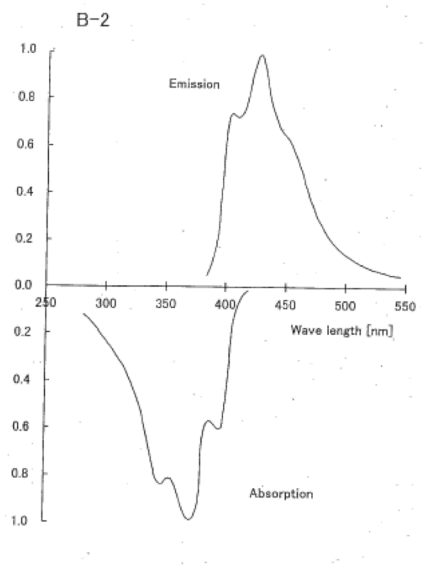

Figure 4.15: Absorption and emission spectra of the B2 fiber.

64-channel multi-anode PMT

The light from the WLS fiber was detected by a 64-channel multi-anode PMT (MAPMT), Hamamatsu H8804. Table 4.3 summarizes its specifications. The H8804 MAPMT has 64 anodes, whose pixel size is 2×2 mm^2, and they are arranged in an 8×8 array. The photocathode area is coated by a bialkali (Sb-K-Cs) material. The quantum efficiency is about 20% at the wavelength of 390 nm.

Model	Hamamatsu H8804
Tube size	30×30 mm^2
Photo-cathode	Bialkali (Sb-K-Cs)
Sensitive wave length	300-650 nm (peak:420 nm)
Quantum efficiency	20% at $\lambda = 390$ nm
Dynode	Metal channel structure, 12 stages
Typical gain	6×10^5 at 800V

Table 4.3: Specifications of the MAPMT used for the tracking hodoscope.

Performance of the tracking hodoscope

The light yield of each strip was measured by using cosmic-ray muons that flew almost horizontally. In this analysis, we required the number of hits in each hodoscope plane to be one, in order to select a single track. The hit position in a x (y) plane was defined as the x (y) position of the center of the strip with a hit. The hit positions in the front and the rear layers were connected, and a cosmic-ray track was reconstructed. We calculated the pass length of the cosmic-ray track in each scintillator strip, and normalized the light yield by the pass length of 5 mm. Figure 4.16 shows the resultant light yields of all the strips in the hodoscope system. The

averaged light yields per 5 mm path length were found to be 20.5 photo-electrons (p.e.) in x planes, and 14.2 p.e in y planes, respectively. In y planes, the yields at both ends were evaluated separately. In x planes, in addition to direct lights, the reflected lights from the opposite ends also contributed the yield, and thus the average value in y planes became larger than that in x planes.

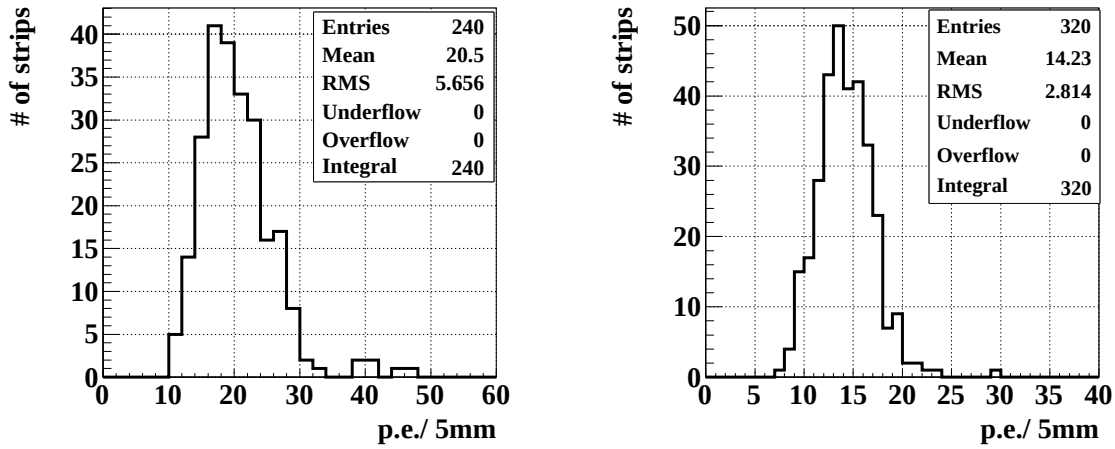

Figure 4.16: Light yields of the scintillator strips read by the H8804 MAPMT in x (left) and y (right) planes. A total of 240 (160) strips in the whole x (y) planes were measured. Note that the yields at both ends were evaluated separately in the y planes.

4.4 Data acquisition

Figure 4.17 shows a schematic diagram of our data acquisition system for the K_L^0 yield measurement. Readout electronics and triggers are explained in order.

4.4.1 Readout electronics

Electronics for the calorimeter

Raw signals from the PMTs in the calorimeter were fed into "amplifier-and-discriminator (A&D)" modules, which were originally developed for the E391a experiment. Each A&D module accepted 8 analog inputs and produced 3 types of outputs: buffered analog signals ($\times 1$ amplified), discriminated logic signals for the individual inputs, and a linear sum of the 8 inputs. The analog signals were sent to CAMAC analog-to-digital converter (ADC) modules: HOSHIN C009H [36], which had 16 input channels, each having the dynamic range of 14 bits. The logic signals were routed to VME multi-hit time-to-digital converter (MHTDC) modules: AMSC AMS-AMT-VME-3A [37], which had 64 input channels, each having the dynamic range of 16 bits with the full scale of 50 μsec. The linear sum signal was used in a trigger logic circuit described later.

Electronics for the tracking hodoscope

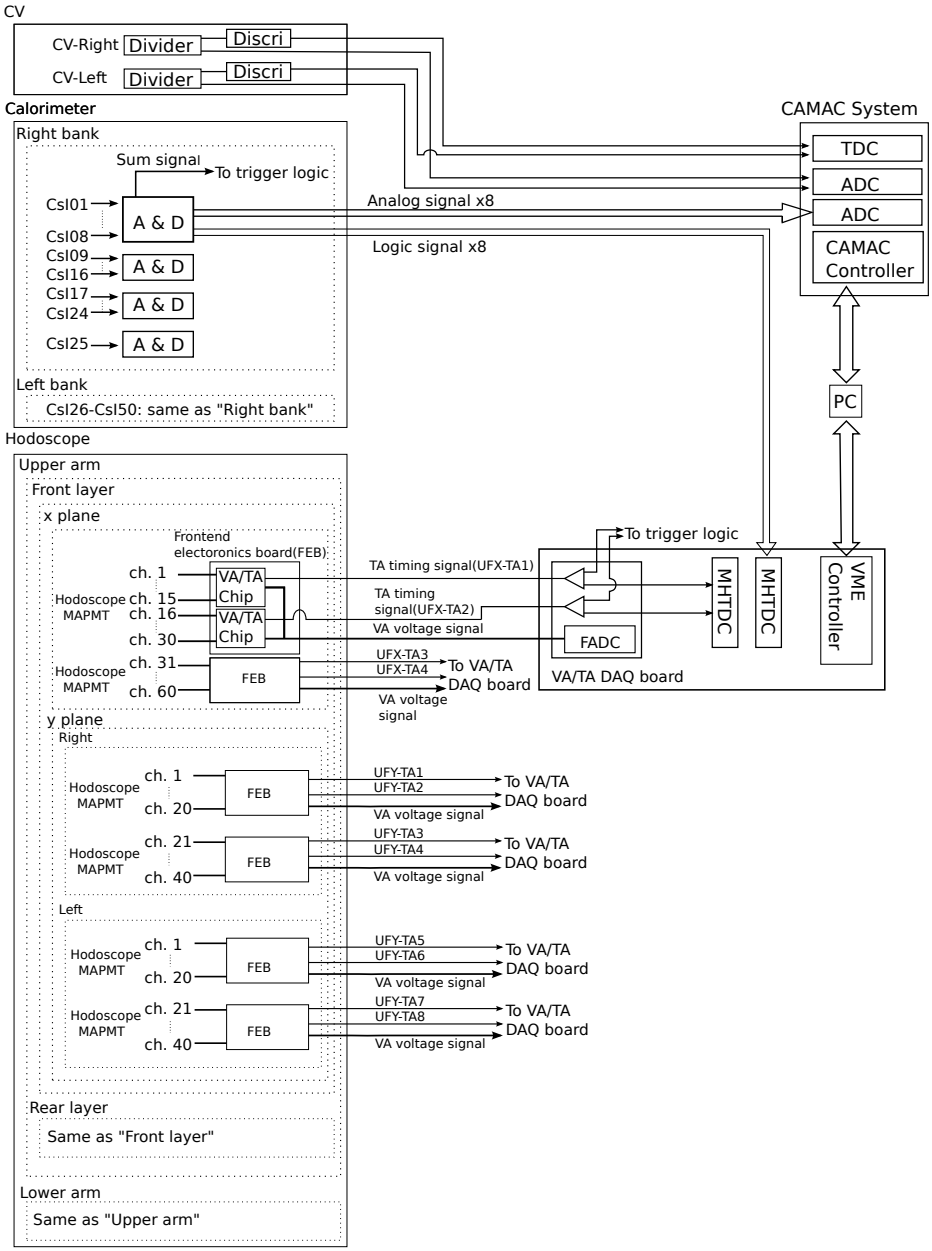

Figure 4.17: Schematic diagram of the data acquisition system.

Raw signals from the hodoscopes were fed into custom readout equipment that incorporated VA/TA chips [38]. Each VA/TA chip accepted 32 analog inputs and produced two types of outputs: a timing signal (TA timing signal), and a serialized voltage signal corresponding to the individual input charges (VA voltage signal). The former output was an OR logic signal of inputs, whose discrimination thresholds were set at voltages equivalent to one photo-electron. The latter output was generated by a parallel-to-serial conversion, which was driven by the request of an external trigger. Both the TA timing and VA voltage signals were sent to custom VME modules called "VA/TA DAQ boards", in which the VA voltage signals were digitized by a 12-bit flash ADC, and the TA timing signal was split into two. Divided two signals were sent to the MHTDC modules and to the trigger logic circuit, respectively. These circuits were originally developed for the long-baseline neutrino experiment at KEK-PS (K2K [39]). Detailed descriptions of the circuits for the hodoscope readout are found elsewhere [40, 41].

4.4.2 Trigger logic circuit

Several types of triggers were formed in this experiment; there were a physics trigger, cosmic-ray triggers, an LED trigger, and a clock trigger.

Physics trigger

Figure 4.18 shows a schematic diagram of the physics trigger circuit. Basically, the physics trigger demanded hits in each calorimeter bank and each hodoscope plane. A hit in the calorimeter bank was defined as an energy deposit more than 20 MeV. More precisely, 25 signals from one calorimeter bank were divided into four groups, and at least one A&D sum signal among the four groups was required to exceed the 20-MeV threshold. On the other hand, a hit in the hodoscope required at least one TA timing signal in a single plane. As mentioned earlier, the threshold for the TA timing signal was set at the one photo-electron level, which was equivalent to the energy deposit of 0.04–0.06 MeV. In the data taking runs, the trigger rate was found to be about 1.2–3.3 Hz, depending on the primary proton intensity. The trigger timing was determined by the coincidence between the two hits from the left and right calorimeter banks. All CAMAC TDCs (VME MHTDCs) were started (stopped) by the physics trigger signal (plus a fixed delay of about 34 μsec).

Other trigger

In addition to the physics trigger, following triggers were prepared.

- Cosmic-ray triggers :
  In order to calibrate the calorimeter and hodoscope gains, we prepared two types of cosmic-ray triggers. For the calorimeter, the trigger was generated by the coincidence signal of cosmic-ray counters located on the top and bottom of the calorimeter. For the hodoscopes, the trigger demanded hits in each hodoscope plane in either of upper or lower arm.

- LED trigger :
  The PMT gain of the calorimeter and the hodoscopes was monitored by LED calibration systems. For the calorimeter, a blue LED was located inside each dry box, and its light was transmitted through an clear fiber to each PMT. For the hodoscopes, a blue LED was located near each multi-anode PMT, and its light was transmitted through WLS fibers to PMT anodes. The LED light was flashed with 1 Hz in the off-spill timing.

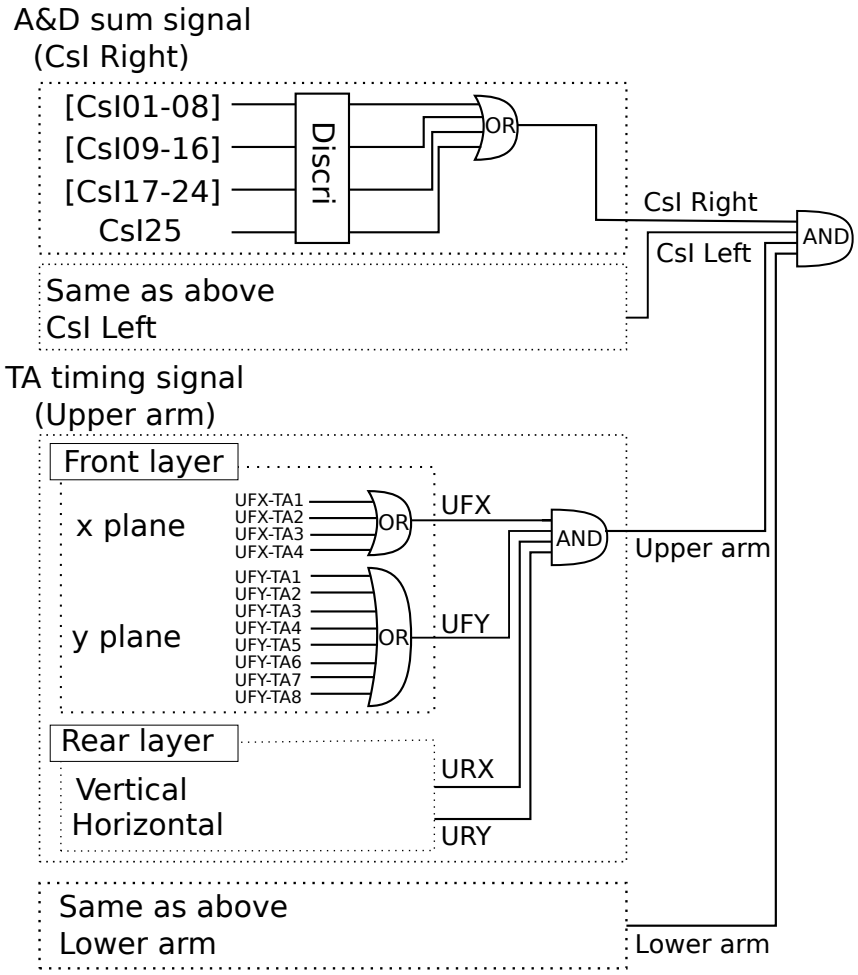

Figure 4.18: Schematic diagram of the physics trigger circuit.

- Clock trigger :
  We took data triggered by a 1 Hz clock in the off-spill timing to monitor the stability of ADC pedestals. The trigger timing is delayed for 500 msec from the LED trigger.

4.5 Calibration

The gains of all detectors were basically calibrated in situ. In this section, methods of energy calibration for the CsI calorimeter and the hodoscope are described.

There were two steps in the energy calibration for the CsI calorimeter. In the first step, the calorimeter module was calibrated by using cosmic-ray tracks. In order to reduce the uncertainty of track length, we selected tracks that passed vertically through the calorimeter, as shown in Fig. 4.19. We required the sum of energy deposits in five crystals in a vertical column of the 5 $\times$ 5 matrix to exceed 10 MeV, and required a pair of top and bottom cosmic-ray counters with the same z position to exceed 0.4 MeV each, respectively. Figure 4.21 shows a resultant ADC distribution of a calorimeter module. The gain factor to convert an ADC value to an energy deposit was calculated by using a simulation for cosmic-ray muons. In the simulation, we used the momentum distribution of cosmic-ray muons shown in Fig. 4.20, which was measured by the BESS experiment at Tsukuba [42]. We assumed the cosmic-ray flux varies as the square of the cosine of the zenith angle. Figure 4.22 shows a distribution of the energy deposits obtained by the simulation, with the same event selection being applied. The peak was fitted to a Landau function. The obtained peak value was 40.7 MeV. Figure 4.23 shows the gain constants for each calorimeter module. We aligned the gain of all modules within $\pm 3.5\%$ by adjusting high voltage values of the PMTs.

In the second step in the calibration for the calorimeter, the gain of each calorimeter module was refined by multiplying an overall factor so that a peak position in the invariant mass distribution of two photons, which is discussed later, became consistent with the nominal π^0 mass.

The hodoscope was calibrated by using cosmic-ray tracks that flew almost horizontally. Tracks used in the calibration were selected by the same way as explained in Section 4.3.4. ADC values were normalized by the pass length in each strip according to the track direction. Figure 4.24 shows the distribution of the normalized ADC value. The gain factor to convert an ADC value to an energy deposit was calculated by using the simulation described in this section.

4.6 Data taking

Data were collected over several days in February 2010, with each run being one- or two-day long. The chronology of the data taking runs is shown in Table 4.4. There were two distinct sets of runs; one used the Ni target and the other used the Pt target. Since the accelerator was being tuned in this period, the beam quality including the power and the instantaneous flux was changed gradually. The data in this thesis corresponds to 2.9×10^{16} protons on the Ni target and 1.5×10^{16} protons on the Pt target. Each run was analyzed separately, and then the runs with the same target were combined.

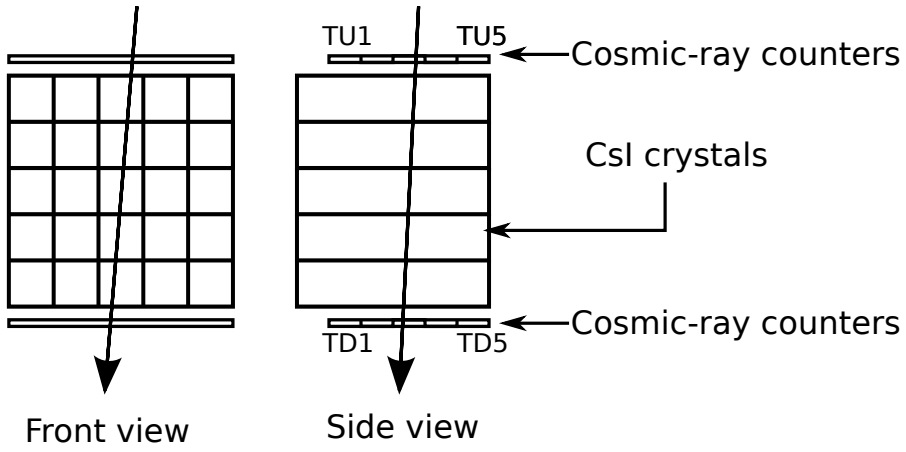

Figure 4.19: Example of a cosmic-ray track used in the energy calibration for the calorimeter. Tracks that passed vertically through the calorimeter were chosen by looking at the hit patterns in the calorimeter array and the cosmic-ray counters.

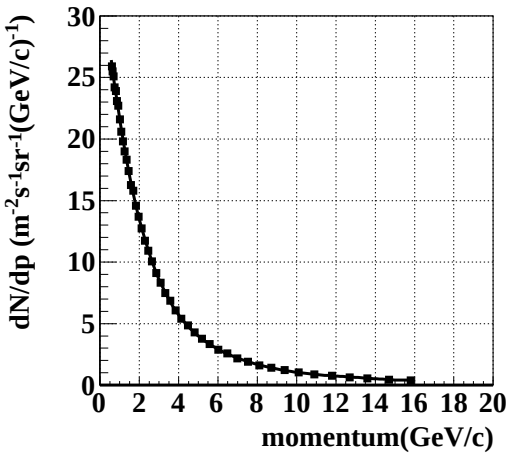

Figure 4.20: Momentum distribution of the cosmic-ray muons which was used in the Monte Carlo simulation.

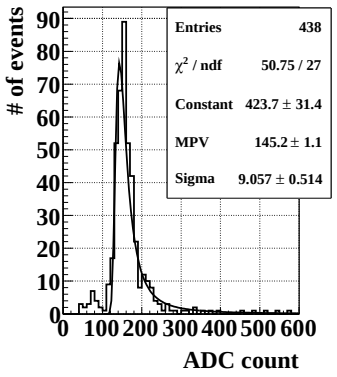

Figure 4.21: ADC data of a calorimeter module for the cosmic-ray tracks used in the calibration. A curve in the figure indicates the fitted Landau function.

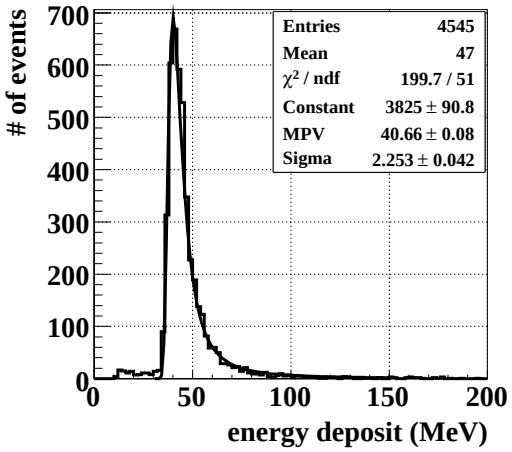

Figure 4.22: Energy deposits of a calorimeter module for the cosmic-ray tracks used in the calibration obtained by the simulation.

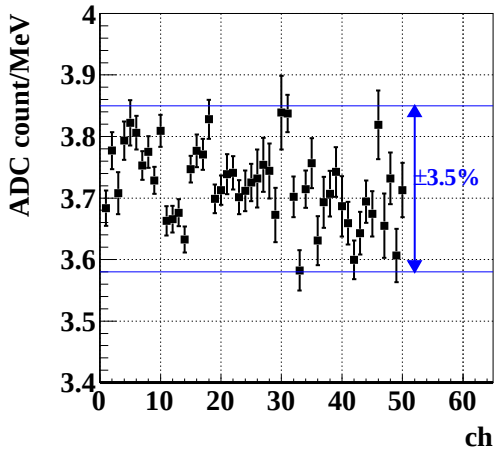

Figure 4.23: Gain constants for each calorimeter module. The horizontal axis indicates module identifiers: 1-25 for modules in the left bank and 26-50 for modules in the right bank.

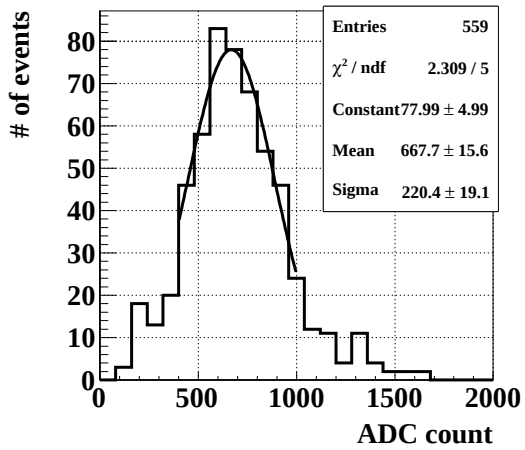

Figure 4.24: ADC data of a scintillator strip for the cosmic-ray tracks, normalized to the 5 mm path length.

Table 4.4: Chronology of data taking runs

Date	Target	Accumulated POT	Number of triggers	MR power
2010/02/17-18	Ni	4.9×10^{15}	1.4×10^{4}	1.0 kW
2010/02/19	Ni	7.9×10^{15}	2.3×10^{4}	1.5 kW
2010/02/19-20	Pt	1.5×10^{16}	9.9×10^{4}	1.0 kW
2010/02/20-22	Ni	1.6×10^{16}	4.5×10^{4}	1.0 kW

Chapter 5

Analysis of the K_L^0 flux measurement

In this chapter, the analysis procedures in the K_L^0 flux measurement are explained. Before discussing the data analysis, the Monte Carlo (MC) simulation for the detector system is described in the first section. Then, the event reconstruction and selection in the data analysis are explained in the next two sections.

5.1 Monte Carlo simulation

The MC simulation was used for three purposes: to estimate the flux of various particles in the neutral beam line, to calculate the acceptance of the signal mode, and to evaluate the contamination of background events.

There were three steps in the simulation processes, as shown in Fig. 5.1. As the first stage of the simulation, a beam line simulation was carried out to estimate fluxes and spectra of the beam particles. We simulated the production of secondary particles in the target and their transportation to the exit of the beam line. In the next step, the simulation process was divided into two streams; one was to simulate K_L^0 decays, and the other was to simulate the hadronic interactions between helium and neutrons in the neutral beam. In the last stage, a detector simulation was carried out to simulate responses of detectors.

5.1.1 Beam line simulation

To estimate the K_L^0, photon, and neutron fluxes in the neutral beam, a beam line simulation was carried out by using the GEANT3 simulation package with the GFLUKA plug-in code for hadronic interactions. The simulation was performed in two steps: particle productions at the target and the transportation to the exit of the beam line. 30-GeV protons were injected into the target, and the generated particles that reached 1 m downstream of the target in 16 degree direction were collected. The interactions of 5.5×10^9 protons on the target were simulated in this step. The obtained outputs were used as input seeds to the transportation step. The azimuthal and polar angles of the momentum vector were smeared by 5% with Gaussian. One seed was recycled two thousand times in order to obtain enough statistics. Note that any effects due to the recycle did not appear in the final results.

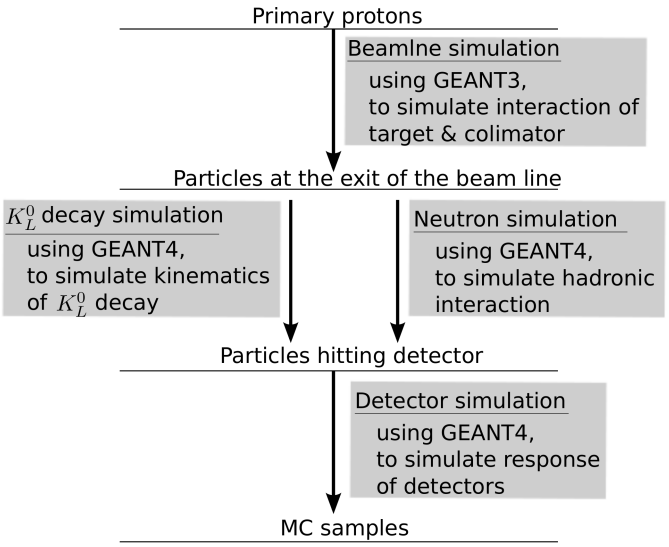

Figure 5.1: Flowchart in the MC simulation.

5.1.2 K_L^0 simulation

We developed a K_L^0 simulation to control the K_L^0 decays. It consisted of a K_L^0 generator and a K_L^0 decay manager.

K_L^0 beam generator

In the simulation, the K_L^0 momentum distribution was expressed by a function that represents an asymmetric Gaussian. For the momentum (p), we used the following function:

$$\frac{dN}{dp} = N_0 exp(-\frac{(p-\mu)^2}{2\sigma^2}) \tag{5.1}$$

$$\sigma = \sigma_0(1-(A+S\times p)(p-\mu)) \tag{5.2}$$

where N_0 denotes an arbitrary normalization factor, and μ, σ_0, A, and S are the mean momentum, the basic dispersion, and the offset and the slope that represent characteristics of the asymmetric shape, respectively. The parameters were determined by fitting the results of the beam line simulation: μ = 1.273, σ_0 = 0.6723, A = -0.4409, and S = 0.02415.

The position and the direction of K_L^0 were determined independently of the beam line simulation. We first set the x and y positions at $z = 0$, so as to be distributed uniformly in the target image: $x = \pm 9.1$ mm and $y = \pm 1$ mm. The direction of K_L^0 was selected uniformly within 10 mrad. We then checked the K_L^0 position at $z = 7$ m, where the size of the beam hole was narrowest, and accepted only K_L^0's within $x = \pm 0.76$ mm and $y = \pm 1.25$ mm. Finally, the position and the direction at the exit of the beam line were calculated. Figure 5.2 shows the momentum distribution of K_L^0's at the beam exit used in the K_L^0 generation. Figure 5.3 shows the position distribution of K_L^0's at the beam exit, which was consistent with that obtained from the beam line simulation.

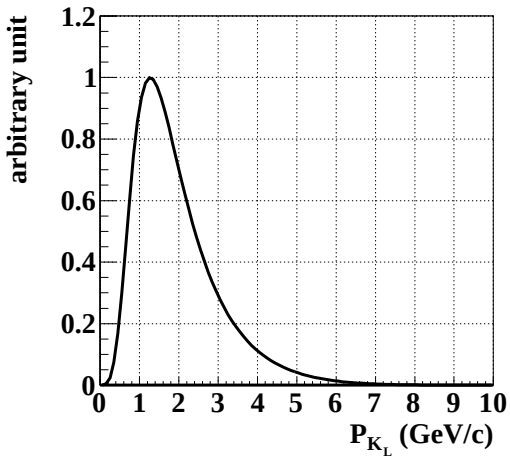

Figure 5.2: K_L^0 momentum distribution expressed by the function in Equation 5.1.

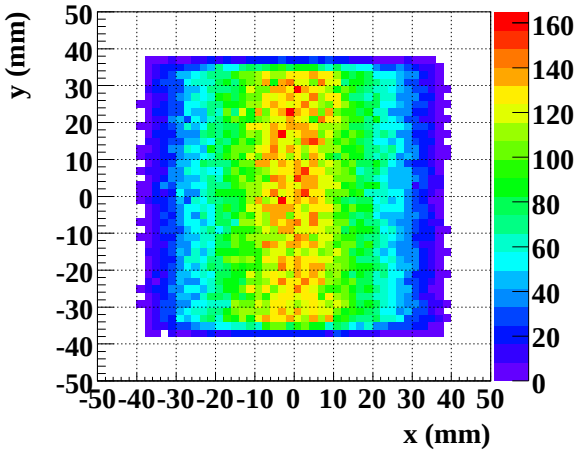

Figure 5.3: K_L^0 position distribution at the exit of the beam line in the Monte Calro simulation.

K_L^0 decay manager

A generated K_L^0 traveled through the detector system until it decayed. The decay position was determined by the life time (τ) and Lorentz-boost factors (β, γ) of the K_L^0. The decay position (z) was determined to obey the exponential curve:

$$f(z) \propto exp(-\frac{z}{\Delta z}) \tag{5.3}$$

$$\Delta z = c\tau\beta\gamma = c\tau \times \frac{p}{m_{K_L^0}} \tag{5.4}$$

where p and $m_{K_L^0}$ are the momentum and the mass of K_L^0, respectively. Then, pre-selected decay process was generated. For $K_L^0 \to \pi^+\pi^-\pi^0$, $K_L^0 \to 3\pi^0$, $K_L^0 \to \pi^\pm e^\mp \nu$, and $K_L^0 \to \pi^\pm \mu^\mp \nu$ decays, kinematics of the secondary particles were calculated on the assumption of V-A interaction with the form factor taken from [22].

5.1.3 Neutron simulation

As shown in Table 3.2, the number of neutrons in the beam was more than one order of magnitude larger than that of K_L^0's. The neutrons interacted with air in the beam region and produced secondary particles. If these particles hit the calorimeter banks and the hodoscope planes, they might become backgrounds. To suppress the interactions, we inserted a bag filled with helium in the beam region from the exit window to the surface of the calorimeter, which reduced the density in the beam region by a factor of seven. In order to estimate the amount of neutron backgrounds, we performed the simulation for hadronic interactions, which was based on the GEANT4 package with the QGSP physics list. As a neutron generator, the outputs from the beam line simulation was directly used, since the statistics of the neutron samples was sufficiently high (2×10^7 neutrons after exit of the beam line).

5.1.4 Detector Response

We simulated the detector response using the GEANT4 package. The interactions with detector materials, such as pair production and multiple scattering, were simulated according to their cross sections implemented in the package.

We summed up energy deposits in sensitive materials in each detector. For the energies in the calorimeter, we added a special treatment to simulate the energy resolution, as described below.

The information of the energy deposit and the timing of each detector were stored with the same format as in the experimental data so that both the real and the simulated data could be analyzed by the identical analysis program.

Energy smearing for the calorimeter

The energy resolution σ_E/E of a calorimeter can be represented as

$$\frac{\sigma_E}{E}(\%) = a \oplus \frac{b}{\sqrt{E}} \oplus \frac{c}{E} \tag{5.5}$$

where $\oplus$ represents addition in quadrature, and E is an energy in the unit of GeV. The constant term a mainly comes from non-uniformity and calibration uncertainty, b is a stochastic term

that represents such as shower fluctuations and photoelectron statistics, and c is a noise term. The c term was estimated to be negligible in our electronics system. A part of the b term that came from shower fluctuations was contained in the energy deposits in the simulation. However, the a term could not be obtained by the interaction in the simulation. We imposed the additional fluctuation, called "smearing", to the energy in each calorimeter module so that the mass resolution of the π^0 expected by the simulation agreed with that obtained from data. The smearing function we used was $\sigma_E/E = 2.5\% \oplus 1.0\%/\sqrt{E}$.

5.2 Event Reconstruction

The flowchart of the event reconstruction in the analysis of $K_L^0 \to \pi^+\pi^-\pi^0$ decays is shown in Fig. 5.4. The reconstruction procedure consisted of four processes: vertex reconstruction, π^0 reconstruction, $\pi^\pm$ reconstruction, and K_L^0 reconstruction. Details of the processes are described in the following subsections.

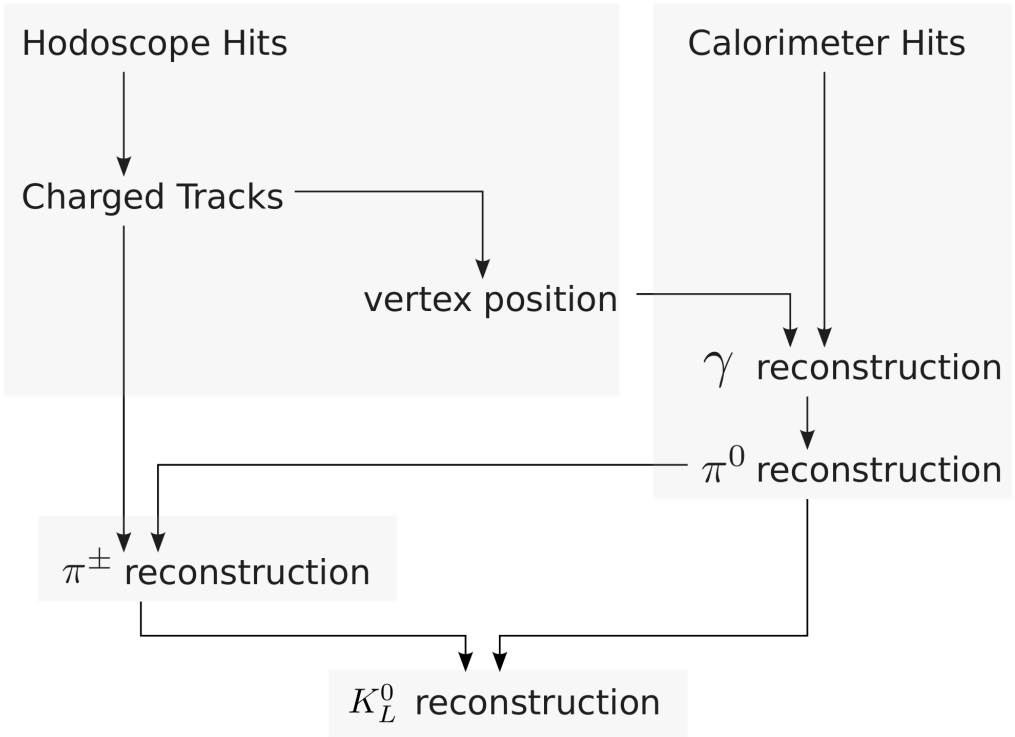

Figure 5.4: Flowchart of the event reconstruction.

5.2.1 Vertex reconstruction

The purpose of the process was to obtain the vertex of two tracks of charged particles, which corresponded to the K_L^0 decay position. To do that, finding hits in the hodoscopes, connecting them as tracks, and calculating their vertex were performed in order.

Hodoscope hits

At first, we searched good hits in each hodoscope plane. A good hit in the hodoscope satisfied the following conditions:

- An energy deposit must be larger than 0.25 times the energy deposited by the passage of a minimum ionizing particle (E_{mip}).
- The hit timing must lie within $\pm$79 nsec of the event timing.

The E_{mip} for the 0.5-cm-thick scintillators was 1 MeV, corresponding to outputs of 21 (14) photoelectrons for the x (y) planes. The event timing was determined by the trigger timing from the coincidence signal of the two calorimeter banks, as stated in Section 4.4.2.

After selecting good hits, the hit positions were calculated. The hit position in each hodoscope plane was defined as the center of the strip with a hit, or the center of the strips if there were multiple hits adjacent to each other.

Charged track reconstruction

The x and y track positions were determined in each layer. If there were more than two hits in a single plane, all x-y combinations were retained for further analysis. The fraction of the events with multiple hits was found to be 29–35%, depending on the beam condition.

Two track positions in the front and rear layers were then connected to obtain a straight line as a track candidate. The candidates were required to be diverging from the beam, expecting good tracks to originate from the upstream beam region.

Vertex reconstruction

With two track candidates from the upper and lower arms, the closest distance between two tracks (d_{min}) were calculated. If there were more than one track candidates in one arm due to multiple hits, the combination with the smallest d_{min} was selected. The vertex position (x_v, y_v, z_v) was then defined as the center of the points on two tracks which gave d_{min}.

5.2.2 π^0 reconstruction

In this process, hits in the calorimeter were analyzed and the energies and positions of photon candidates were obtained. By combining the vertex position reconstructed above, momentum vectors of two photons were obtained, and their invariant mass and total momentum were calculated.

Calorimeter hits

Firstly we defined the energy and the position of a photon that hit a calorimeter bank. The energy was calculated by summing all signals in the bank within the time window of ±79 nsec:

$$E_{\gamma_1} = \sum_{i=1}^{25} e_i,\ E_{\gamma_2} = \sum_{i=26}^{50} e_i \tag{5.6}$$

where E_{γ_1} (E_{γ_2}) is the energy of the photon in the left (right) bank of the calorimeter, and e_i is the energy deposit in the i-th module within the time window.

The position of a photon at the calorimeter surface was defined as the center-of-energy position of all (5×5) energy deposits in a bank:

$$x_{\gamma_1} = \frac{\sum_{i=1}^{25} x_i e_i}{\sum_{i=1}^{25} e_i},\ y_{\gamma_1} = \frac{\sum_{i=1}^{25} y_i e_i}{\sum_{i=1}^{25} e_i}, \tag{5.7}$$

$$x_{\gamma_2} = \frac{\sum_{i=26}^{50} x_i e_i}{\sum_{i=26}^{50} e_i},\ y_{\gamma_2} = \frac{\sum_{i=26}^{50} y_i e_i}{\sum_{i=26}^{50} e_i}, \tag{5.8}$$

where x_{γ_1} and y_{γ_1} (x_{γ_2} and y_{γ_2}) are the positions of the photon in the left (right) bank of the calorimeter, and x_i and y_i are the center positions of each calorimeter module.

Next, we defined a good hit in the calorimeter bank. The following conditions were imposed:

- The total energy in each bank must exceed 50 MeV.
- There must be no hit in the charged veto counter in front of the calorimeter (CV), where a CV hit was defined as a signal larger than $0.4 \times E_{mip}$ within the 500-ns-wide ADC gate.

Both banks were required to satisfy the conditions.

γ reconstruction

The hit position of a photon at the calorimeter was connected to the vertex point in order to obtain the direction of the photon. With information of the total energy in each bank, the momentum vector of each photon was reconstructed.

π^0 reconstruction

The invariant mass of two photons was calculated. A momentum vector of a π^0 candidate was also calculated as a sum of momentum vectors of two photons.

5.2.3 $\pi^\pm$ reconstruction

As the results of the processes so far, the direction of $\pi^\pm$ candidates and the momentum vector of a π^0 candidate were obtained. In order to calculate $\pi^\pm$ momenta next, momentum conservation in the plane perpendicular to the K_L^0 direction was imposed to the transverse momentum balance of the $\pi^+\pi^-\pi^0$ system. Referring to Fig. 5.5, the transverse momentum conservation is represented as

$$p_+ \sin\theta_+ \cos\phi_+ + p_- \sin\theta_- \cos\phi_- + p_{0x} = 0 \tag{5.9}$$
$$p_+ \sin\theta_+ \sin\phi_+ + p_- \sin\theta_- \sin\phi_- + p_{0y} = 0 \tag{5.10}$$

where $p_\pm$, $\theta_\pm$ and $\phi_\pm$ are the absolute momentum, and the polar and azimuthal angles of $\pi^\pm$, respectively, and p_{0x} (p_{0y}) denotes the x (y) component of the π^0 momentum. Here in the analysis, the K_L^0 direction was assumed to be identical to the z direction since the solid angle of the beam was small. In the equations, tracks in the upper and lower arms were designated as π^+ and π^-, respectively. In Eqs. 5.9-5.10, the unknown variables are $p_\pm$, and these are obtained by solving the system of linear equations.

The four vector of the π^+ and π^- were calculated as

$$\begin{bmatrix} E_\pm \\ p_{\pm x} \\ p_{\pm y} \\ p_{\pm z} \end{bmatrix} = \begin{bmatrix} \sqrt{p_\pm^2 + M_{\pi^\pm}^2} \\ p_\pm \sin\theta_\pm \cos\phi_\pm \\ p_\pm \sin\theta_\pm \sin\phi_\pm \\ p_\pm \cos\theta_\pm \end{bmatrix} \tag{5.11}$$

where $E_\pm$ and $M_{\pi^\pm}$ are the energy and the mass of the $\pi^\pm$, and $p_{\pm x}$, $p_{\pm y}$, and $p_{\pm z}$ are the x, y, and z components of the momentum vector of the $\pi^\pm$, respectively.

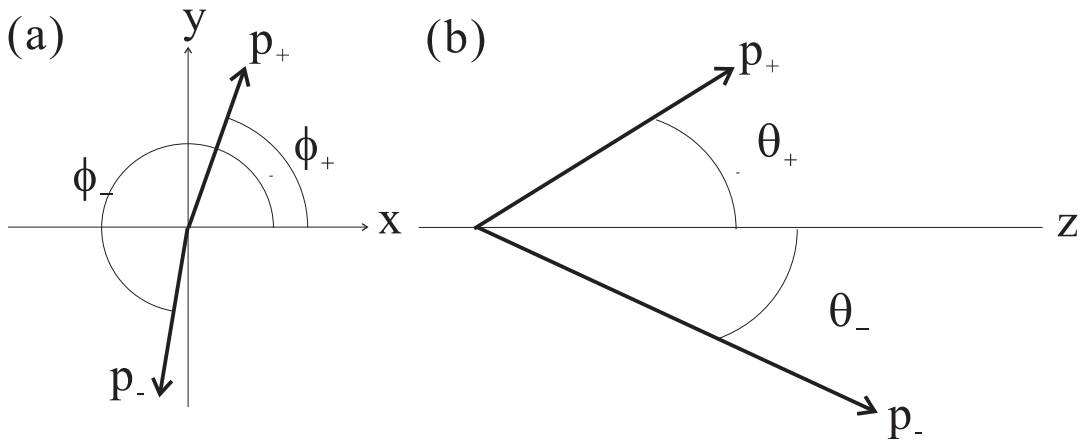

Figure 5.5: Notation of the (a) transverse and (b) longitudinal components of the $\pi^\pm$ momentum vectors.

5.2.4 K_L^0 reconstruction

Here, the invariant mass of π^+, π^-, and π^0 candidates was calculated with the information of their four-momenta. The total energy and momentum were also calculated as the K_L^0 four-momentum.

5.2.5 Primary event selection

In the processes of the event reconstruction, we required conditions on the results in each step. These conditions are summarized below.

- At least two charged tracks must be reconstructed.
- The closest distance between two charged tracks (d_{min}) must be less than 5 cm. Note that if there were more than one combination of track candidates, the combination with the smallest d_{min} was chosen.
- The transverse vertex position (x_v, y_v) should satisfy the condition $|x_v| < 8$ cm and $|y_v| < 8$ cm, which corresponded to the beam size in the experimental setup.
- There must be a good hit in each calorimeter bank without a hit in the CV. The photon energy in each bank must exceed 50 MeV.

These conditions are refered as "primary event selection" in this thesis.

5.3 Event Selection

In this section, the event selection to identify $K_L^0 \to \pi^+\pi^-\pi^0$ decays is described. Note that all the plots in this section were derived for the Ni target. Also note that the resultant K_L^0 flux and spectrum by this study were used as the inputs of the K_L^0 simulation, and results of the neutron simulation were normalized by the accumulated number of protons on the target.

5.3.1 Cut on π^0 invariant mass

In order to select events with a π^0, we required the invariant mass of two photons ($M_{\gamma\gamma}$) to be between 105 and 165 MeV/c^2. Figure 5.6 shows the invariant mass distribution of two photons. Backgrounds from other K_L^0 decays in the low mass region were dominated by $K_L^0 \to \pi^\pm e^\mp \nu$ and $K_L^0 \to \pi^\pm \mu^\mp \nu$ decays with charged pions hitting the support structure of the detector and producing hadronic showers that faked photons in the calorimeter. Small contributions from $K_L^0 \to 3\pi^0$ decays with a π^0 dalitz decay also remained over a broad mass region.

5.3.2 Cut on azimuthal angle

Figure 5.7 shows the distribution of the azimuthal angle between the π^+ and π^-. If the directions of the π^+ and π^- happened to be collinear in the x-y plane, *i.e.* $\phi_- = 180^\circ + \phi_+$, then Eqs. (5.9) and (5.10) are linearly dependent, making them impossible to solve for $p_\pm$. In order to avoid that, we only accepted those events that satisfied

$$|\phi_+ - \phi_-| < 168^\circ \text{ or } |\phi_+ - \phi_-| > 192^\circ. \tag{5.12}$$

5.3.3 Cut on $\pi^\pm$ momentum

Figure 5.8 shows the momentum distributions of the π^+ and π^-. Both p_+ and p_- were required to be in the physical region, *i.e.* positive, as shown in Fig. 5.8.

5.3.4 Cut on vertex position

Figure 5.9 shows the z vertex distribution. In order to ensure that the decay occurred between the exit window of the beam line ($z = 20.6$ m) and the front hodoscope ($z = 23.65$ m), we required z_v to be in the range of $21.0 < z_v < 23.5$ m ($-3.1 < \Delta z_v < -0.6$ m from the front surface of the calorimeter).

5.3.5 Cut on two photon distance

We required the distance between two photons in the calorimeter to be larger than 40 cm. This cut was introduced in order to reject events where both two photons hit the insides of the calorimeter banks.

5.3.6 Cut on K_L^0 invariant mass

Figure 5.10 shows the invariant mass of $\pi^+\pi^0\pi^0$ ($M_{\pi^+\pi^-\pi^0}$), where a clear K_L^0 peak is observed with negligible background contamination. We identified those events that satisfied $460 < M_{\pi^+\pi^-\pi^0} < 540$ MeV/c^2 as K_L^0.

5.3.7 Summary of the event selection

Table 5.1 shows the numbers of remaining events after various kinematical cuts. After imposing all the cuts, the observed number of K_L^0 decays was 1923 for the Ni target. For the Pt target runs, the same analysis procedure was taken, and 2217 events passed all the cuts.

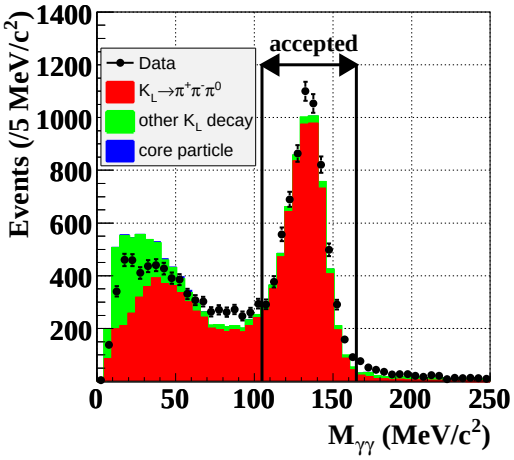

Figure 5.6: Invariant mass distribution of two photons after the primary event selection described in Section 5.2.5. Dots with bars indicate the data. Histograms show the simulation results of $K_L^0 \to \pi^+\pi^-\pi^0$ signals (red), backgrounds from K_L^0 decays (green), and backgrounds due to interactions in the beam core (blue), respectively. Events between the two lines were accepted as π^0-inclusive events. The backgrounds due to beam interactions (blue) were found to be negligible (and their contributions are difficult to find in the plot).

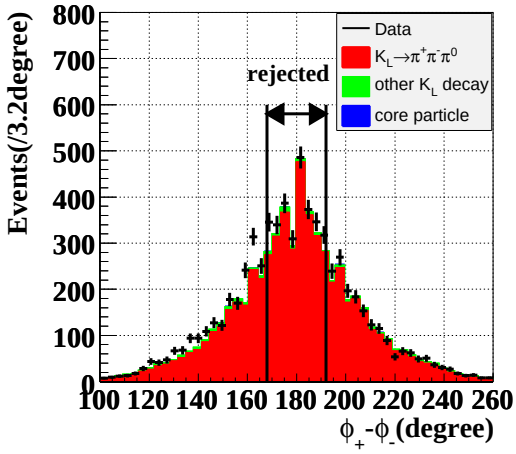

Figure 5.7: Distribution of the azimuthal angle between the π^+ and π^- after the kinematical cuts on $M_{\gamma\gamma}$. Events of the range between the two lines were rejected. Dots with bars indicate the data. Histograms show the simulation results of $K_L^0 \to \pi^+\pi^-\pi^0$ signals (red), backgrounds from K_L^0 decays (green), and backgrounds due to interactions in the beam core (blue), respectively. The backgrounds due to beam interactions (blue) were found to be negligible.

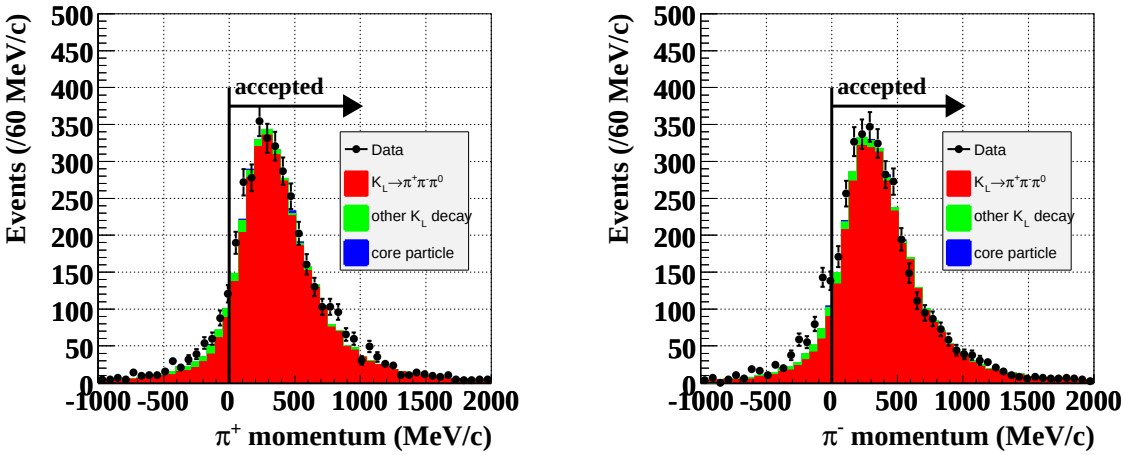

Figure 5.8: Momentum distributions of the π^+ (left) and π^- (right) after the kinematical cuts on $M_{\gamma\gamma}$ and $\phi_\pm$. Here the charge "+" ("-") indicates the track passed through the upper (lower) arm of the hodoscope. Events above the line were accepted. Dots with bars indicate the data. Histograms show the simulation results of $K_L^0 \to \pi^+\pi^-\pi^0$ signals (red), backgrounds from K_L^0 decays (green), and backgrounds due to interactions in the beam core (blue), respectively. The backgrounds due to beam interactions (blue) were found to be negligible.

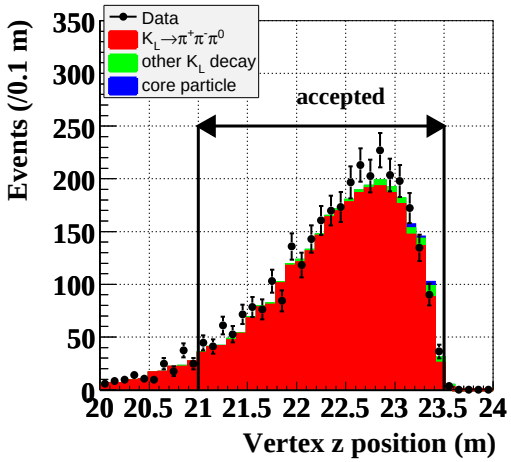

Figure 5.9: Vertex distribution after the kinematical cuts on $M_{\gamma\gamma}$, $\phi_{\pm}$, and $p_{\pm}$. The range between two lines indicates the fiducial region. Dots with bars indicate the data. Histograms show the simulation results of $K_L^0 \to \pi^+\pi^-\pi^0$ signals (red), backgrounds from K_L^0 decays (green), and backgrounds due to interactions in the beam core (blue), respectively. The backgrounds due to beam interactions (blue) were found to be negligible.

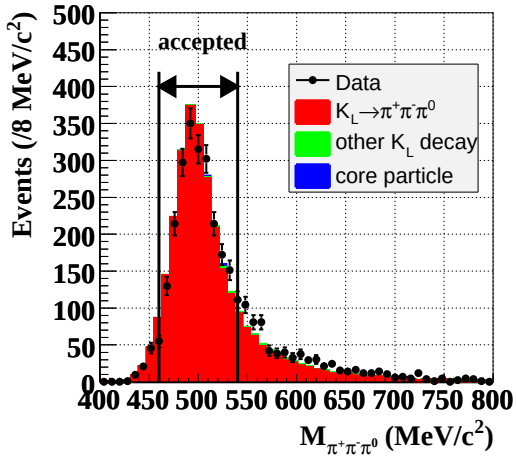

Figure 5.10: Invariant mass distribution of $\pi^+\pi^-\pi^0$ after imposing all the kinematical cuts except the cut on $M_{\pi^+\pi^-\pi^0}$. Events between the two lines were identified as $K_L^0 \to \pi^+\pi^-\pi^0$ decays. Dots with bars indicate the data. Histograms show the simulation results of $K_L^0 \to \pi^+\pi^-\pi^0$ signals (red), backgrounds from K_L^0 decays (green), and backgrounds due to interactions in the beam core (blue), respectively. The backgrounds were found to be negligible.

Table 5.1: Summary of the kinematical cuts. Here the results in the Ni target runs are shown. Reduction here is defined by normalizing to the number of events after the primary event selection.

Cut name	Cut values	Events remained	Reduction
Primary event selection		12059	-
π^0 invariant mass ($M_{\gamma\gamma}$)	$105 < M_{\gamma\gamma} < 165$ MeV/c^2	5801	48%
Azimuthal angle ($\phi_\pm$)	$\lvert\phi_+ - \phi_-\rvert < 168^\circ$ or $\lvert\phi_+ - \phi_-\rvert > 192^\circ$	3465	29%
$\pi_\pm$ momentum ($p_\pm$)	$p_\pm > 0$	2871	24%
Vertex position (z_v)	$21.0 < z_v < 23.5$ m	2722	23%
2γ distance ($d_{2\gamma}$)	$d_{2\gamma} > 40$ cm	2666	22%
K^0_L invariant mass ($M_{\pi^+\pi^-\pi^0}$)	$460 < M_{\pi^+\pi^-\pi^0} < 540$ MeV/c^2	1923	16%

Chapter 6

Results of the K_L^0 flux measurement

In this chapter, the results of the K_L^0 flux measurement are discussed. In the first section, the calculation method of the K_L^0 flux at the exit of the beam line from the observed data is described. In the second section, the method to obtain the K_L^0 momentum spectrum at the exit of the beam line is described. In the last section, the systematic uncertainties of the K_L^0 flux measurement are described.

6.1 K_L^0 flux

In order to determine the K_L^0 flux, it was necessary to apply several corrections to the event sample that remained after imposing all the event selections described in the previous chapter.

The first step was to apply correction factors for the DAQ live time and the detection efficiency of the hodoscope.

Once this was done, the remaining events could be classified into three categories: the $K_L^0 \to \pi^+\pi^-\pi^0$ signal events, background events originated from K_L^0 decays, and background events due to neutron interactions in the beam. The second step was to subtract these backgrounds. For the neutron background, we estimated their contribution by the neutron simulation, and then the number of neutron backgrounds was subtracted from the number of remaining events. After this subtraction, all the remaining events could be regarded as the events originated from K_L^0 decays including both signals and backgrounds. In order to estimate the number of signal events, we calculated the expected fraction of $K_L^0 \to \pi^+\pi^-\pi^0$ signals in the remaining sample by the K_L^0 simulation. Summarizing the discussion above, the number of signal events (N_{signal}) could be written as

$$N_{signal} = \left(\frac{N^{data}}{\epsilon_{DAQ} \cdot \epsilon_{hodoscope}} - N_{core}^{MC}\right) \times R_{signal} \tag{6.1}$$

where N^{data} denotes the number of remaining events after imposing all the event selections, ϵ_{DAQ} the correction factor of the DAQ live time, $\epsilon_{hodoscope}$ the detection efficiency of the hodoscope, N_{core}^{MC} the number of neutron background events obtained by the simulation, and R_{signal} the fraction of the $K_L^0 \to \pi^+\pi^-\pi^0$ signals among the contributions from all the K_L^0 decays.

As the final step, we divided the number of signal events by the product of the acceptance and the branching ratio of the signal mode. This gave the number of K_L^0's at the beam exit. The K_L^0 flux was normalized to 2×10^{14} protons on the production target (POT), which corresponds

Table 6.1: DAQ live time for each period

Date	Target	Intensity	N^{data}	The DAQ live time
2010/02/17-18	Ni	1.0 kW	348	98%
2010/02/19	Ni	1.5 kW	516	96.8%
2010/02/19-20	Pt	1.0 kW	2217	95.6%
2010/02/20-22	Ni	1.0 kW	1059	98.2%

to the design value of POT per single spill from the J-PARC MR accelerator with the slow extraction. In summary, the K_L^0 flux was defined as:

$$(K_L^0\ flux) = \frac{N_{signal}}{Br \times A_{signal} \times N^{POT}} \times 2 \times 10^{14} \tag{6.2}$$

where Br denotes the branching ratio of the signal mode, A_{signal} the acceptance of the signal mode, and N^{POT} the number of accumulated POT during the data-taking period.

The calculations in each step are described below in more detail.

6.1.1 Correction of the DAQ live time

While taking data, we recorded the number of physics trigger requests and the number of events that were actually processed. We defined a DAQ live time as

$$\text{DAQ live time} = \frac{\text{The number of processed events}}{\text{The number of physics-trigger requests}} \tag{6.3}$$

Table 7.1 shows the DAQ live time for each period of data-taking runs. The correction factor for the Ni target runs was 97.7 % in average, and was 95.6 % for the Pt target run.

6.1.2 Detection efficiency of the hodoscope

To evaluate the detection efficiency of the hodoscope, we took data with special trigger conditions; when the efficiency of x planes was being measured, the trigger required hits in only y planes, and vice versa. As an example, the case when we determined the efficiency of the front x-plane in the upper arm is explained here. In this case, using data with the y-plane trigger, we selected the events with one and only one good hit in all the three planes in the upper arm other than the target plane: the front x-plane in this example. The definition of a good hit was the same as that given in Section 5.2.1, namely an energy deposit of more than 0.25 MeV within the timing window of ±79 nsec. We called the resultant events as a "good-track" sample for the front x-plane in the upper arm. We then examined whether or not the front x-plane itself had a good hit. The detection efficiency was defined as,

$$\epsilon_{hodoscope(upper-front-x)} = \frac{N\left(\begin{array}{l}\text{the events with a good hit(s)}\\ \text{in the upper front } x\text{-plane}\end{array}\right)}{N(\text{all events in the "good-track" sample})} \tag{6.4}$$

Figure 7.1 shows the distribution of the maximum energy deposit in a strip in the target plane (the front x-plane in the upper arm). Table 7.2 shows a summary of the efficiencies of the hodoscope planes. Since hits in all the eight planes were required in the $K_L^0 \to \pi^+\pi^-\pi^0$ analysis, the combined detection efficiency ($\epsilon_{hodoscope}$) must be calculated as a products of all efficiencies, and was found to be 87.4±0.2%.

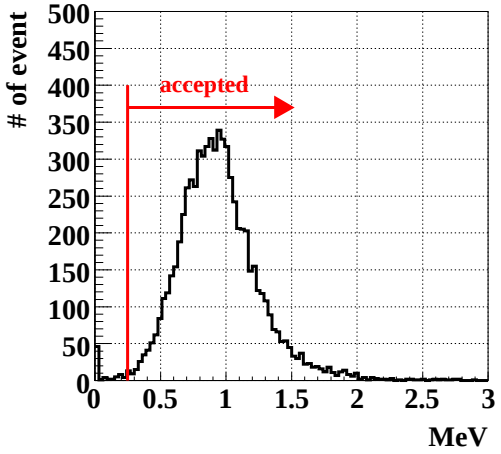

Figure 6.1: Distribution of the maximum energy deposit in a strip in the evaluation of the hodoscope efficiency. Here, the result in the upper front x-plane is shown as an example, with the "good track" sample explained in the text. The red line in this figure shows the threshold value of 0.25 MeV for a good hit.

	Upper arm			
	Front layer		Rear layer	
	Vertical	Horizontal	vertical	horizontal
efficiency	98.9±0.07%	98.8±0.06%	98.5±0.08%	97.4±0.09%

	Lower arm			
	Front layer		Rear layer	
	Vertical	Horizontal	vertical	horizontal
efficiency	99.2±0.06%	98.8±0.06%	99.0±0.07%	97.8±0.09%

Table 6.2: Summary of the hodoscope efficiency for each plane.

6.1.3 Number of backgrounds due to neutron interactions

We estimated the number of neutron backgrounds by the neutron simulation, assuming that the core neutron flux was correctly reproduced by the simulation based on the GEANT3 package.

The estimated numbers of backgrounds (N_{core}^{MC}) were found to be 6.0 for the Ni target and 15.4 for the Pt target, respectively. The percentage contamination to the signal is 0.3% for the Ni and 0.6% for the Pt targets, respectively.

6.1.4 Acceptance for each K_L^0 decay mode

We estimated the acceptance for K_L^0 decay modes with the K_L^0 simulations. The acceptance was calculated as:

$$A_{mode} = \frac{N_{mode}^{remain}}{N_{mode}^{gen}} \tag{6.5}$$

where N_{mode}^{remain} is the number of remaining events in the simulation after imposing all the event selections, and N_{mode}^{gen} the number of generated K_L^0's. Table 7.3 shows a summary of acceptances for four major K_L^0 decays. We note that the neutral mode, $K_L^0 \to 3\pi^0$, could satisfy the physics trigger condition when it was followed by a π^0 Dalitz decay. As shown in Table 7.3, the acceptance of the signal mode was larger than these of other decay modes by more than two order of magnitudes.

In order to obtain the fraction of $K_L^0 \to \pi^+\pi^-\pi^0$ decays in all the contributions from K_L^0 decay modes, the product of the acceptance and the branching ratio of each mode were calculated, also summarized in Table 7.3. The fraction of the signal mode was calculated as:

$$R_{signal} = \frac{(\text{Br} \times A_{mode})_{K_L^0 \to \pi^+\pi^-\pi^0}}{(\text{sum of } (\text{Br} \times A_{mode}) \text{ over all the } K_L^0 \text{ decay modes})} \tag{6.6}$$

R_{signal} was found to be 99.4%. Among the background modes, the $K_L^0 \to 3\pi^0$ decay had the largest acceptance, but even its contamination to the signal mode was less than 1% after imposing all the cuts.

The acceptance for the $K_L^0 \to \pi^+\pi^-\pi^0$ decay (A_{signal}) was calculated to be 6.4×10^{-6}. The signal acceptance may conveniently be divided into three factors: the decay probability, geometrical acceptance, and analysis efficiencies. These factors were evaluated by the MC simulations, and were found to be 5.6%, 0.079%, and 14.4%, respectively. Figure 7.2 shows the signal acceptance as a function of the K_L^0 momentum. The region with high acceptance was from 1 to 2 GeV/c. Compared with this region, the signal acceptances in the momentum regions of less than 0.5 GeV/c and more than 3.5 GeV/c were smaller by one order of magnitude.

decay mode	Br	A_{mode}	Br$\times A_{mode}$
$K_L^0 \to \pi^+\pi^-\pi^0$	12.56%	$(6.40 \pm 0.05) \times 10^{-6}$	$(8.04 \pm 0.06) \times 10^{-7}$
$K_L^0 \to 3\pi^0$	19.56%	$(1.94 \pm 0.31) \times 10^{-8}$	$(3.79 \pm 0.62) \times 10^{-9}$
$K_L^0 \to \pi^\pm e^\mp \nu$	40.53%	$(8.33 \pm 8.33) \times 10^{-10}$	$(3.37 \pm 3.37) \times 10^{-10}$
$K_L^0 \to \pi^\pm \mu^\mp \nu$	27.02%	$(3.75 \pm 2.17) \times 10^{-9}$	$(1.01 \pm 0.59) \times 10^{-9}$

Table 6.3: Summary of the acceptance for each K_L^0 decay mode.

6.1.5 Normalization of protons on the target (POT)

Information from a secondary emission chamber (SEC) in the proton extraction line of the MR was used to monitor the POT value in each spill. The SEC provided a scaler count proportional

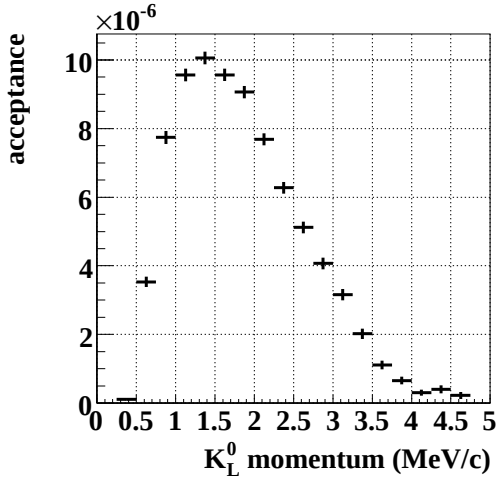

Figure 6.2: Signal acceptance as a function of K_L^0 momentum.

to the proton intensity. The proportionality constant, denoted by G_{SEC}, was determined by comparing the SEC count with the measured intensity by a current transformer (CT) in the MR, provided by the accelerator group. Figure 7.3 shows an example of the G_{SEC} calibration data. The beam loss at the slow extraction was monitored continuously by beam loss monitors, and was 1.4% during the data taking period. Taking the beam loss into account, the number of POT (N^{POT}) was calculated by:

$$N^{POT} = G_{SEC} \times N^{SEC} \times (1 - \delta) \tag{6.7}$$

where N^{SEC} is the total SEC counts during the runs, G_{SEC} an average gain factor obtained by the calibration data , and δ is the beam loss at the extraction, respectively. Table 7.4 summarizes the accumulated numbers of POT in the runs for the Ni and the Pt targets, as well as the gain factors, SEC counts, and beam losses.

Target	G_{SEC}	N^{SEC}	Beam loss	N^{POT}
Ni Target	2.30×10^9	1.26×10^7	1.4 %	2.86×10^{16}
Pt Target	2.30×10^9	6.79×10^6	1.4 %	1.54×10^{16}

Table 6.4: Summary of the accumulated number of POT in the runs for the Ni and the Pt targets. The parameters used in the calculation were also listed.

6.1.6 Calculation of the K_L^0 flux

Table 7.5 summarizes the parameters for the flux calculation, obtained in subsections above. By substituting these values into Eqs. 7.1 and 7.2, the K_L^0 fluxes for the Ni and the Pt targets were obtained as listed in Table 7.6. Expectations by MC simulations are also summarized in the table.

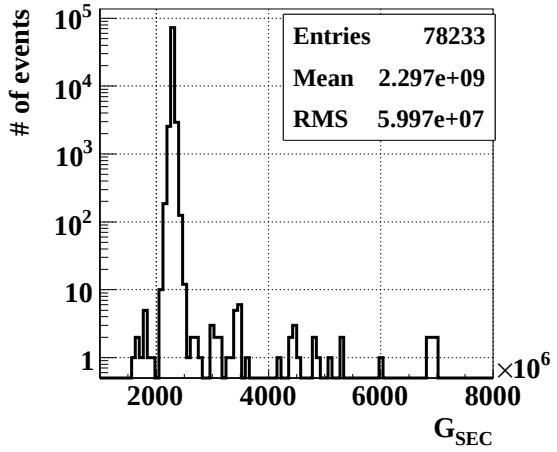

Figure 6.3: Example of the gain factor calibration data; the gain factor was calculated as a ratio of the measured intensity by the CT to the SEC counts in each spill. The fluctuation represented by the root-mean-square in the distribution was found to be a few percent.

The resultant K_L^0 flux for the Ni target was consistent with the expectations from GEANT3 and FLUKA but larger than that from GEANT4. For the Pt target, the measured value was larger than all the expectations by three simulation packages. Note that the differences among various MC simulations included the effects of scattering from the 7-cm-thick lead absorber, as well as the K_L^0 production cross-section. We also examined the ratio of the K_L^0 yield of the Pt target to that of the Ni target. The measurements gave the value of $2.16^{+0.38}_{-0.36}$, while the expectations were 2.05 by GEANT4, 1.58 by GEANT3, and 1.56 by FLUKA, respectively. Concerning the nuclear interaction length (λ_I), the 6.0-cm-long Pt and 5.4-cm-long Ni targets correspond to 0.66 and 0.36 λ_I, respectively. Thus, the ratio of the interaction probabilities in those targets are calculated to be $(1 - e^{-0.66})/(1 - e^{-0.36}) = 1.6$, which is consistent with the GEANT3 and FLUKA results. The measured data showed different dependence on mass numbers in the K_L^0 production from that used in the calculations of interaction lengths, as expected from inclusive hadron production [44].

6.2 K_L^0 momentum spectrum

Figure 7.4 shows the reconstructed K_L^0 momentum distributions for the Ni and the Pt targets, together with the expected spectra by the K_L^0 simulation. The distributions included the detector acceptance and analysis efficiencies, as well as the decay probability in the fiducial region. The original simulation mostly reproduced the spectrum in each plot, but there was discrepancy around a peak. Here, the K_L^0 generators that incorporated the K_L^0 spectra obtained by the GEANT3-based beam line simulation were used in the simulation, as explained in Section 5.1.2. Naively thinking, we just had to make corrections to the original spectrum in the simulation as a function of the K_L^0 momentum. However, the reconstructed momentum was not the true momentum since it contained measurement errors, and the errors also had a momentum dependence. Thus iterative procedures were needed to obtain the true momentum spectrum.

Table 6.5: Summary resultant values of parameters that were used in the calculation of the K_L^0 flux.

Target	Ni target	Pt target
N^{data}	1923	2217
ϵ_{DAQ}	97.7 %	95.6 %
$\epsilon_{hodoscope}$	87.4 %	87.4 %
N_{core}^{MC}	5.98	15.4
R_{signal}	99.4 %	99.4 %
A_{signal}	6.40×10^{-6}	6.47×10^{-6}
N_{POT}	2.86×10^{16}	1.54×10^{16}

Table 6.6: Resultant K_L^0 flux at the exit of the beam line. The K_L^0 yields for the Ni and the Pt targets and their ratio were summarized, together with the expectations by MC simulations. The first uncertainties are statistical and the second ones are systematic (discussed in Section 7.3).

Target	Flux (normalized to 2×10^{14} POT)			
	Data	GEANT4	GEANT3	FLUKA
Ni (5.4-cm-long)	$(1.94 \pm 0.05^{+0.25}_{-0.24}) \times 10^7$	0.74×10^7	1.51×10^7	2.07×10^7
Pt (6.0-cm-long)	$(4.19 \pm 0.09^{+0.47}_{-0.44}) \times 10^7$	1.52×10^7	2.38×10^7	3.24×10^7
Pt/Ni ratio	$2.16^{+0.38}_{-0.36}$	2.05	1.58	1.56

In our analysis, we tried to obtain the best parameters of the K_L^0-spectrum function (Eq. 5.1) in the K_L^0 generator, with which the simulation reproduced the data points in the reconstructed momentum distribution. To this end, we tried to minimize the χ^2 defined by

$$\chi^2 = \sum_{i=1}^{N} \frac{(N_i^{obs} - N_i^{exp})}{\sigma_i^{obs}} \tag{6.8}$$

where $N_i^{obs(exp)}$ represents the observed (expected) number of events in the i-th bin, and N is a number of data points. To calculate N_i^{exp} with each parameter set, we used the following method, instead of running the simulation again. When the parameters in the spectrum function were changed, the ratio of the new function to the original one was calculated as a function of the true K_L^0 momentum, which was defined as a weight function. In a event generated by the simulation, the information of the true K_L^0 momentum as well as the reconstructed one, was also stored. We calculated the new distribution of the reconstructed momentum (and thus N_i^{exp}) by re-weight the remaining events on an event-by-event basis. The minimization process was controlled by the MINUIT package [43]. The χ^2/NDF value was reduced from 2.50 to 0.75 for the result of the Ni target (NDF=17), and from 1.43 to 0.98 for the Pt target (NDF=18), respectively. Here, NDF means the number of degrees of freedom. Figure 7.5 shows the comparison of the data and the simulation in the reconstructed momentum distribution after the minimization.

Figure 7.6 shows the resultant K_L^0 momentum spectrum at the exit of the beam line, with overlays of various MC expectations. The data result in a slightly broader spectrum than those from the simulations.

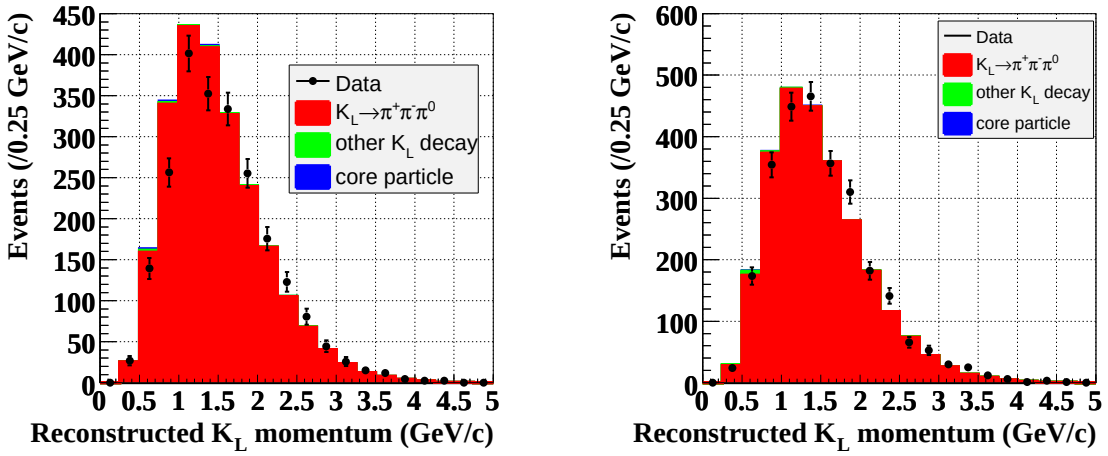

Figure 6.4: Reconstructed K_L^0 momentum distributions after imposing all the kinematic selections and comparison with the GEANT3-based simulation, for the Ni (left) and the Pt (right) targets, respectively. Dots with bars indicate the data. Histograms show the distributions obtained from the simulation, where the K_L^0 spectra obtained by the GEANT3-based beam line simulation were used.

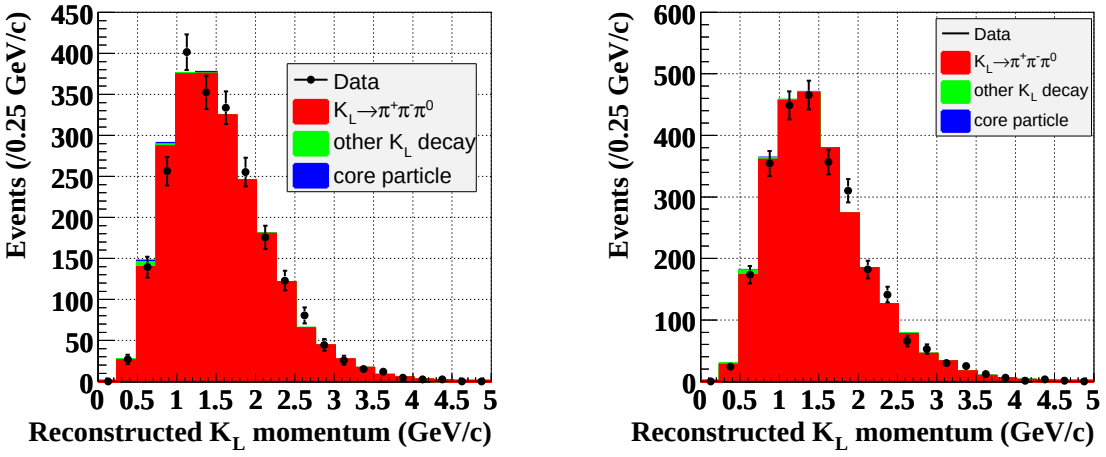

Figure 6.5: Reconstructed K_L^0 momentum distributions after imposing all the kinematic selections and comparison with the simulation with the resultant K_L^0 spectrum, for the Ni (left) and the Pt (right) targets, respectively. Dots with bars indicate the data. Histograms show the distributions obtained from the simulation after tuning the parameters in the K_L^0 generator in the simulation to fit to data points.

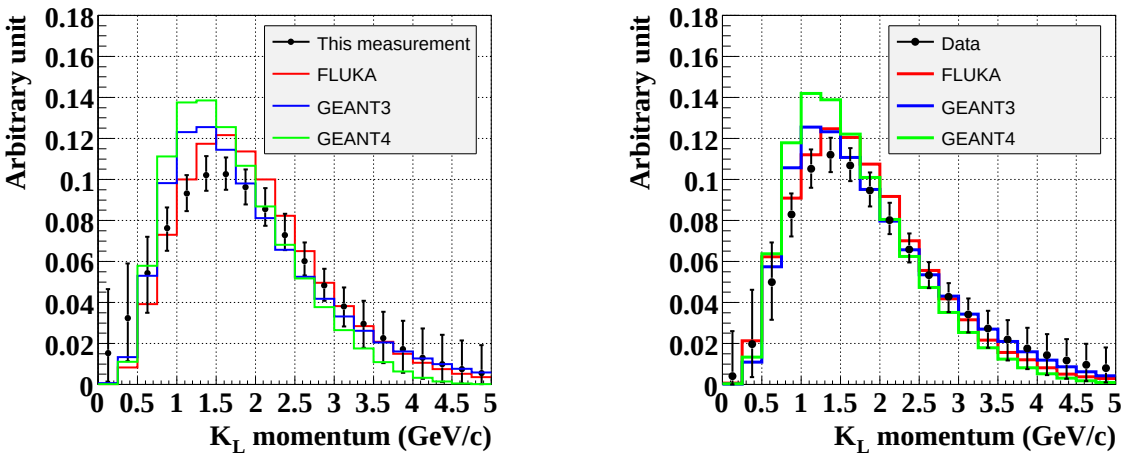

Figure 6.6: K_L^0 momentum spectrum at the exit of the beam line for the Ni (left) and for the Pt (right) targets, respectively. Points indicate the resultant spectrum with one standard-deviation error bars. The deviations in the bins are correlated with each other. The histograms show the simulation results by FLUKA (red), GEANT3 (blue), and GEANT4 (green), respectively. All the distributions are normalized to be 1 when integrated.

6.3 Discussion on the systematic uncertainties

Estimates of the systematic uncertainties are listed in Table 7.7. The largest uncertainty came from "cut effectiveness". The second largest systematic uncertainty originated from uncertainties in the K_L^0 spectrum. Other systematic uncertainties due to the alignment errors of the detector, the fluctuation in the normalization of the POT, and uncertainties in the background estimations were found to be small.

In the following subsection, each systematic uncertainty and its estimation method are described in order.

Table 6.7: Summary of systematic uncertainties.

Source	Error for the Ni target (%)	Error for the Pt target (%)
Cut effectiveness	±12.2	±10.4
K_L^0 momentum distribution	+3.5/-1.1	+4.2/-0.2
Alignment	±1.4	±1.3
POT normalization	<0.1	<0.1
Core neutron background	0/-0.5	+0.3/0
Total	+12.8/-12.3	+11.3/-10.5

6.3.1 Uncertainties due to cut effectiveness

The effectiveness of various kinematical cuts in the actual analysis differed from those expected by the MC simulations. We considered the differences to be sources of systematic uncertainties, and took them into account in the following way. We defined a partial acceptance A_i by

$$A_i = \frac{N(\text{all cuts applied})}{N(\text{all but } i\text{-th cut applied})} \tag{6.9}$$

where the index i denotes one of the kinematical cuts and N is the number of remaining events after the cuts specified in the parentheses. We compared the values of A_i obtained with the real data and the MC data. The fractional differences between the two were considered to be the systematic uncertainties. Figures 7.7 and 7.8 show the A_i of each cut obtained with the real data and their fractional differences. These fractional differences were summed in quadrature. This category of systematic uncertainties resulted in 12.2% for the Ni and 10.4% for the Pt targets, respectively.

6.3.2 Uncertainties due to the K_L^0 momentum distribution

We evaluated the variation of the signal acceptance due to the uncertainties of the K_L^0 momentum distribution because the acceptance of signal events depended on the K_L^0 momentum. We changed the parameters of the K_L^0 momentum spectrum in the simulation based on the one-standard-deviation statistical fluctuation, as shown in Fig. 7.6, and the variation was studied. The systematic uncertainties due to the uncertainties of the K_L^0 momentum distributions were + 3.5 %/-1.1 % for the Ni and +4.2 %/-0.2 % for the Pt targets, respectively.

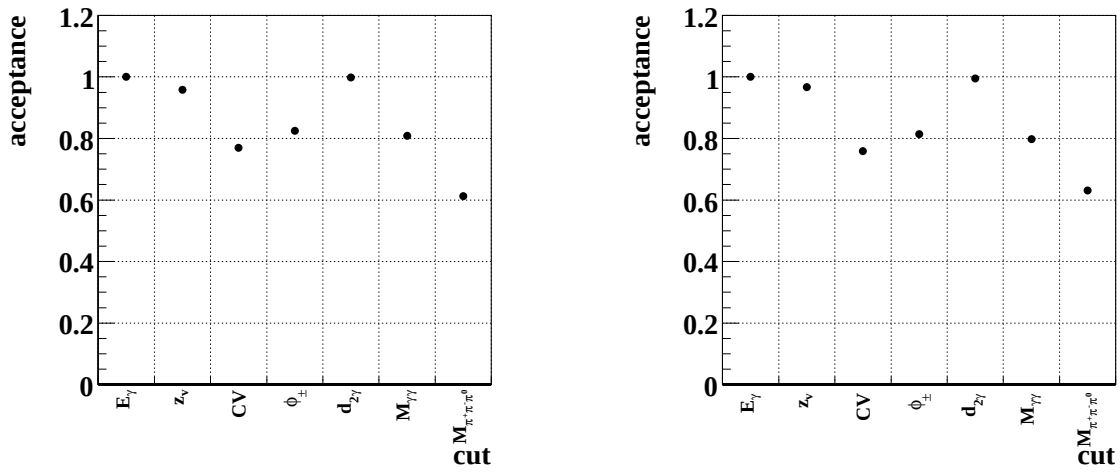

Figure 6.7: Partial acceptance of each cut obtained from data for the Ni (left) and the Pt (right) targets, respectively. The cuts E_γ and CV indicate the requirement on photon energies ($E_\gamma > 50$ MeV) and the CV (no hit in the CV), which were implied in the primary selection. Other kinematic cuts were summarized in Table 5.1.

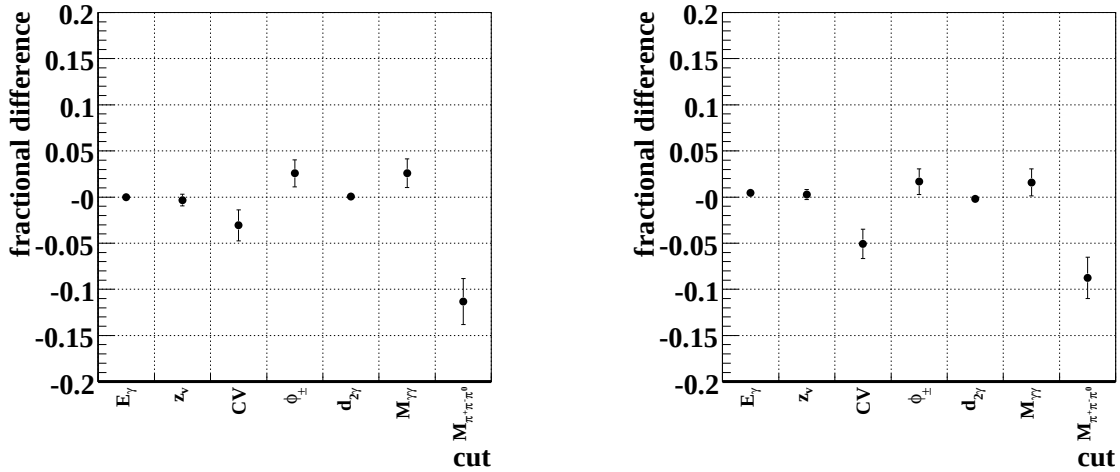

Figure 6.8: Fractional difference of the acceptance of each cut between the real data and MC data for the Ni (left) and the Pt (right) targets, respectively. The cuts E_γ and CV indicate the requirement on photon energies ($E_\gamma > 50$ MeV) and the CV (no hit in the CV), which were implied in the primary selection. Other kinematic cuts were summarized in Table 5.1.

6.3.3 Uncertainties due to the detector alignment

If the position of each detector was deviated from the proper position, the geometrical acceptance would change. Before and after the experiment, the positions of the detectors were measured with an accuracy of 1 mm. In order to study effects of the alignment errors, we changed the position of each detector within 1 mm in the simulation randomly, and calculated the acceptance. After trials of 1000 times, we estimated the uncertainties due to the detector alignment error to be $\pm$1.4% for the Ni and $\pm$1.3% for the Pt targets, respectively.

6.3.4 Uncertainties due to the fluctuation in the POT normalization

As shown in Fig 7.3, there was a spill-by-spill fluctuation of G_{SEC} in the POT normalization, which was found to be a few percent. The accumulated numbers of spills during the runs for both the Ni and the Pt targets were more than a thousand, and thus the fluctuations of the G_{SEC} mean values were reduced to be less than 0.1%.

6.3.5 Uncertainties in the estimation of neutron backgrounds

In order to evaluate the number of backgrounds from the neutron interactions in the beam, we took data in January 2010 and December 2009 without a bag filled with helium gas. This bag was inserted in the beam region between the exit window of the beam line and the surface of the calorimeter to reduce the neutron interactions in the beam. By removing it, the beam passed through air, and the events originated from neutron interactions were enhanced.

By analyzing these data, we evaluated uncertainties in the estimation of background events due to core neutrons. The left plot in Fig. 7.9 shows the vertex distribution of the data taken in January 2010 after imposing all the kinematical cuts. We further enhanced the events from the neutron interactions by removing "CV cut". When a hit in the CV was allowed the events with a proton(s) from neutron interactions could remain in the sample. As shown in the right plot of Fig. 7.9, there appeared an excess due to events originated from neutron interactions in the region of z >22.8 m. We compared the data with the expectation by the simulation in this region, and the differences between the two were considered as uncertainties. Discrepancies between the two were somewhat large, but the fractions of the neutron backgrounds in the remaining events were small, and thus the contributions were not large. As a result, the uncertainties in the estimation of neutron backgrounds was calculated to be +0/-0.5% for the Ni and +0.3/-0% for the Pt targets, respectively.

6.3.6 Uncertainties in total

In order to estimate the systematic uncertainty in total, the uncertainties estimated above were summed in quadrature. The systematic uncertainty in total resulted in +12.8/-12.3% for the Ni and +11.3/-10.5% for the Pt targets, respectively. The uncertainties were about 5 times larger than statistical uncertainties in case of both Ni and Pt targets and were main uncertainties. The largest one in the systematic uncertainties came from "cut effectiveness" on the K^0_L invariant mass, which require the invariant mass of π^+, π^- and π^0 to be 460< $M_{\pi^+\pi^-\pi^0}$ <540 MeV/c^2 to identify the K^0_L. In order to reduce the uncertainties, further understanding of distributions of $M_{\pi^+\pi^-\pi^0}$ is needed.

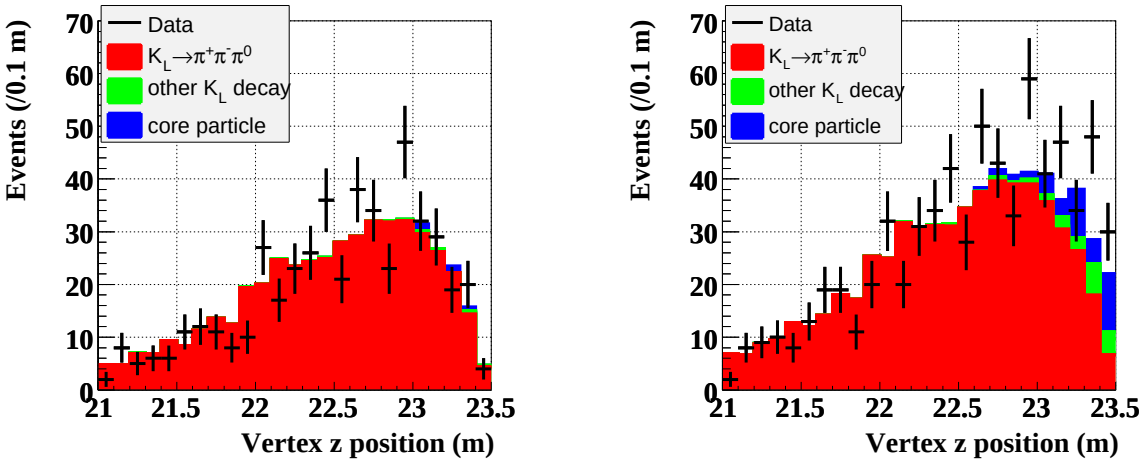

Figure 6.9: K_L^0 vertex distribution of the data taken in January 2010, when a bag filled with helium gas was removed. Dots with bars indicate the data. Histograms show the simulation results of $K_L^0 \to \pi^+\pi^-\pi^0$ signals (red), backgrounds from K_L^0 decays (green), and backgrounds due to interactions in the beam core (blue), respectively. In the left figure, all the kinematical cuts were imposed. In the right figure, all the kinematical cuts except "CV cut" were imposed. There appeared an excess due to neutron interactions in both the real data and the MC data.

Chapter 7

Discussion on the sensitivity of KOTO experiment

Prior to the K_L^0 flux measurement, we estimated the sensitivity of the KOTO experiment, using the K_L^0 flux and spectrum expected by the GEANT4 simulation. The K_L^0 flux expected by this simulation was smallest among various simulations. Now we realize by the measurement, the actual flux is 2.6 times larger than the GEANT4 expectations. The actual K_L^0 spectrum is found to be broader than the expectation, as shown in Fig. 8.1.

The expected numbers of $K_L^0 \to \pi^0\nu\bar{\nu}$ signal and K_L^0-decay backgrounds depend on the K_L^0 flux and momentum spectrum. In this section, the expected experimental sensitivity and background level of the KOTO experiment based on the results of the K_L^0 yield measurement are discussed, and are compared with those by the previous study, namely, the results using the K_L^0 flux and spectrum expected by the GEANT4 simulation. In the following, the values estimated with the flux and spectrum expected by the GEANT4 simulation are called as "GEANT4 values", while those with the results of the K_L^0 flux measurement are called as "new values".

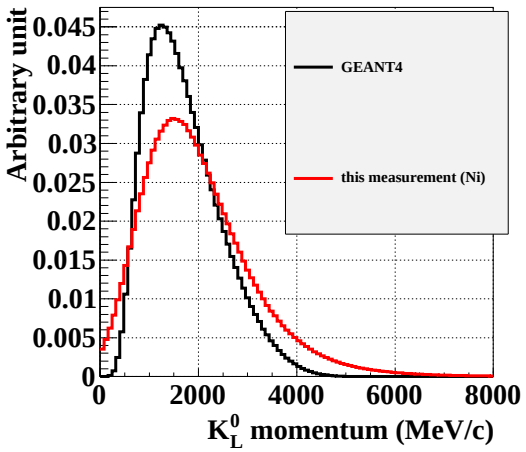

Figure 7.1: K_L^0 momentum distribution at the beam exit expected by the GEANT4 simulation (black) and calculated from the measurement (red).

7.1 Detector

Before discussion on the sensitivity and backgrounds of the KOTO experiment, the KOTO detector system is introduced.

Figure 8.2 shows the schematic view of the KOTO detector. The positions and energies of two photons from π^0 decay are measured with the CsI calorimeter located at the downstream end of the decay region. The calorimeter is made of 2576 undoped CsI crystals. These crystals are of two sizes, $2.5 \times 2.5 \times 50$ cm^3 for the central region (2240 blocks) and $5 \times 5 \times 50$ cm^3 for the outer region (336 blocks), as shown in Fig. 8.3.

In order to reduce background events by detection of extra particles, the decay region is surrounded with two large lead-scintillator sandwich counters, called "Main Barrel (MB)" and "Front Barrel (FB)". The front of the calorimeter is covered with a set of plastic scintillator counters, named "Charged Veto (CV)". An additional layer of a plastic scintillator called "Barrel Charged Veto (BCV)" is placed at the inner surface of the MB module. In order to detect particles that go through the beam hole of the calorimeter, a series of veto detectors called "Collar Counter (CC)" are placed. There are five collar counters: NCC, CC03, CC04, CC05 and CC06.

In order to detect extra particles which are still in the beam region at the downstream end of the detector system, a beam-hole veto detector is located in the beam. This detector is exposed to a high flux of beam particles. The detector should be insensitive to beam particles, while keeping a high sensitivity to products from K_L^0 decays in the decay region. The detector consists of two components; one is for detection of charged particles, which is called Beam Hole Charged Veto counter (BHCV), and the other is for photons, which is called Beam Hole Photon Veto counter (BHPV). BHCV is a set of plastic scintillator counters. BHPV is an array of Pb-Aerogel counters, each of which consists of a lead-converter and an aerogel radiator. It utilizes Cerenkov radiation to detect electrons and positrons produced by photons and is blind to heavy (and thus slow) particles produced by neutron interactions.

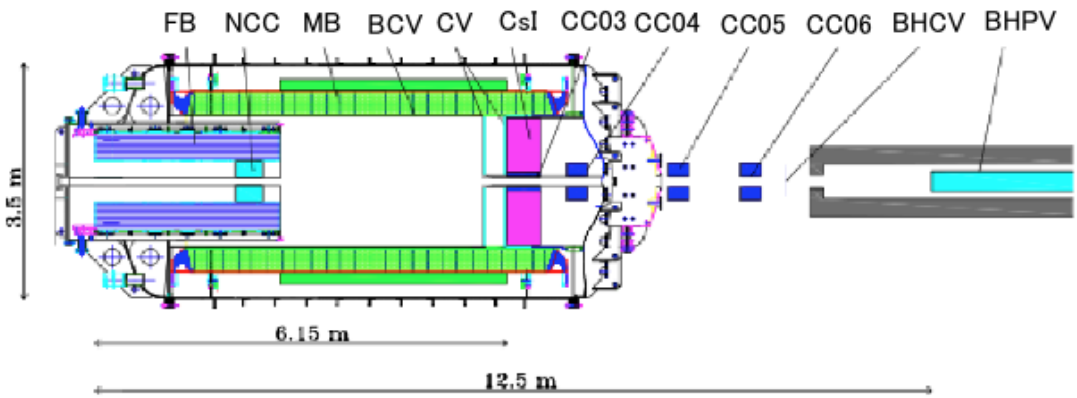

Figure 7.2: Schematic view of the KOTO detector setup

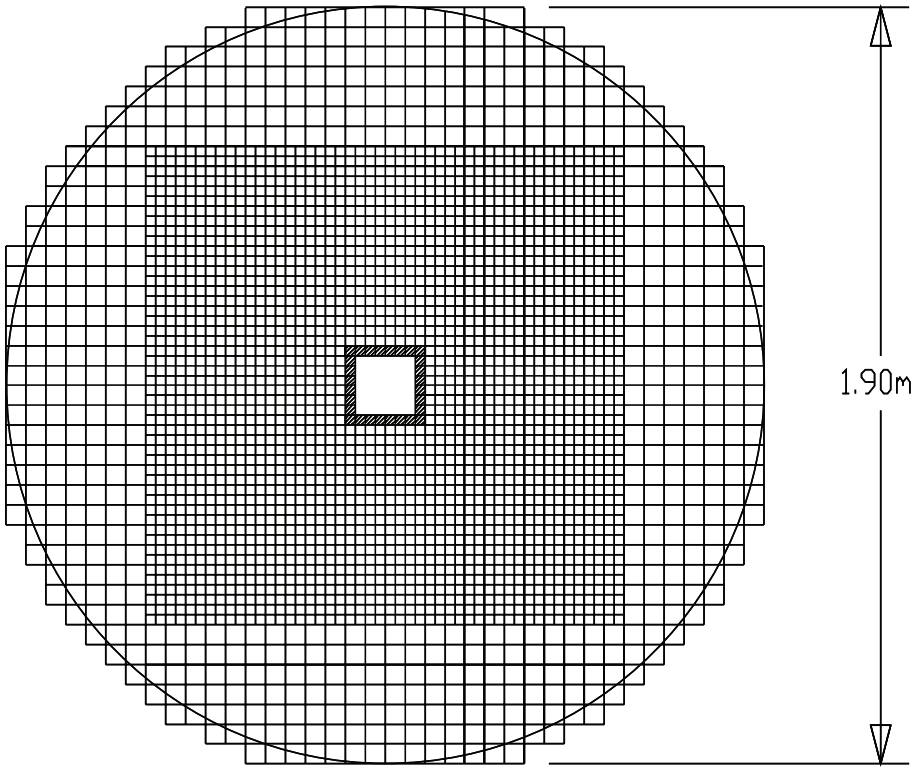

Figure 7.3: Front view of the electromagnetic calorimeter for the KOTO experiment. It is composed of undoped CsI crystals. Two types of crystals, whose dimensions are 2.5×2.5×50 cm^3 and 5.0 × 5.0 × 50 cm^3, are stacked to form a cylindrical shape, with a square beam hole in the center.

7.2 Sensitivity

7.2.1 Signal event sensitivity

Here, we define a parameter called "single event sensitivity" (SES) as:

$$\mathrm{SES}(K_L^0 \to \pi^0\nu\bar{\nu}) = \frac{1}{N_K \times A_{sig} \times (1-\Delta)} \tag{7.1}$$

where N_K is the total number of K_L^0's at the exit of beam line during the experiment, A_{sig} is the signal acceptance, and Δ is the total acceptance loss. We expect to observe $\mathrm{Br}(K_L^0 \to \pi^0\nu\bar{\nu})/\mathrm{SES}$ signal events on average in the experimental period.

In the following subsections, the detail of each factor is described, and finally the sensitivity of the KOTO experiment is discussed.

7.2.2 Signal acceptance

The acceptance for the $K_L^0 \to \pi^0\nu\bar{\nu}$ mode is represented by the product of three factors: the decay probability of K_L^0 in the decay region, the geometrical acceptance defined as the probability that two photons from a π^0 decay hit the KOTO calorimeter, and the net efficiency of various kinematical cuts in the analysis.

Decay probability

We define the decay region as the z range of $24 < z < 26$ m. The origin of the z axis is the center of the production target. The range was determined by the positions of two detectors: the downstream edge of the FB counter at $z = 23.8$ m and the front surface of the KOTO calorimeter at $z = 27.1$ m. The decay region is surrounded by the MB and FB veto counters. In this region, all particles that are produced by K_L^0 decays or neutron interactions can be detected with high efficiency by veto counters, and the signal event can be distinguished from background events.

The new value of the decay probability was calculated to be 3.9%, while the GEANT4 value was 4.0%. This decrease came from the fact that the momentum distribution obtained from the measurement was harder than the momentum distribution expected by the GEANT4 simulation.

Geometrical acceptance

The geometrical acceptance is defined as the probability that two photons from a π^0 decay in the decay region hit the calorimeter.

The GEANT4 value of the geometrical acceptance was 28%, and the new value of the geometrical acceptance becomes 27%. The slight decrease came from the fact that the momentum distribution obtained from the measurement was broader than the momentum distribution expected by the GEANT4 simulation, spreading to a lower momentum region where the geometrical acceptance gets smaller. Figures 8.4 and 8.5 show the momentum dependence of the geometrical acceptance and the product of the decay probability and geometrical acceptance, respectively. As shown in Fig. 8.5, the product of the decay probability and the geometrical acceptance had a peak around 2 GeV/c.

Efficiency for kinematical cuts

In the KOTO experiment, various kinematical conditions, described below, are required to distinguish the $K_L^0 \to \pi^0\nu\bar{\nu}$ signals from background events. The reconstruction methods,used in the KOTO experiment, of the kinematical variables are explained in Appendix A.

- E_γ cut
  The energies of photons that hit the KOTO calorimeter should be in the range of $0.1 \leq E_\gamma \leq 2.0$ GeV. This condition reduces the contamination of accidental hits.

- Calorimeter fiducial cut
  The incident position of each photon in the calorimeter should be between 175 mm and 850 mm from the center of the beam. This is to ensure that the electromagnetic showers by the photons are well contained in the calorimeter, and hence the energies and positions of the photons are properly reconstructed.

- P_t cut
  The reconstructed transverse momentum of π^0 should be in the range of $0.13 < P_t < 0.25$ GeV/c. This cut rejects backgrounds from $K_L^0 \to \pi^+\pi^-\pi^0$ and $K_L^0 \to \gamma\gamma$ decays.

- Collinearity angle cut
  The collinearity angle is defined as the projected angle of two photons in the calorimeter plane (x - y plane). The collinearity angle is required to be less than 150 degree to reject $K_L^0 \to \gamma\gamma$ background events, which two photons are expected to go to the opposite (and collinear) directions in the plane.

- E-θ cut
  There is a certain correlation between the energy and the polar angle of a photon that comes from a π^0 decay in the $K_L^0 \to \pi^0\nu\bar{\nu}$ signal and enters into the calorimeter. The reconstructed energy and angle of each photon should satisfy kinematics that is consistent with the correlation.

- E-ratio cut
  The ratio between the lower and the higher energy of two photons is required to be greater than 0.2 to reject odd-paring events for $K_L^0 \to 2\pi^0$ decays, which have two photons from different π^0 decays in the calorimeter.

- E-total cut
  The sum of energies of two photons should be greater than 0.5 GeV. This cut is effective to reject events in which a π^0 comes from the downstream region of the calorimeter, with photons traveling back upstream.

- γ distance cut
  The distance between two photons at the front surface of the calorimeter is required to be more than 300 mm. It ensures that electromagnetic showers of two photons are separated so that their energies and positions are reconstructed correctly.

- P_t/P_Z cut
  The π^0 kinematics is further restricted in the P_t/P_Z-Z plane (where P_Z is a longitudinal momentum of π^0) in order to reduce backgrounds that come from η productions by halo neutrons in the CV counter.

- Cluster-χ^2 cut
  This cut examines a shape of a cluster in the calorimeter, and selects events with two proper photon candidates. Here, a cluster is defined as a group of hits in the calorimeter that are identified to be generated by one photon. The cut is developed to distinguish a single photon cluster from other types of clusters, such as a fusion cluster that is made by two photons hitting the calorimeter closely and a fake cluster that is created by a hadronic shower. A cluster-χ^2 is calculated by comparing a pattern of energy deposits in a cluster with those in the simulated clusters by an electromagnetic shower model. A detailed description of the cut is found elsewhere [45]. We request cluster-χ^2 values of the two photons to be less than 2.4.

- Artificial neural-net cut
  An artificial neural-net (ANN) selection on the cluster shape is developed to reject backgrounds from η productions by halo neutrons in the CV counter [46]. The inputs to ANN are the energies of 5×5 blocks around the incident position of the photon, the reconstructed incident angle to the calorimeter that is calculated with the reconstructed z vertex, and the azimuthal angle of the incident position of the photon. We require the product of outputs from ANN for the two photon clusters to be less than 0.1.

Figure 8.6 shows the momentum dependence of the total efficiency of all the kinematical cuts and the signal acceptance. The new value of the net efficiency of all the kinematical cuts was estimated to be 22%. Here, the net efficiency (acceptance) is defined as an averaged efficiency (acceptance) over the momentum range from 0 to 8 GeV/c, with being weighted by a given momentum distribution. This value became slightly smaller compared with the GEANT4 value to be 23%. The new value of the net signal acceptance was found to be 0.24%, while the GEANT4 value was 0.26%, which change corresponds to about 8% decrease. The reason is that the momentum distribution obtained from the measurement was broader than the momentum distribution expected by the GEANT4 simulation, spreading to a lower momentum region where the signal acceptance gets smaller, as shown in the right plot in Fig. 8.6.

7.2.3 Acceptance loss

In the KOTO experiment, we require tight conditions on the veto counters to reject background events, and these cause signal losses for several reasons. In this section, the signal losses caused by tight vetoing are described.

- Backsplash loss ($\Delta_{backsplash}$)
  In some events, a part of particles in electromagnetic showers generated by photons that hit the calorimeter escapes outside the calorimeter and is detected by a veto counter(s). We require that signal candidates have no activity in the veto counters, and thus this results in a loss of the signal acceptance, which is called backsplash loss. The veto threshold is an energy deposit of 0.1 MeV for CV, 0.3 MeV for MB and BHCV, and 1 MeV for other veto counters except BHPV. We estimated the new value of this loss to be 57%, which is almost same as the GEANT4 value.

- Collateral cluster ($\Delta_{collateralcluster}$)
  In certain cases, a photon cluster accompanies a low-energy cluster(s) that is made by low-energy photons in the shower and is identified as an isolated cluster; such a nearby

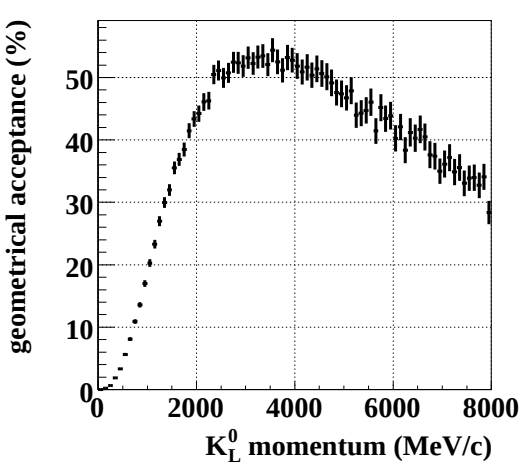

Figure 7.4: Momentum dependence of the geometrical acceptance.

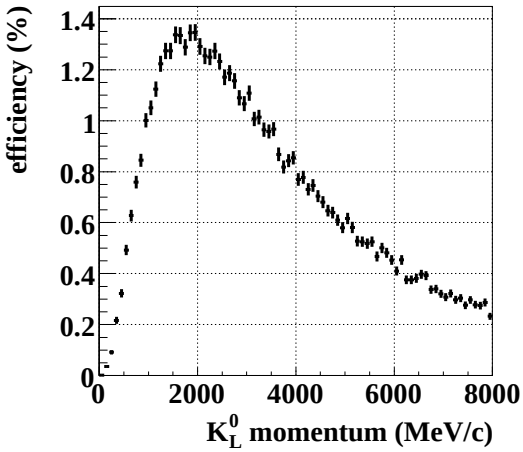

Figure 7.5: Momentum dependence of the product of the decay probability and the geometrical acceptance.

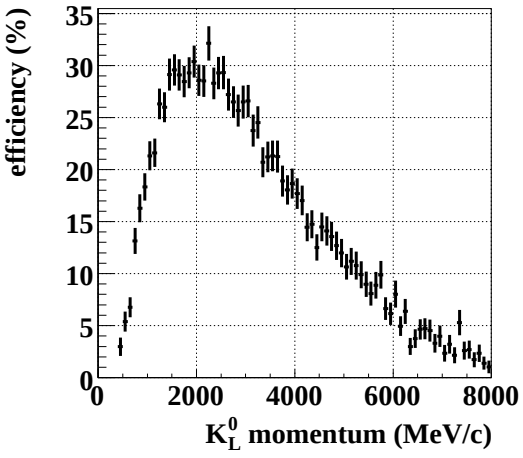

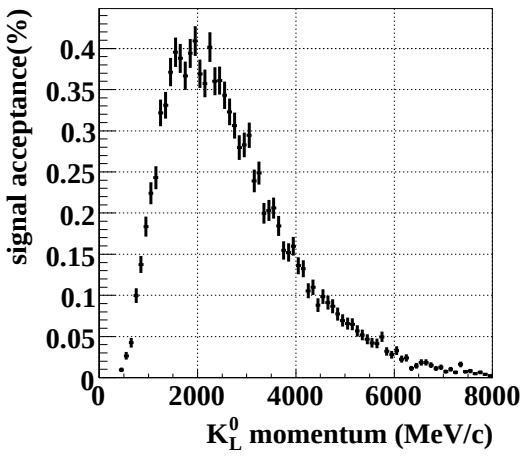

Figure 7.6: The momentum dependence of the total efficiency of all the kinematical cuts (left) and the signal acceptance (right).

cluster is called "collateral cluster". It vetoes the signal event itself. As shown in Fig. 8.7, we set the threshold for a collateral cluster as a function of the distance from the closest photon cluster in order to reduce the signal loss.

Both the new and the GEANT4 values of the signal loss due to collateral clusters were found to be 10%.

- Accidental activities ($\Delta_{accidental}$)
  High intensity beam causes accidental activities in the detector. To estimate this value, we calculate a total counting rate of the KOTO detector by using the simulation. Hits in detectors are produced by particles from K_L^0 decays and from interactions of neutrons and photons in the beam. In the calculation of the counting rates, we used the value expected by the GEANT3 simulations for the neutron and gamma fluxes. For the K_L^0 flux, we used the expected value by the GEANT4 simulation or the measured value. The detector components were divided into two categories, depending on their time-window; in the KOTO experiment, FB, NCC, and MB hits are required to be within 25 ns of the event timing, and others within 10 ns. Here, the event timing is determined by the arrival time of two photons to the calorimeter. The former group needs to detect both types of photons that go forward and travel back upstream, and thus needs to have a wider time-window. With the measured value of the K_L^0 flux, as well as the neutron and photon fluxes by the GEANT3, the counting rates of the former and latter groups were found to be 9.2 MHz and 13.9 MHz, while those with the GEANT4 K_L^0 flux were 6.5 MHz and 11.3 MHz, respectively. Considering the time windows, the new and the GEANT4 values of the accidental loss were estimated to be 37% and 28%, respectively. The detector rate (and thus the accidental loss) become larger in the case of the measured K_L^0 flux. However, the increase was not drastic because the major part of the total rate came from particles other than K_L^0's.

The total acceptance loss (Δ) is represented as:

$$1 - \Delta = (1 - \Delta_{backsplash})(1 - \Delta_{Collateralcluster})(1 - \Delta_{accidental}) \tag{7.2}$$

The new value of the total acceptance loss was calculated to be 76%, while the GEANT4 value was 72%. The change mainly came from the increase of the loss due to accidental activities.

7.2.4 Sensitivity of the KOTO experiment

Table 8.1 summarizes the values in the calculation of the sensitivity of the KOTO experiment. Figure 8.8 shows the distribution of K_L^0 events in the scatter plots of the π^0 transverse momentum (P_t) and the reconstructed vertex position after imposing all the kinematic cuts, expect for cuts on P_t and the vertex position. Based on the results of the K_L^0 flux measurement, the single event sensitivity is estimated to be 1.0×10^{-11}. This value is 2 times better than the sensitivity based on the GEANT4 expectation. With the Standard Model prediction of $\mathrm{Br}(K_L^0 \to \pi^0\nu\bar{\nu}) = 2.4 \times 10^{-11}$, we expect to observe 2.4 signal events.

7.3 Backgrounds

As mentioned in Section 2.2, background events are classified into two categories in the KOTO experiment. One is due to K_L^0 decays, and the other is due to halo neutrons. In this section,

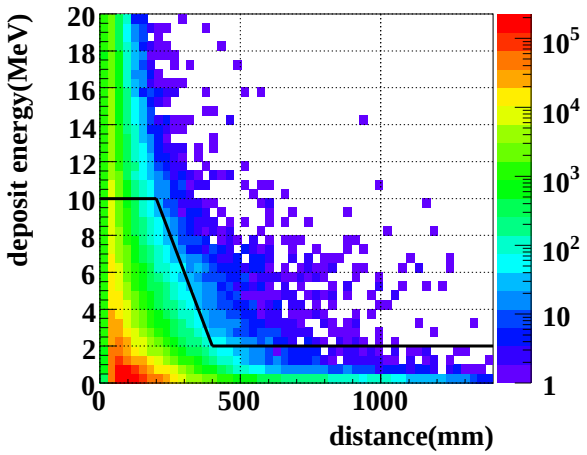

Figure 7.7: Energy deposition in a collateral cluster versus the distance from the nearest photon cluster of the two in the $K_L^0 \to \pi^0\nu\bar{\nu}$ decay, obtained by the simulation. The solid line in the figure shows the threshold function for the collateral clusters as a function of the distance.

these background events are described in order. In particular, K_L^0-decay-originated background must be re-evaluated in response to the result of the K_L^0 spectrum measurement. The K_L^0 momentum dependence of the acceptance for each K_L^0 decay is studied, and the number of background events is calculated with the K_L^0 spectrum obtained from this measurement.

7.3.1 K_L^0 background

The K_L^0 backgrounds are in turn classified into three categories.

The first one originates from decays with a π^0(s) in the final state, such as the $K_L^0 \to 2\pi^0$, $K_L^0 \to 3\pi^0$, and $K_L^0 \to \pi^+\pi^-\pi^0$ decays. In these decays, events may become backgrounds if the extra particles other than the π^0 are not detected with veto counters. Backgrounds due to the $K_L^0 \to 3\pi^0$ decay is estimated to be negligible in the KOTO experiment in spite of its large branching ratio, because the decay have four extra photons in the final state and the probability that none of the four is detected is small. The $K_L^0 \to 2\pi^0$ and $K_L^0 \to \pi^+\pi^-\pi^0$ decays are discussed later.

The second one is due to the $K_L^0 \to \gamma\gamma$ decay. This decay mode has only two photons in the final state, and there are no other particles. This background can be rejected by requiring a large transverse momentum of the π^0 candidate (P_t), because the P_t in the decay becomes zero in principle since it is a two body decay. It is found the background level of this category is negligible in the KOTO experiment.

The third one comes from decays with charged particles but a π^0 in the final state, such as $K_L^0 \to \pi^\pm e^\mp \nu$ and $K_L^0 \to \pi^\pm \mu^\mp \nu$ decays. Backgrounds from these decays, except that from the $K_L^0 \to \pi^- e^+ \nu$ decay, can be rejected by detecting charged particles with CV before they hit the calorimeter. Owing to the high efficiency of CV, these backgrounds are considered to be negligible in the KOTO experiment. In $K_L^0 \to \pi^- e^+ \nu$ decays, both of the π^- and e^+ tracks would be missed in CV through the charge-exchange and the conversion processes, $\pi^- + p \to \pi^0 + n$ and $e^+ + e^- \to \gamma + \gamma$, respectively. Four photons are generated in this type of events, and if

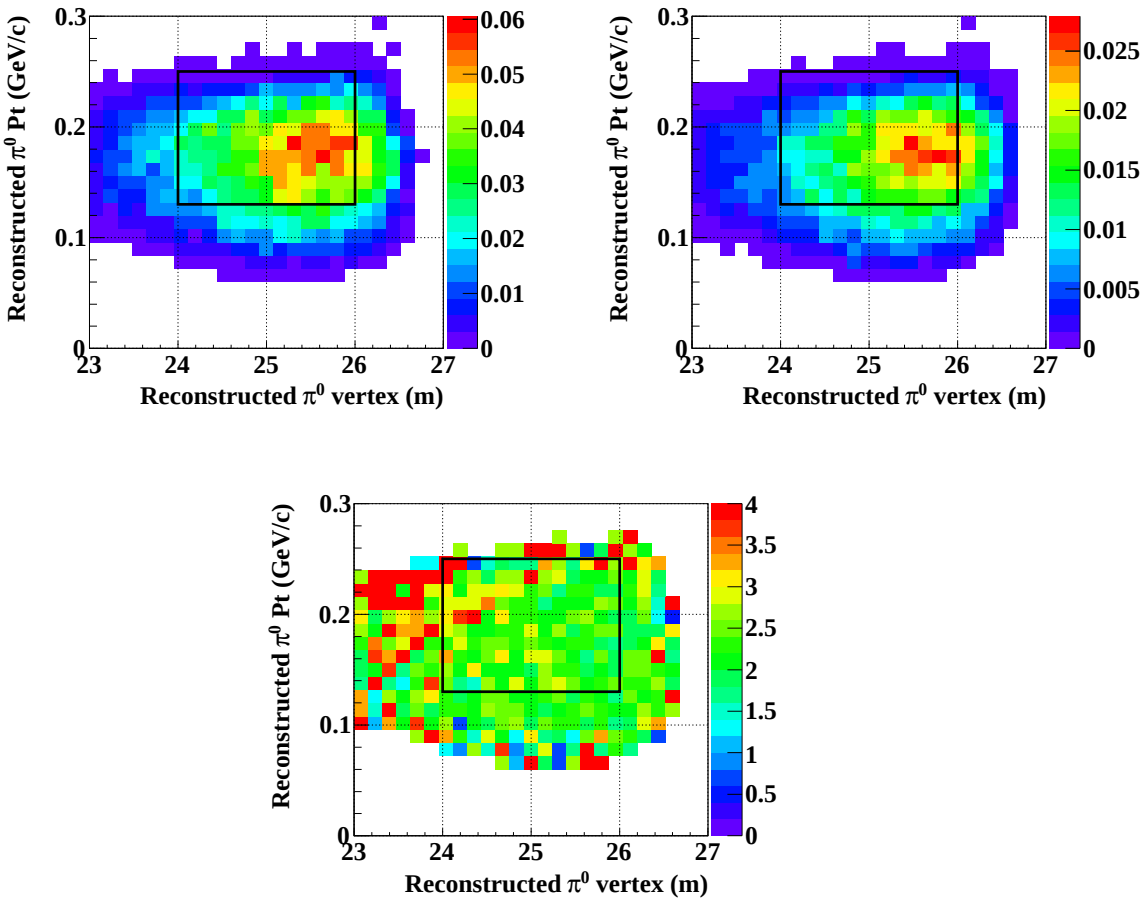

Figure 7.8: Distributions of π^0 transverse momentum (P_t) vs the reconstructed z position for the $K_L^0 \to \pi^0\nu\bar{\nu}$ events obtained by the simulations, using the expectation of the GEANT4 simulation (top left) and the results of the K_L^0 flux measurement (top right), after imposing all the kinematical cuts except for cuts on P_t and the vertex position. The bottom plot shows the ratio of the two. The region bounded by the solid line indicates the signal box.

Table 7.1: Summary of the sensitivity calculation. The values in the calculation, as well as the resultant sensitivity and the expected number of signals, are summarized in both cases with the measured K_L^0 flux ("new value") and with the GEANT4 expectation ("GEANT4 value").

	GEANT4 value	new value
K_L^0 flux/ 2×10^{14} P.O.T	7.4×10^6	1.94×10^7
P.O.T	1.8×10^{21}	1.8×10^{21}
decay probability	4.0%	3.9%
geometrical acceptance	28%	27%
cut efficiency	23%	22%
acceptance loss	72%	76%
sensitivity	2.1×10^{-11}	1.0×10^{-11}
number of signal event	1.2	2.4

two of them mimic the decay of π^0, those events become backgrounds. They are found to be potentially dangerous backgrounds, and thus are studied in detail below.

In the following, the estimation of the $K_L^0 \to 2\pi^0$, $K_L^0 \to \pi^+\pi^-\pi^0$, and $K_L^0 \to \pi^- e^+ \nu$ backgrounds by the MC simulations are described; these are the primary background sources in the KOTO experiment. In the MC simulations, we used response functions for modeling the veto detector capability and estimated the remaining numbers of backgrounds with event weights by the veto functions. The detail of the response functions is described in Appendix B.

$K_L^0 \to 2\pi^0$ background

The $K_L^0 \to 2\pi^0$ decay is considered to be the main source of backgrounds in the KOTO experiment. The reasons are that the decay mode has only one extra π^0 to veto in the final state, and, in addition, its branching ratio (8.65×10^{-4}) is eight orders of magnitude larger than that of the signal mode.

Figure 8.9 shows the K_L^0 momentum dependence of the detector acceptance for the $K_L^0 \to 2\pi^0$ decay. There are several different features compared with the signal acceptance, which is shown in the right plot in Fig. 8.6. One point is that the highest acceptance for the $K_L^0 \to 2\pi^0$ background occurs at a lower K_L^0 momentum than that for the signal mode. Another point is that a K_L^0 with higher momentum could have higher acceptance for the $K_L^0 \to 2\pi^0$ backgrounds. This is because the photons from the π^0 originated from high momentum K_L^0 is boosted in the beam direction so that such photons tend to escape through the beam hole in the calorimeter, where rejection capability by veto counters drops down. In order to detect these photons, BHPV is placed at the end of the detector system in the beam. This detector is exposed to a high flux of beam particles, and thus its detection efficiency is relatively low compared with other veto detectors. Although the veto capability becomes low at high momentum, the amount of backgrounds due to such events is negligible thanks to the rapid decrease in the flux of the K_L^0 with high momentum. Consequently, as shown in Fig. 8.10, the main contribution of the backgrounds due to the $K_L^0 \to 2\pi^0$ decay was found to come from the momentum around 1 GeV/c.

As a result of the estimation, we found that the average acceptance of the $K_L^0 \to 2\pi^0$ back-

ground events changes from 1.76×10^{-11} with the GEANT4 expectation to 1.37×10^{-11} with the measured spectrum. The reason for the decrease is due to the fact that the K_L^0 momentum spectrum obtained by our measurement was broader than the original (GEANT4) spectrum so that the number of K_L^0's that have the momentum around 1 GeV/c, where the acceptance for the $K_L^0 \to 2\pi^0$ backgrounds became highest, decreased in the calculation with the measured spectrum. Taking into account the increase of the K_L^0 flux, we estimated the number of $K_L^0 \to 2\pi^0$ backgrounds to be 1.32, while the GEANT4 value was 0.74.

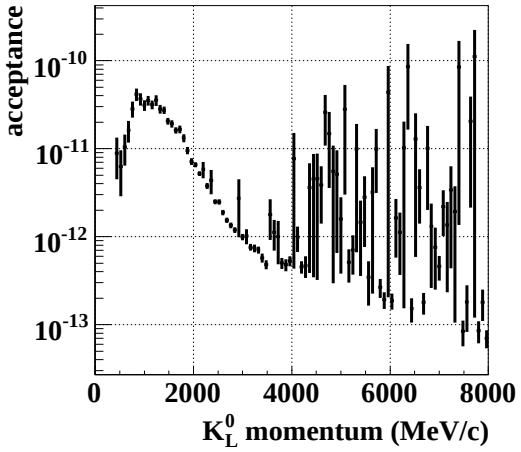

Figure 7.9: Momentum dependence of the acceptance for the $K_L^0 \to 2\pi^0$ decay after imposing all the kinematical cuts. Events are weighted by the veto functions.

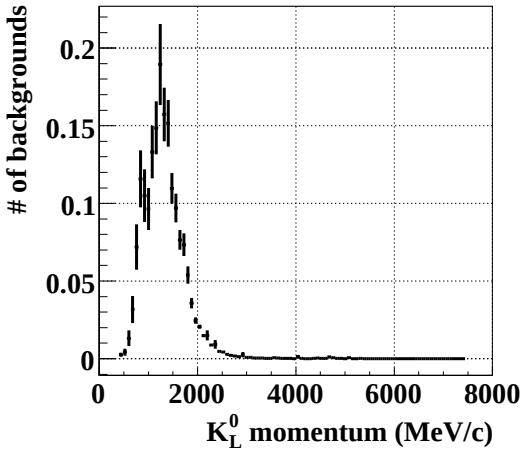

Figure 7.10: Momentum dependence of the remaining number of the $K_L^0 \to 2\pi^0$ backgrounds after imposing all the kinematic conditions. Events are weighted by the veto functions.

$K_L^0 \to \pi^+\pi^-\pi^0$ background

$K_L^0 \to \pi^+\pi^-\pi^0$ decays may become backgrounds if two charged pions happen to escape from detection with veto detectors. There are two methods for reducing this type of backgrounds. The primary method is to detect charged pions with high efficiency. The other method is to utilize the kinematical limit of the $K_L^0 \to \pi^+\pi^-\pi^0$ decay. The maximum π^0 transverse momentum is 133 MeV/c in this decay, and thus this background is effectively reduced by requiring high P_t. In the KOTO experiment, we actually require that the reconstructed π^0 has transverse momentum more than 130 MeV/c.

Although these two methods provide a powerful way to suppress this type of backgrounds, the $K_L^0 \to \pi^+\pi^-\pi^0$ backgrounds are not negligible since the decay is one of the major decay modes with a large branching ratio (12.56%). We thus study this background in more detail below.

Figure 8.11 shows the K_L^0 momentum dependence of the acceptance for the $K_L^0 \to \pi^+\pi^-\pi^0$ backgrounds. As shown in Fig.8.12, the acceptance does not have strong dependence on the K_L^0 momentum. The reason is as follows. The dominant contribution in this background comes from those charged pions that escape through the beam hole in the calorimeter. The charged counter in the beam hole (BHCV), located upstream of the BHPV, suffers a high flux of beam

particles, and its charged particle detection efficiency is relatively low compared with other charged counters. Since the $K_L^0 \to \pi^+\pi^-\pi^0$ decay is a three-body decay with a small Q-value, the probability of one charged pion going through the beam hole doesn't depend much on the boost factor (and thus the K_L^0 momentum).

As a result of the estimation, we found that the average acceptance for the $K_L^0 \to \pi^+\pi^-\pi^0$ background events does not change much by replacing the GEANT4 spectrum with the measured one; it actually varied from 8.6×10^{-15} with the GEANT4 expectation to 8.1×10^{-15} with the measured spectrum. Taking into account the increase of the K_L^0 flux, we estimated the number of $K_L^0 \to \pi^+\pi^-\pi^0$ background to be 0.11, while the GEANT4 value was 0.05.

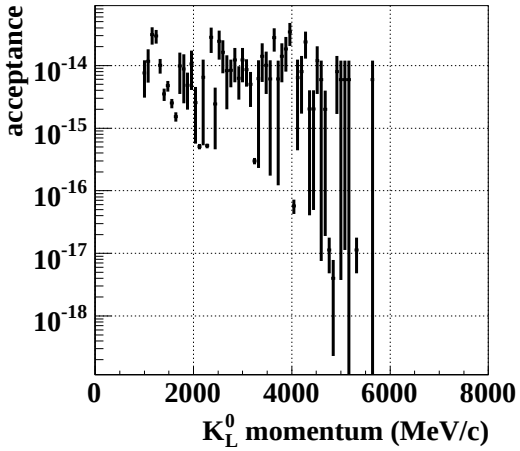

Figure 7.11: Momentum dependence of the acceptance for the $K_L^0 \to \pi^+\pi^-\pi^0$ decay after imposing all the kinematic cuts. Events are weighted by the veto functions.

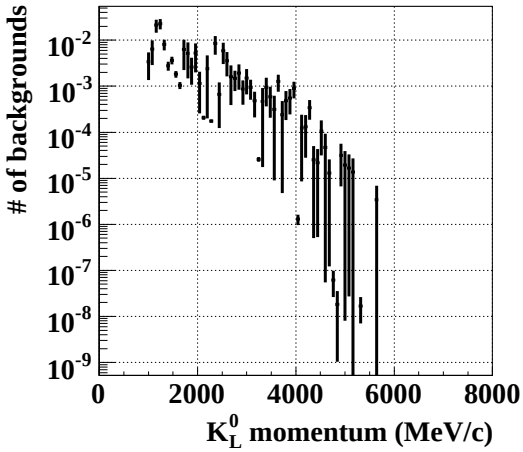

Figure 7.12: The momentum dependence of the remaining number of the $K_L^0 \to \pi^+\pi^-\pi^0$ backgrounds after imposing all the kinematic cuts. Events are weighted by the veto functions.

7.3.2 $K_L^0 \to \pi^- e^+ \nu$ background

A charge-exchange interaction of π^- ($\pi^- + p \to \pi^0 + n$) and annihilation of e^+ ($e^+ + e^- \to 2\gamma$) prevent detection of charged particles in $K_L^0 \to \pi^- e^+ \nu$ decays. If these processes occur, four photons would be generated, in which two photons are from the decay of π^0. If any two of the four photons can not be detected and the other two mimic a π^0 decay, this event may become a background event.

Figures 8.13 and 8.14 show the K_L^0 momentum dependence of the acceptance for the $K_L^0 \to \pi^- e^+ \nu$ backgrounds, and the remaining number of $K_L^0 \to \pi^- e^+ \nu$ backgrounds. In replacing the GEANT4 K_L^0 spectrum with the measured spectrum, we found the acceptance of $K_L^0 \to \pi^- e^+ \nu$ backgrounds changes from 1.80×10^{-15} to 1.54×10^{-15}. Taking the increase of the K_L^0 flux into account, we estimated the number of $K_L^0 \to \pi^- e^+ \nu$ backgrounds to be 0.07, while the GEANT4 value was 0.04.

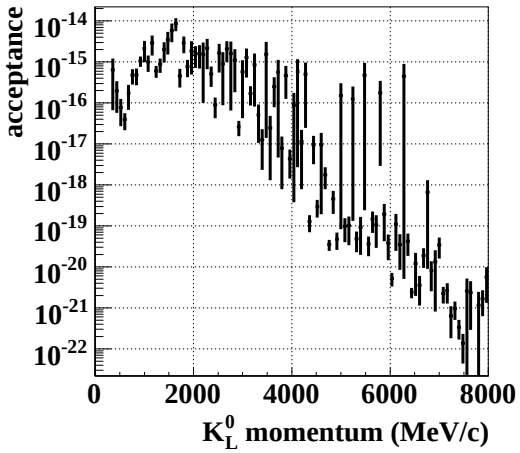

Figure 7.13: Momentum dependence of the acceptance for the $K_L^0 \to \pi^- e^+ \nu$ decay after imposing all the kinematic cuts. Events are weighted by the veto functions.

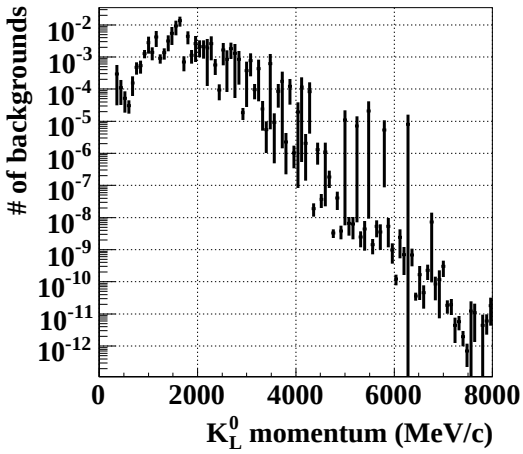

Figure 7.14: The momentum dependence of the remaining number of the $K_L^0 \to \pi^- e^+ \nu$ backgrounds after imposing all the kinematic cuts. Events are weighted by the veto functions.

7.3.3 Halo neutron background

Halo neutron backgrounds are the events made by hadronic interaction of halo neutrons with detector materials located near the beam line. In these interactions, π^0's or η's may be produced and decay into two photons, imitating the signal mode. Dominant halo neutron backgrounds are classified into three categories; they are called NCC-π^0 backgrounds, CV-π^0 backgrounds, and CV-η backgrounds. In the following the mechanism of each background is briefly described, and the number of events for each background is estimated. The detail of halo neutron backgrounds in the KOTO experiment is described elsewhere [46]. In the estimation, the halo neutron flux and spectrum expected by the GEANT3 simulation were used. In principle, there are no difference between the GEANT4 value and the new value for halo neutron backgrounds. Only the difference of accidental activities due to the increase of the K_L^0 flux affects on the estimation.

The NCC-π^0 events are the backgrounds caused by the interaction between the halo neutrons and NCC. In this interaction, two photons decayed from the produced π^0 hit the calorimeter. If the energies of the photons are measured correctly by the calorimeter, the vertex of a NCC-π^0 event should be reconstructed at the position of the detector. However, if the energy of either photon is mis-measured lower than the actual due to a shower leakage and/or photo-nuclear interaction in the calorimeter, the reconstructed vertex position would be shifted to the downstream, into the signal region. The number of NCC-π^0 backgrounds was estimated to be 0.05.

The CV-π^0 events are defined as the events in which π^0's are produced by the halo neutrons hitting CV, which is located at the upstream of the calorimeter. If extra energies of other secondary particles produced by the interaction are added to energies of the photons decayed from the π^0, the reconstructed vertex position can be shifted to the upstream, into the signal region. The number of CV-π^0 backgrounds was estimated to be 0.04.

In the CV-η events, a η particle is produced by the interaction between halo neutrons and

CV. The η decays into two photons with the branching ratio of 39%. These events can enter the signal region due to the assumption in the vertex reconstruction process that the invariant mass of two photons is the π^0 mass (133.4 MeV/c^2). Because the mass of η is 547.5 MeV/c^2, which is about four times larger than that of π^0, the reconstructed vertex can be shifted to the upstream. The number of CV-η backgrounds was estimated to be 0.01.

7.4 Summary of the sensitivity and the signal-to-noise ratio

The sensitivity and background estimations in the KOTO experiment are summarized in Table 8.2. By our measurement, the K_L^0 flux was found to be 2.6 times larger than the flux expected by the GEANT4 simulation. This resulted in the increase of the number of expected signal in the KOTO experiment: from 1.16 events to 2.39 events. In consideration of backgrounds from K_L^0 decay, we found the average acceptance for $K_L^0 \to 2\pi^0$ backgrounds is reduced with the measured K_L^0 spectrum, while those acceptances for other major decay modes does not change much. Since the $K_L^0 \to 2\pi^0$ decay dominates the remaining backgrounds, the signal-to-noise ratio (S/N) in K_L^0 decays is improved by about 20%.

The background events due to halo neutrons, which were the major background sources in the E391a experiment, are well suppressed by various efforts in the KOTO experiment, such as the implovement of the beam line, optimization of the detector configuration, and improvements in the analysis. We estimated the number of neutron backgrounds based on the (halo) neutron flux by the GEANT3 simulation. We also conducted measurements of neutrons and photons in the KOTO beam line. However, we are still making efforts to evaluate the results, and there was no conclusion applicable to update the calculation. Here, only the accidental loss with the new K_L^0 flux were added in the calculation, which does not change the results much. Consequently, the fraction of neutron backgrounds in all the remaining backgrounds was reduced, from 11% with the GEANT4 K_L^0 flux to 6% with the measured K_L^0 flux.

In total, the S/N is improved with the new K_L^0 flux to be 1.49. As explained above, the estimated number of neutron backgrounds was calculated based on the simulation, not on experimental data, and they would not be the correct values, even though their contributions are not dominant in all the backgrounds. It is important to measure the actual halo neutron flux in the KOTO experiment. For this purpose, NCC, which stands for a neutron collar counter, was designed to have combined function of a veto detector and a neutron counter. We plan to measure the halo neutron flux by NCC during the physics runs in the KOTO experiment.

.

Table 7.2: Summary of the expected numbers of the signal and backgrounds.

	source	GEANT4 value	new value
signal	$K_L^0 \to \pi^0\nu\bar{\nu}$	1.16±0.01	2.39±0.03
K_L^0 decays	$K_L^0 \to 2\pi^0$	0.74±0.02	1.32±0.04
	$K_L^0 \to \pi^+\pi^-\pi^0$	0.05±0.01	0.11±0.01
	$K_L^0 \to \pi^\pm e^\mp \nu$	0.04±0.01	0.07±0.04
halo neutron	NCC-π^0	0.05±0.02	0.05±0.02
	CV-π^0	0.04±0.04	0.04±0.04
	CV-η	0.01±0.01	0.01±0.01
	S/N	1.25	1.49

Chapter 8

Conclusion

In particle physics, one of the issues not solved is CP violation mechanism. CP violation is considered as a key to solve the mystery of asymmetry of matter and antimatter in the universe. The rare decay $K_L^0 \to \pi^0\nu\bar{\nu}$ is a sensitive probe to direct CP violation in the quark sector. The decay is a flavor changing neutral current process that is induced through electroweak loop diagrams. The decay is sensitive to new physics beyond the Standard Model, because the amplitude of the decay can vary when an unknown particle(s) appears in the loop diagram.

The KOTO experiment aims at the first observation of the $K_L^0 \to \pi^0\nu\bar{\nu}$ decay. In the KOTO experiment, the $K_L^0 \to \pi^0\nu\bar{\nu}$ decay is identified by detecting two photons from the π^0 decay. No other particles are allowed to exist in the final state. Because its branching ratio is very small, it is important to collect as many K_L^0's as possible and to suppress background events to as low levels as possible. We constructed a new neutral-kaon beam line at the J-PARC. The primary proton energy of the MR accelerator of J-PARC is 30 GeV. The extraction angle for the neutral beam is 16 degree with respect to the primary proton beam. The neutral beam is well collimated by two stages of long collimators made of iron partly embedding tungsten alloys. The solid angle is 7.8 μsr, which was optimized by considering both the K_L^0 yield and rejection of backgrounds. The beam line is also designed to reduce a beam halo as much as possible. The K_L^0 flux in the beam was estimated by using several MC simulation packages of hadron interactions. The simulation tools include GEANT4 with the QGSP-BERT-CHIPS physics list, GEANT3 with the GFLUKA hadron package, and FLUKA. The expectation values differed by up to a factor of three. Precise measurements of the K_L^0 flux and spectrum in the neutral beam line were important for the KOTO experiment. We decided to measure the K_L^0 flux and spectrum by a separate experiment prior to the physics runs of the KOTO experiment.

The setup of our K_L^0 flux measurement consisted of an electromagnetic calorimeter and a tracking hodoscope system. The two charged tracks were reconstructed by connecting hit positions in the hodoscopes, and the K_L^0 vertex position was calculated. The energies and positions of the two photons were measured by the calorimeter. By combining the vertex position, momentum vectors of two photons were obtained. To fully reconstruct a K_L^0 decay without any magnetic spectrometer, we developed original method; our idea was that we could derive the momenta of the charged pions by solving equations for the transverse momentum balance of $\pi^+\pi^-\pi^0$. The $K_L^0 \to \pi^+\pi^-\pi^0$ decay could be identified certainly by requiring that the invariant mass of two photons equals to the π^0 mass, and invariant mass of the π^+, π^-, and π^0 equals to the K_L^0 mass.

There were two distinct sets of runs; one used the 5.4-cm-long Ni target and the other used the 6-cm-long Pt target. The data in this thesis corresponds to 2.9×10^{16} protons on the Ni

target and 1.5×10^{16} protons on the Pt target, repectively. After imposing kinematical selections, the observed number of K_L^0 decays was 1923 for the Ni and 2217 for the Pt targets, respectively. The background contamination was studied by the MC simulations and was found to be 0.8% (1.1%) in the case of the Ni (Pt) target. The K_L^0 yields at the exit of the beam line, normalized to 2×10^{14} POT, were obtained to be 1.94×10^7 for the Ni target and 4.19×10^7 for the Pt target, respectively. Compared with the simulations, the resultant K_L^0 flux for the Ni target was consistent with the expectations from GEANT3 and FLUKA but larger than that from GEANT4. For the Pt target, the measured value was larger than all the expectations by three simulation packages. We also measured the K_L^0 momentum spectrum at the exit of the beam line. For this purpose, the K_L^0 spectrum in the simulation was improved iteratively so as to reproduce the measured momentum distribution. The resultant K_L^0 momentum spectrum at the exit of the beam line have a slightly broader than those from the simulations.

Finally, the impacts of the measured results on the KOTO sensitivity was discussed. After collecting 3×10^{21} POT, we expect to observe 2.5 events based on the Standard Model prediction of $\mathrm{Br}(K_L^0 \to \pi^0\nu\bar{\nu}) = 2.4\times10^{-11}$. The signal-to-background ratio (S/N) was also discussed, and we expect to achieve the S/N of 1.5.

The KOTO experiment is now in the process of detector construction and plan to finish all the detector installation to the experimental area by October in 2012. After that, we will take physics data using the Pt target for several months with 10 kW beam, which correspond to 3% of the design intensity for the slow extraction from the J-PARC MR accelerator. Using this data, we will search for the $K_L^0 \to \pi^0\nu\bar{\nu}$ decay to the sensitivity of $\mathrm{O}(10^{-9})$, exceeding the Grossman-Nir limit and stepping in a region of a new physics search. The major upgrade of the J-PARC accelerator is planed in summer 2013, where the beam energy of the LINAC will increase to 400 MeV. Together with improvements in the slow extraction, we expect a high power of 100 kW from 2014. With the high intensity beam, the KOTO experiment will continue taking physics data for three years to reach the goal of the experiment: the sensitivity comparable to the Standard Model prediction.

Appendix A

Event Reconstruction in the KOTO experiment

In the KOTO experiment, the energies and positions of two photons from a π^0 decay are measured by the calorimeter. With the information, the vertex position of the π^0 is reconstructed on the beam axis, assuming the invariant mass of the two photons to be the π^0 mass. Kinematical variables of the π^0 are also calculated and are used to discriminate signal events from background events.

In this section, firstly, we describe the method that the energies and positions of photons hitting the calorimeter are reconstructed from patterns of energy deposits in crystals. Next, we describe the method that the vertex position and kinematical variables of the π^0 are reconstructed.

A.1 clustering

When a photon hits the calorimeter, it generates an electromagnetic shower in the CsI crystals. The energy deposit of the electromagnetic shower spreads over multiple CsI crystals. We collect neighbor crystals with finite energy deposits and make a "cluster". We pick CsI crystals with their energy deposit of more than 1.5 MeV (called "cluster seeds"). Then, we group the cluster seeds whose the distance between the centers is less than 7.1 cm. We start this procedure from the CsI crystal which has a maximum energy deposit among the cluster seeds, because such a crystal is generally at the center of an electromagnetic shower generated by a photon. This process continues until all cluster seeds are used. To be recognized as a photon cluster, the group is required to contain more than two cluster seeds and to have the energy deposits of more than 20 MeV in total. We count the number of photon clusters in the calorimeter and two-photon sample is used to search for the $K_L^0 \to \pi^0\nu\bar{\nu}$ decay.

A.1.1 Energy calculation

We define the energy sum of crystals in a cluster as a cluster energy (E_{clu}). The cluster energy is smaller than the incident photon energy because a part of the energy of the incident photon leaks outside the cluster. The energy of the incident photon (E_γ) is calculated as:

$$E_\gamma = (1 + F) \times E_{clu} \tag{A.1}$$

where $F = 0.00362 + 0.0388/E_{clu}(GeV)$ is the fraction of the energy leakage obtained by the MC simulation.

A.1.2 Position calculation

In order to obtain the incident position of the photon, we calculate the center of energy in the cluster, $P_{coe} = (x_{coe}, y_{coe})$. However, there is a difference between the incident position and the center of energy to the incident photon with an angle. This is due to shower length, as shown in Fig. A.1. The difference can be corrected as a function of the shower length (L). The incident position, $P_{inc} = (x_{inc}, u_{inc})$, is calculated:

$$x_{inc} = x_{coe} - L \cdot \sin\theta \cdot \cos\phi \tag{A.2}$$

$$y_{inc} = y_{coe} - L \cdot \sin\theta \cdot \sin\phi \tag{A.3}$$

where θ is the polar angle of the photon from the z-axis, and ϕ is the azimuth angle of the photon around the z-axis. In order to estimate the incident angle of the photon, the π^0 vertex position is reconstructed by assuming the position of the photon to be P_{coe}. The π^0 reconstruction is described in the next section. We calculate the θ and ϕ with the vertex position and P_{coe}. The shower length L is expressed as:

$$L(cm/X_0) \equiv \frac{|P_{inc} - P_{rec}|}{X_0} = p_1 + p_2 \cdot In(E(GeV)) \tag{A.4}$$

where X_0 is the radiation length of the CsI (1.85 cm), E is the incident energy, and p_1, p_2 are free parameters. Using the MC simulation, we estimated p_1 and p_2 to be 6.490 and 0.993, respectively.

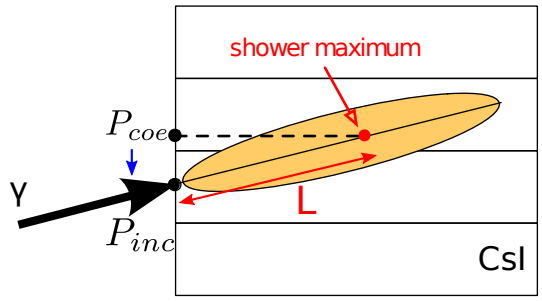

Figure A.1: A schematic view of the position correction. Taking the shower length (L) into account, the incident position (P_{inc}) was calculated from the center of energy in the cluster (P_{coe}) and the incident angle.

A.2 π^0 reconstruction

Once we obtain two photon-clusters, we calculate a π^0 decay position, z_{vtx}, by assuming the π^0 mass. In this calculation, we also assume that the vertex is on the z-axis, (0, 0, z_{vtx}).

Figure A.2 shows the relation between several parameters used in the calculation. The distance between the vertex and the calorimeter is defined as $dz = z_{CsI} - z_{vtx}$. There are following geometrical relations:

$$r_{12}^2 = d_1^2 + d_2^2 - 2d_1 d_2 \cos\theta, \tag{A.5}$$

$$d_1 = \sqrt{r_1^2 + (dz)^2} \tag{A.6}$$

$$d_2 = \sqrt{r_2^2 + (dz)^2} \tag{A.7}$$

where r_{12} is the distance between the two photons, θ is the angle between the direction of the two photon, d_1 and d_2 are the distances between the decay vertex and the hit position, r_1 and r_2 are the distance of the hit position from the z-axis. In addition, assuming that the invariant mass of the two photons is the π^0 mass (M_{π^0}), we get:

$$\cos\theta = 1 - \frac{M_{\pi^0}^2}{2E_{\gamma 1}E_{\gamma 2}}, \tag{A.8}$$

where $E_{\gamma 1}$ and $E_{\gamma 2}$ are the energies of the photons.

After reconstructing the vertex (0, 0, z_{vtx}), the momentum vector of the π^0 was calculated as the sum of two photon momenta. The transverse momentum of the π^0, P_t, is expressed as

$$P_t = \sqrt{(P_x^{\pi^0})^2 + (P_y^{\pi^0})^2}, \tag{A.9}$$

where $P_x^{\pi^0}$ and $P_y^{\pi^0}$ are x and y components of the π^0 momentum, respectively.

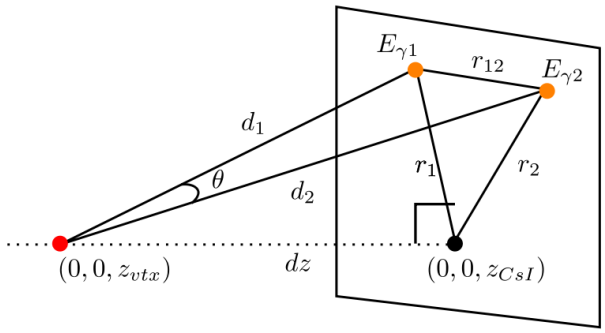

Figure A.2: Schematic view of parameters used to reconstruct the π^0 vertex.

Appendix B

Detector response function in the KOTO quick simulation

In the MC simulations, we used response functions for modeling the veto detector capability and estimated the remaining numbers of backgrounds due to the K_L^0 decays with event weights by the veto functions. There were several response functions. In the following sections, details of the functions are described.

B.1 Detection inefficiency functions for photons

The detection inefficiency functions for photons were important to evaluate the number of $K_L^0 \to 2\pi^0$ backgrounds. We made two types of the functions: one was for sampling calorimeters such as MB and FB, and the other was for BHPV.

B.1.1 Photon detection inefficiency function of MB

The detection inefficiency for photons can be caused by the following mechanisms.

- Sampling effect
  The sampling effect is a source of the inefficiency in sampling calorimeters such as MB, which consists of alternating lead and plastic scintillation plates. The electromagnetic shower generated in the inactive converter can be totally absorbed and does not produce any signal in the active layers of the detector.
- punch through
  An incident photon penetrates the detector without any interaction.
- Photonuclear interaction
  The inefficiency due to photonuclear interaction is caused by events in which a photonuclear interaction occurs in the calorimeter prior to an electromagnetic shower, and the secondary particles produced do not generate large signals above the detection threshold. For example, neutrons can be produced which then escape the calorimeter.

The sampling effect is important to the low-energy photons and the photonulclear interaction is important to the high-energy photons. We evaluated the inefficiencies due to punch through and the sampling effect by using MC simulations. We also considered a dependence of the

photon inefficiency on incident angle. This was because the effective thickness of the inactive converter would be different for the different incident angle photons. On the other hand, the inefficiency due to the photonuclear interaction in the high energy region was evaluated by using experimental data [47, 48]. The threshold value of MB set 0.3 MeV by energy loss in scintillator layers. Figure B.1 shows the photon detection inefficiency function for MB. The function were also used for FB and Collar Counters.

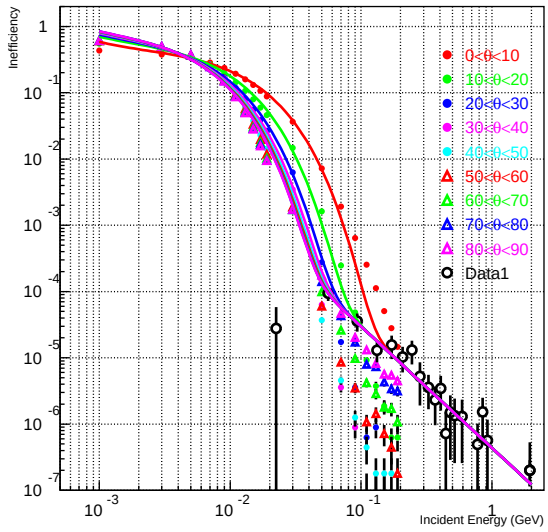

Figure B.1: Photon detection inefficiencies for MB as a function of incident photon energy. The open black circles are experimental data for photonuclear interactions. MC results for the inefficiencies due to punch-through and sampling fluctuations are shown as colored points. Different colors indicate different incident angle on the detector. The solid curves are the model inefficiency functions obtained by fitting the data and MC resuts.

B.1.2 Photon detection inefficiency function of BHPV

BHPV is located at the downstream end of the KOTO detector system. BHPV is an array of Pb-Aerogel counters, each of which consists of a lead-converter and an aerogel radiator. It utilizes Cerenkov radiation to detect electrons and positrons produced by photons and is blind to heavy particles produced by neutron interactions. The counters are lined up in 25 layers along the beam direction.

In order to estimate the detection inefficiency of BHPV for photons, we built a simulation tool based on the GEANT3 framework. All of the Cerenkov photons were traced by using our own subroutines. The simulation included the effect of optical properties of aerogel tiles and the light collecting system. Figure B.2 shows the photon detection inefficiency of BHPV obtained by the simulation. In order to identify events due to photons, we required three or more consecutive hits along the beam direction, where the threshold of each counter was set to be 4 photoelectrons. The requirement enabled us to select events that had their shower development in the forward direction, and thus reduce the sensitivity to neutron.

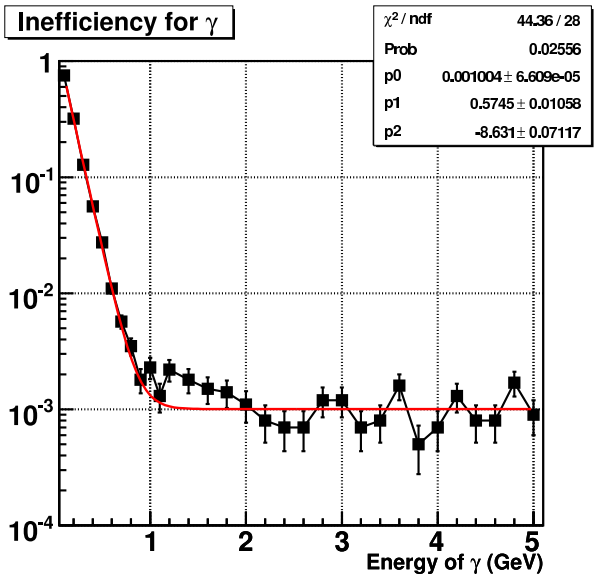

Figure B.2: Expected photon inefficiency of BHPV. The black dots show the photon inefficiency of BHPV obtained by the simulation. The red curve indicates our inefficiency function Inefficiency $= p_0 + exp(p1 + p2 \times E_\gamma)$, which was used for background estimations.

B.2 Detection inefficiency functions for charged particles

The detection inefficiency functions for charged particles, especially π^+ and π^-, were important to evaluate the number of $K_L^0 \to \pi^+\pi^-\pi^0$ backgrounds. We made two types of the functions: one was for charged veto counters such as CV and BCV, and the other was for BHCV.

B.2.1 Charged particle inefficiency functions of CV

The main source of the π^- detection inefficiency is the charge-exchange process $\pi^- + p \to \pi^0 + n$. The π^- can change into neutral particles through the process before the energy loss of the π^- in CV exceed the detection threshold of CV, and escape outside the detector. The inefficiency due to the charge-exchange process can reduced by using the information of the photon counters behind the charged particle counters. Therefore, the estimates here result from a combination of charged and photon counters. We performed a MC simulation to obtain inefficiencies for π^+ and π^-, as shown in Fig B.3. The data points in the figure show the experimental data of inefficiency measurements by charged particle beams at PSI [49]. Because the MC result does not reproduce the experimental data very well, we decided to use only the shape of the inefficiency curve from the simulation and scale it to fit the data. In these plots, we assumed a detection threshold of 100 keV. The functions were also used for other charged veto counters except BHCV.

B.2.2 Charged particle inefficiency functions of BHCV

We estimated the BHCV inefficiency to be 0.5%, independent of particle species and the energies of the particle. The dominant source of BHCV inefficiency is masking effect. BHCV suffers from a high counting rate due to beam photons and neutrons. If a fake signal happens to come just

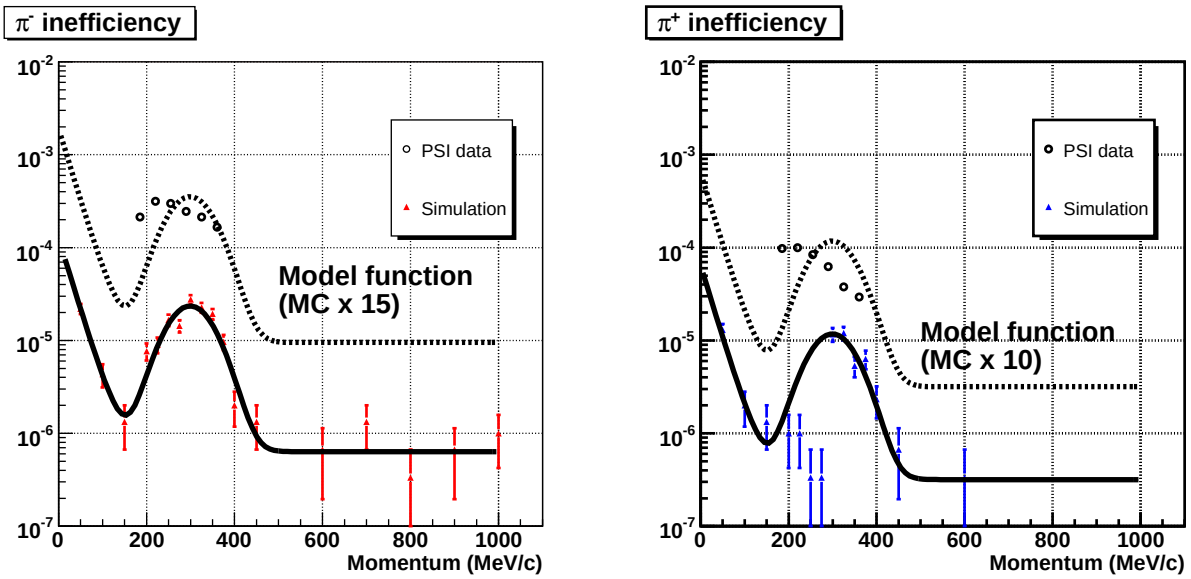

Figure B.3: Inefficiency for negative (left) and positive pions (right), with the combination of charged particle detectors and photon counters behind them. The shape of the curve is obtained by fitting the simulation result, as indicated by the lower curve in the plots. We scaled it to reproduce the measured data by the PSI group, as indicated with dashed line, and used it as the model function of pion inefficiency.

before the particle that we want to veto, wrong timing information is recorded and masks the genuine signal.

Bibliography

[1] J. H. Christenson, J. W. Cronin, V. L. Fitch, and R. Turlay, Phys. Rev. Lett. **13**, 138 (1964).

[2] A. Alavi-Harati *et al.*, Phys. Rev. D **67**, 012005 (2003).

[3] N. Cabibbo, Phys. Rev. Lett. **10**, 531 (1963);
M. Kobayashi and T. Maskawa, Prog. Theor. Phys. **49**, 652 (1973).

[4] L. Wolfenstein, Phys. Rev. Lett. **51**, 1945 (1983).

[5] A. J. Buras, F. Schwab, and S. Uhlig, (2004), hep-ph/0405132.

[6] T.Inami and C.S.Lim, *Progr. Theor. Phys.* **65**, 297 (1981); Erratum-*ibid.* **65** 1172 (1981).

[7] J. Brod, M. Gorbahn, and E. Stamou, Phys. Rev. D **83** (2011) 034030.

[8] Y. Grossman and Y. Nir, Phys. Lett. **B398**, 163 (1997), hep-ph/9701313.

[9] V. V. Anisimovsky *et al.* (E949), Phys. Rev. Lett. **93**, 031801 (2004), hep-ex/0403036.

[10] A. J. Buras, T. Ewerth, S. Jager, and J. Rosiek, Nucl. Phys. **B714**, 103 (2005), hep-ph/0408142.

[11] G. D'Ambrosio, G. F. Giudice, G. Isidori, and A. Strumia, Nucl. Phys. **B645**, 155 (2002), hep-ph/0207036.

[12] U. Haisch, A. Weiler, Phys. Rev. **D76**, 074027 (2007), hep-ph/07062054.

[13] M. Blanke, A. J. Buras, B. Duling, S. Recksiegel, and C. Tarantino, hep-ph/09065454.

[14] T. Goto, Y. Okada, and Y. Yamamoto, Phys. Lett. **B670** 378 (2009), hep-ph/08094753.

[15] C. Promberger, S. Schatt, and F. Schwab, Phys. Rev. **D75** 115007 (2007), hep-ph/0702169.

[16] W. S. Hou, M. Nagashima, and A. Soddu, Phys. Rev. **D72** 115007 (2005), hep-ph/0508237.

[17] F. Mescia and C. Smith, http://www.lnf.infn.it/wg/vus/content/Krare.html

[18] L. S. Littenberg, Phys. Rev. D **39**, 3322 (1989).

[19] J.K. Ahn *et al.* (E391a Collaboration), Phys. ReV. D **81** (2010) 072004.

[20] J. Comfort *et al* (E14 Collaboration) "Proposal for $K_L^0 \to \pi^0\nu\bar{\nu}$ Experiment at J-PARC", http://j-jparc.jp/NuclPart/Proposal_e.html .

[21] D.E. Jaffe, K.H. Lo, J.R. Comfort, M. Sivertz, Nucl. Instr. Meth. Phys. Res. B **246** (2006) 309-321.

[22] S. Eidelman *et al.*, (Particle Data Group), Phys. Lett. B **592**, (2004) 1.

[23] Y.Itow *et al.* " The JHF-Kamioka neutrino project " arXiv:hep-ex/0106019 (2001)

[24] T. Shimogawa *et al.* (E14 collaboration), Nucl. Instr. Meth. Phys. Res. A **623** (2010) 585-587.

[25] GEANT3, A detector description and simulation tool, 1993. Application Software Group, Computing and Networks Division, CERN, Geneva.; A. Fasso, A. Ferrari, J. Ranft, P.R. Sala in: A. Menzione and A. Scribano (eds.), Proc. IV Int. Conf. on Calorimetry in High Energy Physics, La Biodola, World Scientific, 1993, pp. 493–502.

[26] GEANT4 version 9.4 patch-02. http://geant4.cern.ch; S. Agostinelli *et al.*, Nucl. Instr. Meth. Phys. Res. A 506 (2003) 250–303; J. Allison *et al.*, IEEE Trans. Nucl. Sci. 53 (2006) 270–278.

[27] FLUKA version 2008.3 and later. http://www.fluka.org/fluka.php; G. Battistoni *et al.* in: M. Albrow, R. Raja (eds.), Proceedings of the Hadronic Shower Simulation Workshop 2006, AIP Conference Proceeding 896 (2007) 31–49; A. Fasso, A. Ferrari, J. Ranft, and P.R. Sala, CERN-2005-10 (2005), INFN/TC_05/11, SLAC-R-773.

[28] G. Takahashi *et al.* Jpn. J. Appl. Phys. **50** (2011) 036701.

[29] Hamamatsu Photonics Inc., http://jp.hamamatsu.com/ .

[30] M. Doroshenko *et al.* (E391a Collaboration), Nucl. Instr. Meth. Phys. Res. A **545** (2005) 278-295.

[31] TDK Corporation, http://www.tdk.co.jp/ .

[32] Technoland Corporation, http://www.tcnland.co.jp/ .

[33] National Semiconductor Corporation, http://www.national.com/jp/ .

[34] Kuraray Co., Ltd., http://www.kuraray.co.jp/en/ .

[35] Eljen Technology, http://www.eljentechnology.com/ .

[36] HOSHIN ELECTRONICS CO.,LTD., http://www.kagaku.com/hoshin/index.html .

[37] Y. Arai, *et al.* Development of a new TDC LSI and a VME module. IEEE Trans. Nucl. Sci., **49**, (2002) 1164.

[38] Gamma Medica, Inc. http://www.ideas.no/ .

[39] M. H. Ahn, *et al.* Phys. Rev. D **74** (2006) 072003.

[40] K. Nitta *et al.* Nucl. Instr. Meth. Phys. Res. A **535** (2004) 147-151.

[41] M. Yoshida *et al.* IEEE Trans. Nucl. Sci. **51** (2004) 3043-3046.

[42] S. Haino *et al.* Phys. Lett. B **594** (2004) 35-46.

[43] F. James and M. Roos, Comput. Phys. Commun. **10**, (1975) 343.

[44] D.S. Barton *et al.*, Phys. Rev. D 27 (1983) 2580–2599.

[45] K.Sato, Master thesis (in Japanese), Osaka University, 2008 (in Japanese).

[46] K.Shiomi, Master thesis (in Japanese), Kyoto University, 2008 (in Japanese).

[47] S. Ajimura *et al.*, Nucl. Inst. Meth. A **552**, (2005) 263.

[48] K. Sakashita, Master thesis, Osaka University (2002).

[49] KOPIO Conceptual Design Report, 2005.